Physics of microorganism behaviour:

Motility, synchronisation, run-and-tumble, phototaxis.



Rachel Bennett

St Hugh's College

University of Oxford

A thesis submitted for the degree of

Doctor of Philosophy

Trinity 2015

In memory of David M. Creedon

Acknowledgements

I would like to thank my supervisor Ramin Golestanian for his inspiring ideas that initiated this work and for his support as I have developed this work. Thank you to my experimental collaborators, Gerard Wong and his team, particularly Andy Utada and Calvin Lee. They performed the tracking experiments which revealed the intersting surface motility of *Vibrio cholerae* (Andy) and *Shewanella* (Calvin) and I have benefitted from fruitful discussions with them. I would like to thank Andy and Gerard for their hospitalilty during my enjoyable visit to their lab. My thanks go to Nariya Uchida for insightful discussions about synchronisation and metachronism.

I have greatly appreciated the stimulating environment of the Rudolf Peierls Centre for Theoretical Physics during my time in Oxford. I would like to thank Anatolij Gelimson, Douwe Bonthuis, Till Kranz, Mira Zorkot, Jack Cohen, Arnold Mathijssen and Matthew Andrew for many interesting discussions. Thank you Michelle Bosher for all your administrative support.

My thanks go to the EPSRC for their financial support and I would also like to thank St Hugh's college for financial support towards travelling to conferences.

Finally, I would like to thank my family and friends. I would particularly like to thank my husband, Jason Bennett, and my mother, Rosemary Creedon, for their continuous encouragement and support.

Abstract

Microorganisms have evolved in a low Reynolds number environment and have adapted their behaviour to its viscosity. Here, we consider some features of behaviour observed in microorganisms and use hydrodynamic models to show that these behaviours emerge from physical interactions, including hydrodynamic friction, hydrodynamic interactions and mechanical constraints.

Swimming behaviour is affected by surfaces and observations of *Vibrio cholerae* show that it swims near a surface with two distinct motility modes. We develop a model which shows that friction between pili and the surface gives the two motility modes. The model is extended to study the behaviour of bacteria which are partially attached to a surface. Observations of *Shewanella* constrained by a surface show several different behaviours. The model shows that different degrees of surface constraint lead to different types of behaviour; the flexibility of the flagellar hook and the torque exerted by the flagellar motor also cause different behaviours. Near surface behaviour is important for understanding the initial stages of biofilm formation.

Chlamydomonas swims using synchronous beating of its two flagella. A simple model of *Chlamydomonas* is developed to study motility and synchronisation. This model shows that the stability of synchronisation is sensitive to the beat pattern. Run-and-tumble behaviour emerges when we include intrinsic noise, without the need for biochemical signalling. The model is also used to show how observed responses of the flagella to light stimuli produce phototaxis. Finally we study hydrodynamic synchronisation of many cilia and consider the stability of metachronal waves in arrays of hydrodynamically coupled cilia.

This thesis shows that physical interactions are responsible for many behavioural features and that physical models provide a useful technique for exploring open questions in biology.

Contents

1 Introduction **1**

1.1 Low Reynolds number swimming 1

1.1.1 *Vibrio cholerae* near a surface 3

1.1.2 Bacteria stuck to a surface 4

1.2 Flagellar Synchronisation 5

1.2.1 Flagellar synchronisation in *Chlamydomonas* 7

1.3 Phototaxis in *Chlamydomonas* 8

1.4 Thesis overview 11

2 Near surface motility of *Vibrio cholerae* **12**

2.1 Experimental observations 12

2.2 Hydrodynamic model with surface friction 14

2.2.1 Results of model 17

2.2.2 Swimming angle 20

2.3 Discussion 21

3 *Shewanella* at a surface **23**

3.1 Experimental observations 23

3.2 The Model 24

3.3 Results of model 25

3.4 Discussion 28

4 Simple model of *Chlamydomonas*: Synchronisation and run-and-tumble **31**

4.1 The Model 31

4.2 Swimming velocity in the synchronised state 33

4.3 Synchronisation and stability 34

4.3.1 Equal beat patterns 37

4.3.2 Initial conditions 39

4.3.3 Combinations of harmonics . . . 40
4.3.4 Mismatched coefficients . . . 42
4.4 Run-and-tumble . . . 44
4.5 Summary and discussion . . . 46

5 Phototaxis in *Chlamydomonas* 48
5.1 Coupling light intensity to beat pattern . . . 48
5.2 Results of the model . . . 50
5.3 Understanding the steering mechanism . . . 52
5.4 Summary and discussion . . . 56

6 Metachronal waves in arrays of cilia 59
6.1 The model . . . 60
6.1.1 The Blake tensor . . . 60
6.2 Constant velocity gauge . . . 62
6.3 The dispersion relation . . . 64
6.4 Stability of the wave . . . 67
6.4.1 Looking for stability analytically . . . 70
6.5 Summary and further work . . . 72

7 Summary and Conclusions 74

A Linear stability and the three-sphere model 80

B Cilia Phase Equations 81
B.1 Phase equation in original gauge . . . 81
B.2 Phase equation in constant velocity gauge to first order in perturbation 82
B.3 Dispersion Relation . . . 84
B.4 Stability of a plane wave . . . 84

Bibliography 86

List of Figures

1.1 9+2 structure of cilia 6
1.2 Image system for a Stokeslet near a boundary 7
1.3 *Chlamydomonas* eyespot 10

2.1 Observed trajectories of *V. cholerae* 13
2.2 Radius of gyration and MSD 14
2.3 Hydrodynamic model of *V. cholerae* 14
2.4 Model trajectories for small and large friction coefficient 17
2.5 Radius of curvature vs. friction coefficient 18
2.6 Swimming angles 20

3.1 Model of *Shewanella* with part of flagellum stuck to a surface 24
3.2 Angles between flagellum and surface and head and surface 26
3.3 Trajectories of *Shewanella* model with partially stuck flagellum 28

4.1 Three-sphere model of *Chlamydomonas* 32
4.2 Velocity dependence on geometric parameters 35
4.3 Phase difference and orientation for different driving force coefficients 37
4.4 Stability of synchronised state for different harmonics and coefficients 38
4.5 Initial condition phase diagrams 40
4.6 Initial condition phase diagrams for each stability type 41
4.7 Stability of synchronised state for two harmonics 42
4.8 Phase difference for mismatched coefficients 43
4.9 Drifting phase difference for mismatched coefficients 44
4.10 Run-and-tumble trajectory 45

5.1 Three-sphere model with light 49
5.2 Phototaxis trajectories 51
5.3 Steering rate 53
5.4 Helical motion of cell 54

6.1 An individual rotor on a lattice point with trajectory $(R(\phi), z(\phi))$ . . 60
6.2 k-dependence in dispersion relation 66
6.3 Density plots of $\Re[\tilde{c}(0) - \tilde{c}(q')]$ 69
6.4 Stable and unstable wavevectors 72

Chapter 1

Introduction

In this thesis I use simple hydrodynamic models to understand complex behaviour in biological systems at low Reynolds number. My focus is on the behaviour of microorganisms and I demonstrate how observed features in their motility arise from physical mechanisms, particularly hydrodynamic friction, hydrodynamic interactions and physical constraints.

I study the motility of bacteria close to a surface, first developing a model of *Vibrio cholerae* when it swims close to a surface. I then develop the model to show how different degrees of surface constraint on the flagellum of *Shewanella* lead to different behaviours of the cell body. Synchronisation is often observed in cilia and flagella at low Reynolds number; I use *Chlamydomonas* as a model organism and study synchronisation between the two flagella, showing that the stability of synchronisation depends on the flagellar beat pattern. I use this model to show that run-and-tumble behaviour emerges from the non-linear dynamics when there is internal noise. Changes in the flagellar beat pattern of *Chlamydomonas* cause the cell to change direction and I use the model to show how flagellar responses to light allow the cell to steer phototactically. I also consider synchronisation in a large two-dimensional array of cilia and study metachronal coordination.

1.1 Low Reynolds number swimming

Microorganisms swim in low Reynolds number environments where viscous forces dominate and inertial forces are negligible. Fluid flow is described by the Stokes equations $-\nabla p + \mu\nabla^2\mathbf{v} = 0$, $\nabla \cdot \mathbf{v} = 0$, which are time reversible. One of the main challenges of building robots at this scale is designing a periodic swimming stroke that is non-reciprocal. Purcell's scallop theorem demonstrates how reciprocal shape deformations can displace the swimmer in the first half of the stroke, but the second

half of the stroke pattern brings the swimmer back to its original position, regardless of the speed at which the second half of the stroke is performed [1–3].

Non-reciprocal strokes can be achieved using two or more degrees of freedom or continuous deformations. Model swimmers that use two or more degrees of freedom include Purcell's two hinge swimmer, where three rods are connected by two joints with prescribed angular changes [1]; the linear three-sphere swimmer, joined by two rods that change their length periodically, but with a phase difference between the two rods [4]; a rotational analogue of the three-sphere swimmer [5]; the two bladder model where two spheres change their volume and the distance between them [6]. Leoni *et al.* experimentally demonstrated the effectiveness of the three-sphere model by moving three colloidal beads with optical tweezers which pumped fluid [7].

Many biological swimmers use continuous deformations for propulsion, for example rotating a rigid helical flagellum or propagating bending waves along a flexible flagellum [8, 9]. Artificial magnetically actuated swimmers have been developed experimentally [10, 11] and studied theoretically [12–15]. A self propelled biohybrid swimmer was developed by Williams *et al.* where a flexible flagellar filament is attached to a rigid head. Cardiomyocytes are cultured on a small region of the filament and contractions of the cardiomyocytes cause bending waves to propagate down the tail [16].

Squirmers are another class of model swimmer, which are spheres that swim by imposing a velocity on the surface [17]. These models can describe ciliated organisms, for example *Volvox* or *Paramecium* [18]. Squirmers are useful because the velocity field can be solved for analytically [19].

Bacteria have thin, rigid, helical flagella connected to a rotary motor embedded in the cell by a flexible hook [20]. When all the flagella motors rotate counterclockwise (CCW) the flagella form a helical bundle and propel the cell forwards [21]. Hydrodynamic interactions provide a mechanism for the individual helices to synchronise into a bundle [22]. When at least one of the motor rotates clockwise (CW) then that flagellum leaves the bundle and the cell changes direction. Shigematsu *et al.* report trajectories of *Vibrio cholerae* and *Pseudomonas aeruginosa* that follow nearly straight lines with occasional sharp bends, despite these bacteria having one flagellum only [23]. Bacteria with one flagellum use a buckling instability of the flagellar hook to change direction after reversal of the motor [24]. It is difficult to image bacterial flagella because they are only $\sim$ 20nm thick [25]; recently, a novel method has been used to observe flagella optically by putting bacteria into liquid crystals [26].

Hydrodynamic models are useful for understanding how microorganisms swim near solid surfaces [9, 27–30]. It has been observed that bacteria near a surface swim in circles [31–35]. Ramia *et al.* studied numerically the effects of hydrodynamics on a bacteria swimming near a wall using the Boundary Element Method and reported circular swimming [30]. Lauga *et al.* developed an analytic hydrodynamic model of bacteria and considered the forces and torques acting on the head and flagellum to show that the overall force and torque free conditions on the swimmer near the surface lead to the observed circular swimming [35].

The model uses resistive force theory (RFT) to calculate the forces on the flagellum which is modelled as a helical rod [36]. In resistive force theory, the force per unit length at a point on a filament is proportional to the velocity of the centre line. The components of the velocity that are tangent and normal to the filament are considered separately using two resistance coefficients:

$$\vec{f_{\parallel}} = c_{\parallel}\vec{u_{\parallel}}, \quad \vec{f_{\perp}} = c_{\perp}\vec{u_{\perp}}. \tag{1.1}$$

The normal resistance coefficient is approximately double the tangential resistance coefficient $c_{\perp} \approx 2c_{\parallel}$. Hydrodynamic interactions between the different elements of the filament are neglected. A higher order theory is slender body theory, which considers the effect of thickness which may vary along the filament [37–39].

1.1.1 *Vibrio cholerae* near a surface

Observations of the bacteria *Vibrio cholerae* show that they swim near a surface with two distinct motility modes: orbiting, where a bacterium swims in small repetitive circles, and roaming, where a bacterium travels much further across the surface and the curvature of the trajectory is smaller [40]. The curvature in the orbiting cells is much larger than that observed in *E. coli*; the curvature predicted by Lauga's model with appropriate parameters for *V. cholerae* is comparable with the smaller curvature observed in the roaming cells. We do not see the two motility modes in the mutant $\Delta mshA$, which does not have mannose-sensitive hemagglutinin (MSHA) pili, appendages on the cell body that the bacterium uses to adhere to the surface [41]. In chapter 2 we develop a hydrodynamic model to understand why there are two motility modes. Our model is based on Lauga's model in reference [35] and we add an interaction between the pili and the surface.

MSHA pili are a particular form of type IV pili (TFP). TFP are strong, thin, flexible filaments which are used for important functions including surface motility, biofilm formation, host-cell adhesion and cell signalling [42]. *V. cholerae* cause

cholera disease and pili play a significant role in infection. Toxin coregulated type IV pili (TCP) are required for colonisation of the intestine [43–45]; MSHA pili increase adherence to plankton, which is thought to increase survival of *V. cholerae* in aquatic environments [46], and it is known that abundance of plankton can lead to cholera outbreaks [47]. Motility also enhances virulence [48–52].

The near-surface swimming behaviour of *V. cholerae* is interesting for understanding biofilm formation [53]. *Pseudomonas aeruginosa* is a model organism that has features in common with *V. cholerae*: Gram-negative bacteria with a single polar flagellum and TFP. *P. aeruginosa* reversibly attach to surfaces in an upright position and use TFP to move along the surface using 'walking' motility; they then attach irreversibly in a horizontal position and move using 'crawling' motility [54, 55]. *P. aeruginosa* cells interact with a network of Psl polysaccharides through which they organise into microcolonies [56]. However, surface motility modes have not been observed in *V. cholerae*, despite having three types of TFP: MSHA pili, virulence-associated TCP and chitin-regulated pili [57]. MSHA pili and flagella are important for biofilm formation; mutants that lack MSHA pili ($\Delta mshA$) or flagella ($\Delta flaA$) take much longer to develop into biofilms than wild type cells (WT) [41]. The two near-surface motility modes of *V. cholerae* that we describe in chapter 2 allow cells to scan the surface before attachment [40].

1.1.2 Bacteria stuck to a surface

A bacterium's flagellum can reversibly attach to the surface, which causes the head to rotate when the flagellar motor exerts a torque. Observations of *Shewanella* bacteria show different features in the behaviour when the cell is constrained by the surface but still has some rotational freedom [58]. For example, sometimes the cell lies close to the surface and rotates in the surface plane and then stands on its end and spins faster about its axis. In chapter 3 we develop the hydrodynamic model of *V. cholerae* and show that different degrees of flagellar constraint result in the different types of behaviour that are observed.

Shewanella is a slightly curved rod shape with a single polar flagellum. It can survive in extreme environments and biotechnological uses have been developed from the interesting physiology of *Shewanella* [59]. Although the flagellum is not essential for biofilm formation, in flagella mutants the biofilm develops and remains flat, whereas wild-type biofilms develop a structure, indicating that the flagellum plays an important role in biofilm structure [60]. MSHA pili are required for initial attachment in the formation of biofilms and it has been suggested that flagella are important for

overcoming repulsive surface forces and spreading of the biofilm [61]. Flagella surface attachment is particularly important on rough surface as the flagella can reach into crevices and attach in places where the cell body cannot reach [62].

1.2 Flagellar Synchronisation

Synchronisation is often observed in active systems at low Reynolds number [63]. For example, when two sperms swim close together their flagella synchronise [8, 64, 65], the flagella in the biflagellate *Chlamydomonas* beat synchronously [66, 67] and the many cilia on *Opalina*, *Paramecium* and *Volvox* form metachronal waves [68–71]. Motile cilia are important for fluid transport, for example moving mucus out of the lungs, and propulsion of microorganisms [72–74]. Beating cilia also protect surfaces from biofouling [75]. Metachronal coordination can lead to stationary flows and is efficient for generating fluid flow. In synchronised beating, the flow created by a cilium's neighbour acts in the same direction as the cilium's beat, so there is a faster beat frequency, but it means a smaller fraction of the force goes into moving the flow forwards, and there is backwards movement of the flow in each cycle. In metachronal beating, a cilium works against the flow from its neighbours, so it exerts a larger force on the fluid [76]. It has been shown that metachronal coordination of independently beating cilia can arise from hydrodynamic interactions [76–79].

Eukaryotic flagella and cilia are flexible filaments, a membrane encloses an axoneme most commonly made up of 9 microtubule doublets in a ring surrounding a central microtubule pair [37]. Dynein motors are attached to the microtubules and cause adjacent microtubules to slide past each other. The axoneme is fixed at the base so the sliding causes the axoneme to bend [80]. Figure 1.1 shows the 9+2 microtubule structure of a eukaryotic flagella.

The beat consists of two parts: the power stroke and the recovery stroke [81]. During the power stroke, the cilium is quite straight to maximise the force it exerts on the fluid; during the slower recovery stroke, the cilium is more curved. In general, the beat is three-dimensional, but some organisms have planar beats, for example *Opalina* and *Chlamydomonas*. The direction of the beat is determined by the components of the basal body that anchors the cilium into the cell: the basal foot and striated fibres define the orientation of the cilium [82, 83]. Guirao and Joanny showed that arrays of cilia can spontaneously align due to hydrodynamic interactions [78]. Metachronal waves are observed in organisms with many cilia and this coordination can arise from

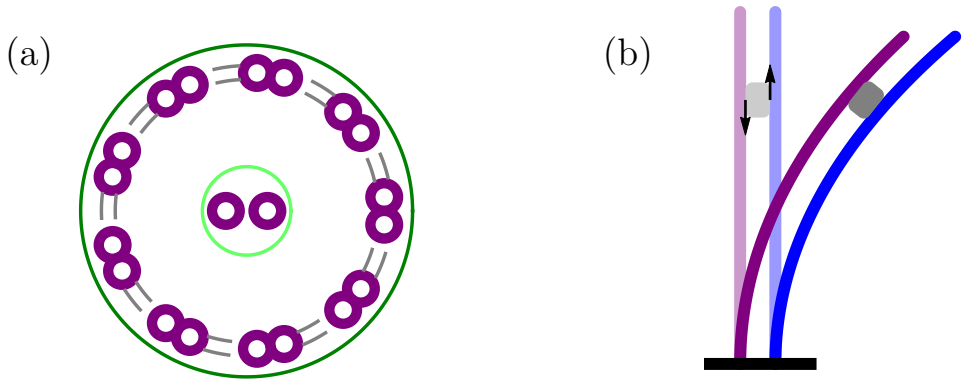


Figure 1.1: (a) 9+2 structure of microtubules forming a eukaryotic flagellum: 9 pairs of microtubule doublets form a circle around two central microtubules. Dynein motors (represented by the grey lines) slide the microtubules past each other. (b) The microtubules are fixed at the base so bending is induced when they slide past each other.

hydrodynamic interactions [76, 78, 79], although the mechanism of wave formation is not well understood.

Theoretical studies of hydrodynamic synchronisation often use simple actuated bead models [79, 84–90], and some have been used to study metachronal waves in one-dimensional arrays of cilia [91–94]. Hydrodynamic interactions are included by considering force monopoles (Stokeslets) acting on the beads. At low Reynolds number forces are linearly related to velocities so fluid velocity at $\boldsymbol{r}$ when a point force $\boldsymbol{f}$ acts at $\boldsymbol{r}_0$ is given by $\boldsymbol{v} = \mathbf{G}(\boldsymbol{r} - \boldsymbol{r}_0) \cdot \boldsymbol{f}$. In bulk fluid and in the far field limit we use the Oseen tensor for the Green's function, $\mathbf{G}$ [95]:

$$\mathbf{G}(\boldsymbol{r}) = \frac{1}{8\pi\eta r}(\mathbf{I} + \hat{\boldsymbol{r}}\hat{\boldsymbol{r}}). \tag{1.2}$$

When there is a surface nearby we use the Blake tensor which uses the method of images to maintain a no-slip boundary condition [96, 97]. The image consists of a Stokeslet of opposite sign to the original Stokelet and also a Stokes doublet and source doublet, which are shown schematically in figure 1.2. The Blake tensor for the velocity at y with a point force acting at $Y_\mathrm{f} = (Y_1, Y_2, h)$, with image at $Y_\mathrm{im}(Y_1, Y_2, -H')$ and the surface at $z = 0$ is given below, using $x = y - Y_\mathrm{f}$ and $X = y - Y_\mathrm{im}$

$$\begin{aligned}\mathbf{G}_{ij}(y, Y_\mathrm{f}) &= \tfrac{\delta_{ij}}{x} + \tfrac{x_i x_j}{x^3} - \left(\tfrac{\delta_{ij}}{X} + \tfrac{X_i X_j}{X^3}\right) \\ &+2h(\delta_{j\alpha}\delta_{\alpha k} - \delta_{j3}\delta_{3k})\tfrac{\partial}{\partial X_k}\left[\tfrac{hX_i}{X^3} - \left(\tfrac{\delta_{i3}}{X} + \quad \tfrac{X_i X_3}{X^3}\right)\right] \quad \alpha = 1, 2\end{aligned} \tag{1.3}$$

In chapter 6 we develop a hydrodynamic model of a two-dimensional array of cilia by modelling each cilium as a bead moving around a trajectory and use the

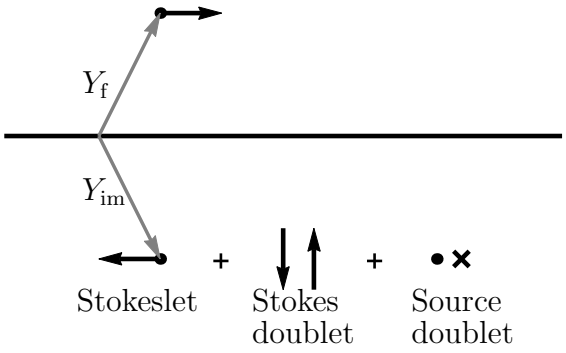


Figure 1.2: Image system for a Stokeslet near a boundary

Blake tensor for hydrodynamic interactions. We use this model to study metachronal coordination in two-dimensions and try to understand why a particular wavevector is selected.

Hydrodynamic synchronisation of two rotors requires time reversal symmetry breaking which can be achieved using flexibility in the trajectories [93] or phase dependence in the driving force [88, 89]. The relative importance of these two factors is discussed in reference [98]. In chapter 4 we develop a model of the biflagellate *Chlamydomonas* and study synchronisation between its two flagella.

1.2.1 Flagellar synchronisation in *Chlamydomonas*

Chlamydomonas is a single celled alga that swims using two flagella that beat synchronously with a breaststroke-like pattern and is a model organism for synchronisation. The cell body has diameter $\sim 10\mu$m and cells swim with velocity $\sim 100\mu$m/s so the Reynolds number is $\sim 10^{-3}$ and viscous forces dominate. In chapter 4 we consider the mechanism of synchronisation between the flagella of *Chlamydomonas* using a simple hydrodynamic model. Time reversal symmetry is broken by hydrodynamic interactions so the model can swim in its viscous environment. Asynchronies cause the cell to rotate and we use the model to show that the cell can exploit intrinsic noise to produce run-and-tumble behaviour [99, 100]. The model is developed further in chapter 5 by coupling a parameter that describes the beat pattern to the light intensity seen by the cell's eyespot, demonstrating a mechanism for phototactic steering [101].

In our model we represent the flagella as beads driven around circular trajectories by a phase dependent driving force. We find that constant forcing does not produce stable synchronisation and investigate the forms of phase dependence that give stable

synchronisation. Surprisingly, we find that hydrodynamic interactions are not necessary for synchronisation, a result reported independently by Friedrich *et al.* who developed a similar model independently [90, 102]. The mechanism of synchronisation is through the rotation of the cell body and the resulting changes in hydrodynamic friction acting on each flagellar bead. It has been demonstrated that flagella can synchronise through hydrodynamic interactions, however in free swimming *Chlamydomonas* cells this is a second order effect and the rotation dynamics provide the dominant mechanism for synchronisation [103, 104].

The stability of synchronisation in our model is sensitive to the flagellar beat pattern and run-and-tumble behaviour emerges from our model when we include internal noise. In run-and-tumble motion, a cells swims along long straight trajectories interrupted by short tumble events, where the cell reorients into a random direction. Run-and-tumble behaviour is an effective search strategy [105–107] and is often used by bacteria, in particular *E. coli* [108]. In bacteria, during runs the flagellar motors rotate CCW and tumble events are caused when one or more of the motors rotate CW. In *E. coli*, changes in the motor direction are controlled by the concentration of the protein CheY, which is phosphorylated (CheY-P) when repellants are bound and dephosphorylated when attractants are bound [109]. As the cell moves up a concentration gradient of an attractant, the concentration of CheY-P decreases, so the average run duration increases. This biased random walk provides a method for chemotaxis [110].

In *Chlamydomonas*, there is no discrete change in the beat direction of either flagella; during runs the flagella beat synchronously and short asynchronies cause tumbles [67]. Is a direct biochemical switch necessary or is it possible for a mechanical switch to produce this behaviour? In chapter 4 it is demonstrated that a biochemical switch is not necessary and that run-and-tumble behaviour emerges in our model when we include intrinsic noise in the beat pattern. *Chlamydomonas* is much less susceptible to orientational diffusion than bacteria, and it has been suggested that *Chlamydomonas* uses run-and-tumble motion to avoid predators [111].

1.3 Phototaxis in *Chlamydomonas*

Many microorganisms adapt their motion to find nutrients or light. For example, chemotactic run-and-tumble bacteria move towards a nutrient source by increasing the average run duration when they are moving up the concentration gradient. Berg and Purcell described how a microorganism could compare the concentration of

chemoattractants over a time interval of a few seconds [112]; subsequent experiments demonstrated that wild-type *E. coli* cells perform such comparisons [113, 114]. It has been demonstrated that bacteria have a response that maximises the minimum uptake of chemoattractants for any concentration profile [115].

Phototaxis is the ability of an organism to move towards or away from a light source and is useful for photosynthesis. The light intensity measured by the organism's light sensitive cells depends on the orientation of the organism, not just the position, since the flux of light is a vector quantity. *Chlamydomonas* is phototactic, but it does not use run-and-tumble to move towards the light; when there is a directed light source, *Chlamydomonas* steers directly towards or away from it. *Chlamydomonas* swims with run-and-tumble motion in darkness, so how does it steer directly towards or away from a light source? In chapter 5 we develop our simple hydrodynamic model of *Chlamydomonas* to include a coupling to the light intensity that is consistent with experimental observations. This model elucidates a mechanism for phototactic steering that is robust to the noise that causes run-and-tumble motion in the dark.

Chlamydomonas has a single eyespot on its equator. As it swims it slowly rotates about its body axis, so the eye scans the incoming light from different directions. If the incoming light is perpendicular to the swimming direction, then the light signal varies sinusoidally, but if the incoming light is parallel to the swimming direction, then the eyespot will see a constant light intensity.

When photons hit the eyespot photocurrents cause an influx of Ca^{2+} ions to the flagella [116–120]. The cis-flagellum (closest to the eyespot) and trans-flagellum (furthest from the eyespot) have different responses to the Ca^{2+} ions. Kamiya and Witman studied demembrenated axonemes and observed that the beat amplitude of the cis-axoneme decreases when the concentration of Ca^{2+} is increased, and the beat amplitude of the trans-flagellum [121] decreases when the concentration of Ca^{2+} is decreased.

Rüffer and Nultsch performed high-speed cinematography photoresponse experiments on cells held on micropipettes to study the response of beat frequency and pattern to white light stimuli [122, 123]. Two responses to an increase in light and two opposite responses to a decrease in light were observed; suggesting that the two responses to each type of stimulus would correspond to positive and negative phototaxis in free cells. They observed the same frequency response in both the cis and trans flagellum, so frequency changes do not cause steering. However, there are opposite beat amplitude changes in the cis and trans flagella. They define two types of

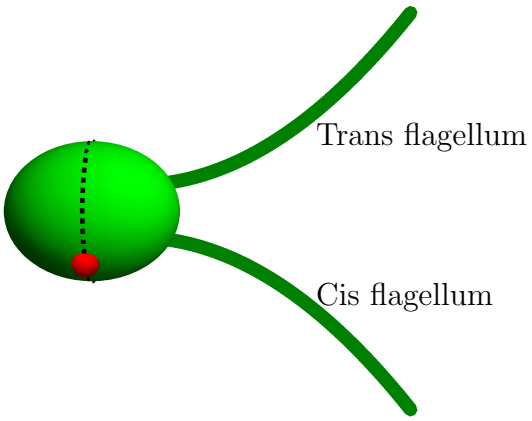


Figure 1.3: The red spot shows the position of the *Chlamydomonas* eyespot on the equator of the cell body, lying 45° ahead of the flagellar beat plane.

cells based on their amplitude response to light stimuli: In 'type (+)' cells, the trans amplitude increases and the cis amplitude decreases when the light is increased; in 'type (-)' cells, the trans amplitude decreases and the cis amplitude increases when the light is increased (vice versa when the light is decreased). Subsequent measurements with better sensitivity and which also allowed simultaneous measurements of photocurrents confirmed these results [124–126]. The mutant strain *ptx*1 shows the same amplitude response in both flagella and cannot steer phototactically [127, 128].

Evolution has carefully positioned the eyespot on the cell's equator. The eyespot is located about 45° ahead of the flagellar beat plane, so when the cell spins at its usual frequency of 2 Hz the eyespot rotates past a fixed point 60ms ahead of the beat plane. The position of the eyespot is shown by the red spot in figure 1.3. The lag time between stimulation at the eyespot and beat pattern changes is 30-40ms, so in free swimming cells, the onset of beat pattern change occurs when the beat plane is nearly parallel to the light direction [66, 122, 123]. The sensitivity of the photoreceptor is optimised for the observed 2 Hz frequency of rotation [129]. Schaller *et al* suggested that the 45° offset of the eyespot is important for the stability of the cell's path towards or away from the light [130]. Cells swim with helical motion so the eyespot either tilts towards or away from the light depending on whether the cis or trans flagellum has the larger beat amplitude and whether the cell is moving towards or away from the light. They showed that single photons can cause directional changes and argued that the eyespot should be in a shaded position to keep the correct orientation.

The direction of phototaxis is affected by the intensity of the light source: in low to moderate intensities cells usually move towards the light, but in high intensities

cells move away from the light. Pre-irradiation, concentration of cations and the wavelength of background monitoring light also affect the direction of phototaxis [122, 123, 131–133]. Evidence that photosynthesis affects the sign of phototaxis is reported in reference [133]. Eyespot directivity is essential for phototaxis; the cell body is opaque to most wavelengths so the eyespot can only receive light from the front. However, yellow light passes through the cell body, so there is little contrast between the directions and phototaxis is ineffective for yellow light [130, 134]. Understanding the mechanism that controls the direction of phototaxis remains an open question.

1.4 Thesis overview

This thesis is arranged in the following chapters. In chapter 2 we develop a hydrodynamic model of *Vibrio cholerae* to understand why it swims with two near-surface motility modes. We include an interaction between pili and the surface and find that the nonlinearity of this interaction gives the two distinct motility modes. We extend the hydrodynamic model of flagellated bacteria to include flagellar constraints with the surface in chapter 3 and suggest physical reasons for the different types of behaviour that are observed in *Shewanella* at a surface. In chapter 4 we develop a simple hydrodynamic model of *Chlamydomonas*. We study how this model can swim at low Reynolds number, the conditions on the beat pattern that are required for synchronisation, and we see that run-and-tumble behaviour emerges when we add intrinsic noise. We then couple the beat pattern to the light intensity at the eyespot and describe how the cell uses this coupling for phototactic steering in chapter 5. In chapter 6 we study metachronal waves in arrays of cilia. Each cilium is modelled as an independent rotor on a lattice and the cilia are coupled via hydrodynamic interactions. Metachronal waves emerge from this coupling and we use stability analysis to understand how a wavevector is selected.

Chapter 2

Near surface motility of *Vibrio cholerae*

Tracking experiments performed by Wong's group showed that *Vibrio cholerae* cells swim near surfaces with two distinct motility modes: orbiting, where cells travel on small, repetitive, circular paths, and roaming, where cells meander over new patches of surface and trajectories have smaller curvature [40]. We have developed a hydrodynamic model to show that these motility modes arise from a nonlinear dependence of the trajectory shape on friction with the surface.

Observations of bacteria swimming in circles near surfaces have been reported previously, [31–34] and explained as a consequence of torque balance [35], however these observations do not show the large curvature that we see in orbiting *V. cholerae* cells. The hydrodynamic model in reference [35] also does not predict the two motility modes.

After *V. cholerae* attaches to a surface, it does not walk or crawl across the surface, so the near-surface swimming motility is important for understanding the initial stages of biofilm formation. This is unlike the bacteria *Pseudomonas aeruginosa* which has walking and crawling motility modes after attachment to the surface [54, 55].

2.1 Experimental observations

The results from tracking experiments reported in this section were produced by Andrew Utada. *V. cholerae* cells were cultured in Luria-Bertani broth then injected into a sterile flow cell maintained at 30°C. High speed movies of the bacteria's motion were recorded every 4 minutes during the first 20 minutes after innoculation, then every 15 minutes until an hour after innoculation. Each movie frame was processed so that bacteria within 1μm of the surface appear as bright regions. Tracking was done

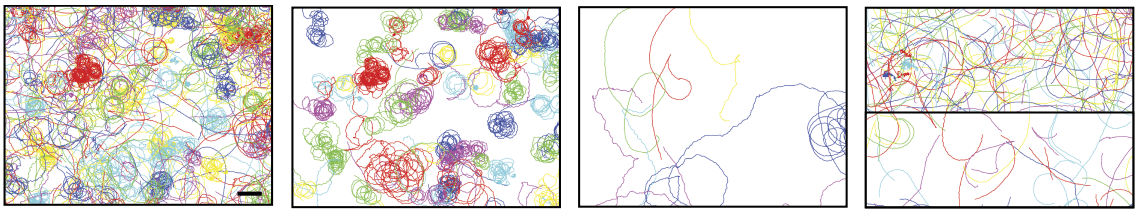


Figure 2.1: Observed trajectories of *V. cholerae*: (a) All WT trajectories, (b) Orbiting trajectories, (c) Roaming trajectories, (d) $\Delta mshA$ mutant: the top panel shows all tracks and the bottom panel shows a subset for easier visualisation. Different colours represent different tracks. Scale bar shows 10μm. Trajectories recorded by Andrew Utada and reproduced with his permission.

by locating bright regions that overlap in consecutive frames. Further experimental details are given in reference [40].

Figure 2.1 shows trajectories of *V. cholerae* cells swimming within a micron of a planar glass surface. In wild type (WT) cells we observe many tracks where the cell moves in small circles and other tracks where the cell roams further across the surface with smaller curvature. Examples of these two types of trajectories are shown separately in figures 2.1(b),(c). However, in the mutant $\Delta mshA$ we do not see these two motility types. $\Delta mshA$ mutants do not have Mannose-sensitive hemagglutinin (MSHA) pili. Figure 2.1(d) shows $\Delta mshA$ tracks and we do not see the tight circular trajectories that wild type cells make. MSHA pili are used for surface adhesion [41], but these results suggest that the MSHA pili also play a role in near-surface motility.

Figure 2.2(a) shows the radius of gyration for WT cells and we use this to characterise cells as 'orbiting', if $R_{\text{gyr}} < 8\mu\text{m}$, or 'roaming' if $R_{\text{gyr}} > 8\mu\text{m}$. The radius of gyration is defined as $R^2_{\text{gyr}} = 1/N \sum_{i=1}^{N} (\mathbf{r}_i - \mathbf{r}_{\text{cm}})^2$, which is a statistical measure of the spatial spread of the points $\mathbf{r}_i$ on the track of a particular trajectory, where $\mathbf{r}_{\text{cm}}$ is the centre of mass of all the points. The radius of gyration has a sharp peak at 3μm corresponding to the orbiting cells that move around small circles. The long tail corresponds to polydisperse roaming cells that travel across the surface. Approximately 95% of the cells are orbiting.

Figure 2.2(b) shows the mean square displacement (MSD) of WT roaming and orbiting cells, $\Delta mshA$ mutants and $\Delta flaA$ mutants (no flagella). The MSD is defined by $\Delta x^2(t) = \langle (\mathbf{x}(t+t_j) - \mathbf{x}(t_j))^2 \rangle_{t_j}$, where $\mathbf{x}(t_i) = \mathbf{r}_i$ is the position of the i^{th} point on the trajectory. The mutant $\Delta flaA$ shows diffusive behaviour with an MSD slope of ~ 1. This is expected, since these cells have no flagella to propel themselves so they just diffuse. The $\Delta mshA$ mutants do not have pili to hinder them and they travel

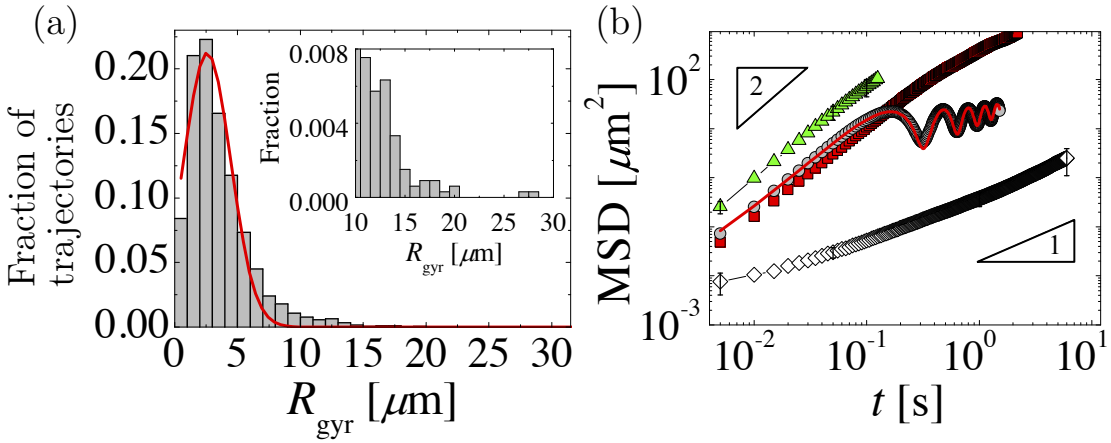


Figure 2.2: (a) Radius of gyration for WT trajectories. (b) MSD for WT orbiting, WT roaming, $\Delta mshA$ and $\Delta flaA$. Reproduced by permission of Andrew Utada.



Figure 2.3: Hydrodynamic model of *V. cholerae* swimming close to a surface. The flagellum is a thin helix driven by a rotary motor at the base of the cell head. The cell head is a curved rod and is modelled as half a wavelength of a helix. Pili are attached to the cell head and sweep past the surface as the cell rotates.

ballistically with MSD slope close to 2. WT roaming cells travel nearly ballistically, but do not travel as far as $\Delta mshA$ cells for each time interval. WT orbiting cells show near-ballistic motion on short timescales, but for $t \gtrsim 1$s, the MSD oscillates periodically, indicating circular motion.

2.2 Hydrodynamic model with surface friction

We develop a hydrodynamic model to understand why there are two motility modes for WT cells close to the surface. We use the model of Lauga *et al.* [35] and adapt it to the shape of *V. cholerae*, then add an interaction between the pili and the surface. In Lauga's model, the forces and torques on the head and flagellum of *E. coli* are written in terms of mobility matrices, then force free and torque free conditions are used to solve for the linear and angular velocities.

V. cholerae swims in a low Reynolds number environment, $Re \approx 10^{-4}$, so the fluid

flow is given by the Stokes equations, which are linear. Therefore, we can write the forces and torques on the head or the flagellum as the linear and angular velocities multiplied by a mobility matrix. We consider the forces and torques on the head and flagellum separately and use the approximation that hydrodynamic interactions between the head and the flagellum are negligible. In the experiments described in section 2.1, the cell concentration was sufficiently dilute that the cells did not interact with each other. We assume that the cell maintains a parallel orientation to the surface, as suggested by the experimental observations. We write

$$\vec{T}^{\text{head}} = M^{\text{head}}\vec{X}, \quad \vec{T}^{\text{flag}} = M^{\text{flag}}(\vec{X} - \vec{Y}), \tag{2.1}$$

where $\vec{T}^k = (F^k_{\text{x}}, F^k_{\text{y}}, F^k_{\text{z}}, L^k_{\text{x}}, L^k_{\text{y}}, L^k_{\text{z}})^{\text{T}}$ is the forces and torques acting on part k, and $k =$ head, flag; M^k is the mobility matrix of part k; $\vec{X} = (U_{\text{x}}, U_{\text{y}}, U_{\text{z}}, \Omega_{\text{x}}, \Omega_{\text{y}}, \Omega_{\text{z}})^{\text{T}}$ is the linear and angular velocity of the head; $\vec{Y} = (0, 0, 0, 0, \omega, 0)^{\text{T}}$ is the velocity of the rotary motor that rotates the flagellum CCW.

During forward swimming, the flagellum rotates counterclockwise (CCW) due to the flagellar motor. As a consequence of the torque free condition on the cell, the cell body rotates clockwise (CW). As the cell body rotates, pili that protrude from the surface of the cell sweep past the surface. We consider a time-dependent frictional force between the pili and the surface that depends linearly on the instantaneous velocity of the pili at the surface. This friction exerts a force and torque on the cell,

$$\begin{aligned} \vec{T}^{\text{pili}} &= -\gamma(1 + \cos(\Omega_{\text{y}}t + \varphi))\big(U_{\text{x}} - \Omega_{\text{y}}d,\ U_{\text{y}} + \Omega_{\text{x}}d,\ 0, \\ &\quad d(U_{\text{y}} + \Omega_{\text{x}}d),\ -d(U_{\text{x}} - \Omega_{\text{y}}d),\ -l(U_{\text{x}} - \Omega_{\text{y}}d)\big)^{\text{T}} \\ &= \gamma M^{\text{pili}}\vec{X}, \end{aligned} \tag{2.2}$$

where d is the distance from the surface to the head axis, l is the distance along the cell head axis from the centre to the longest pili and the phase difference is $\varphi = (l/L - 1/2)\pi$, where L is the length of the cell head. The strength of the interaction between the pili and the surface depends on a number of unknowns, for example distance of cell from surface, number of pili, distribution of pili, impurities on surface. It is likely that the interaction strength varies within a population, so we describe the interaction strength with a parameter γ. We solve for $\vec{X}$ numerically using force and torque balance

$$\vec{T}^{\text{head}} + \vec{T}^{\text{flag}} + \vec{T}^{\text{pili}} = 0. \tag{2.3}$$

The flagellum is a left-handed helix rotating CCW, with positions along the helix given by

$$\begin{cases} x = b\sin(s-\omega t) \\ y = -\frac{\lambda}{2\pi}s \\ z = b\cos(s-\omega t) \end{cases}, \tag{2.4}$$

where $0 < s < 2\pi n$. We use resistive force theory (RFT) as an approximation for the mobilities [36], which were calculated and given in Appendix A of Ref. [35]. RFT is the zeroth order approximation of slender body theory (SBT) which considers the force acting on a slender filament by integrating force singularities along the the filament's centre line. RFT considers the velocity $\vec{u}$ of each element δl of the filament, which is decomposed into components parallel and perpendicular to the filament: $\vec{u} = \vec{u}_\parallel + \vec{u}_\perp$. Each direction is associated with a local drag coefficient $c_\parallel$, $c_\perp$. The force on an element of length δl is then

$$\delta\vec{F} = -\delta l(c_\parallel \vec{u_\parallel} + c_\perp \vec{u_\perp}). \tag{2.5}$$

We use the far field asymptotic results of Katz *et al.* [29] for the resistant coefficients near a plane boundary:

$$c_\parallel = \frac{2\pi\mu}{\log(2[d+z(s)]/r)}, \qquad c_\perp = 2c_\parallel, \tag{2.6}$$

where $-b < z(s) < b$ is the distance of the helix filament from the helix axis, d is the distance from the surface to the helix axis and r is the radius of the helix filament.

The curved head is approximately half a wavelength of a right-handed helix rotating CW, with positions along the helix given by

$$\begin{cases} x = b\sin(s+\Omega_{\mathrm{y}} t) \\ y = \frac{\lambda}{2\pi}s \\ z = b\cos(s+\Omega_{\mathrm{y}} t) \end{cases}, \tag{2.7}$$

where $0 < s < \pi$. We use RFT to calculate the head mobilities.

We use the following values for the parameters in the model, with all distances in micrometres: head length $\lambda_{\mathrm{h}}/2 = 2.2$, head filament radius $R = 0.3$, head helix radius $B = 0.4$, gap between surface and the bottom of head $h = 0.04$, height from surface to centre of cell $d = 0.74$, flagellum wavelength $\lambda_{\mathrm{f}} = 2$, number of wavelengths $n = 3$ (so flagellum length $L_{\mathrm{f}} = 6$), flagellar helix radius $b = 0.4$, radius of flagellum filament $r = 0.02$, motor frequency $\omega = 200$ Hz. We assume that the pili are concentrated at the leading pole of the cell so $l = \lambda_{\mathrm{h}}/4$ and $\varphi = 0$.

We find that the radius of curvature depends on the geometric parameters, so we choose values that are realistic. We also find that the curvature increases with decreasing distance between the cell and the surface, even when we keep the friction coefficient, γ, constant.

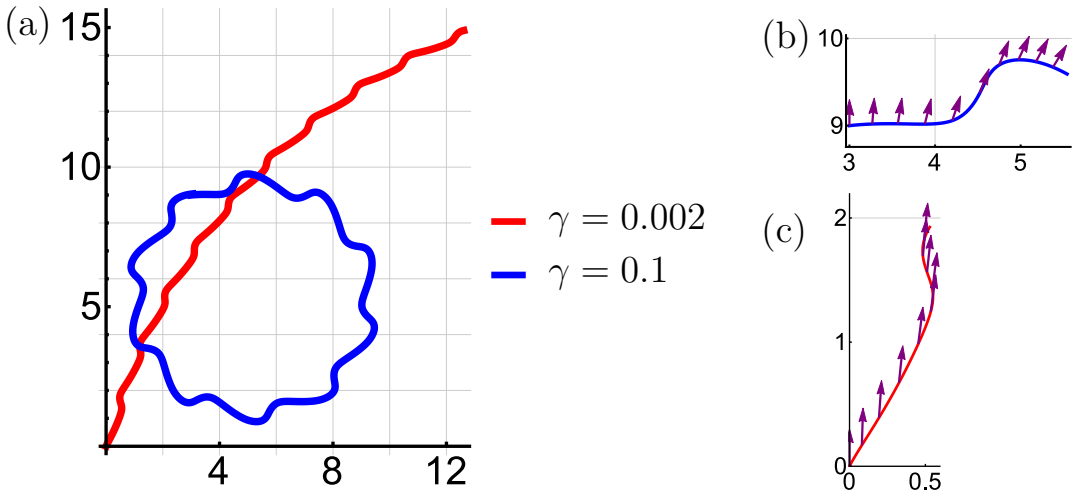


Figure 2.4: (a) Vibrio model trajectories for two choices of friction coefficient, red: $\gamma = 0.002$, blue: $\gamma = 0.1$. (b), (c) Trajectory during a single rotation of the cell head, with arrows showing the orientation of the cell head. We observe that the angle between the cell and the trajectory varies during the rotation cycle for both (b) $\gamma = 0.1$ and (c) $\gamma = 0.002$.

2.2.1 Results of model

The shape of the trajectory depends on the value of the friction coefficient γ. Figure 2.4 shows trajectories for a small and a large friction coefficient. For the small friction coefficient, $\gamma = 0.002$, the trajectory's average radius of curvature is large so the cell can move across the surface, which is the observed roaming behaviour shown in figure 2.1(c). For the large friction coefficient, $\gamma = 0.1$, the trajectory has a small radius of curvature and the cell moves repetitively around small circles, which is the observed orbiting behaviour shown in figure 2.1(b).

Figure 2.4 shows that the model can produce roaming and orbiting trajectories for small and large friction coefficients. But what about intermediate friction coefficients? Figure 2.5 shows how the radius of curvature depends on γ. We see a non-linear dependence of the radius of curvature on the friction coefficient: there is a small range of small values of γ that give a large radius of curvature, with a wide spread in the radius of curvature values, but there is a wide, flat part of the curve spread over a large range of values of γ, where large changes in γ do not change the radius of curvature significantly. The friction coefficient of an individual bacterium depends on several factors including distance from surface, number and distribution of pili, surface heterogeneities, so we expect that the different bacteria producing the tracks shown in figure 2.1 have a range of different values of γ. For a population with a range of γ,

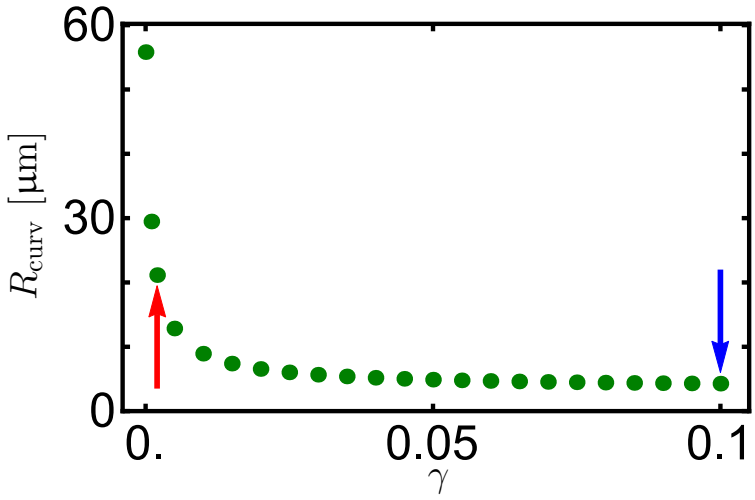


Figure 2.5: Radius of curvature dependence of the pili-surface friction coefficient. Arrows show the values of γ used in the trajectories shown in figure 2.4.

the results of our model are consistent with the experimental observations: a small number of cells have small friction coefficients, corresponding to the steep part of the curve in figure 2.5. These cells have large radius of curvature so they can meander further across the surface and there is polydispersity between the trajectories of these cells. However, the rest of the cells have friction coefficients that correspond to the flat part of the curve in 2.5, so have small values of radius of curvature and the variation in values of γ has little effect on the radius of curvature.

The flat part of the curve in figure 2.5 plateaus to a finite value; we show this by considering the radius of curvature in the limit $\gamma \to \infty$. We calculate the radius of curvature by considering the change in angle $\Delta\theta$ and x-y displacement $\Delta\rho$ of the cell over one rotation of the cell head. From the geometry, we have

$$R_{\mathrm{curv}} \sin(\Delta\theta/2) = \Delta\rho/2. \tag{2.8}$$

In the limit $\gamma \to \infty$ with finite driving torque, the pili have zero velocity at the point of contact with the surface, so from equation (2.2) this gives

$$U_x - \Omega_y d = 0, \tag{2.9}$$

where d is the distance from the centre of the cell to the surface. This means that that the cell head rolls just above the surface. We also have $U_y + \Omega_x d = 0$, but $\Omega_x << \Omega_y$ so motion in the y-direction is negligible. During rolling motion, the displacement of the cell over one head rotation is $2\pi d$ so from equation (2.8) we have

$$R_{\mathrm{min}} = \frac{\pi d}{\sin(\Delta\theta)}. \tag{2.10}$$

The angular change is $\Delta\theta \sim -\Omega_z \Delta t$, where $\Delta t \sim 1/\Omega_y$, so

$$\Delta\theta \sim -\frac{\Omega_z}{\Omega_y}; \tag{2.11}$$

the sign is due to the CW rotation of the cell. In the following we use the notation of Lauga *et al.* in reference [35], where $N_{ij}^{\alpha\beta}, M_{ij}^{\alpha\beta}$ are the viscous mobilities relating the jth component of velocity ($\beta = U$) or angular velocity ($\beta = \Omega$) to the ith component of force ($\alpha = F$) or torque ($\alpha = L$), for the cell head and flagellum respectively. From torque balance in the z-direction we have $-(N_{zx}^{\mathrm{LU}} + M_{zx}^{\mathrm{LU}})U_x - (N_{zz}^{\mathrm{L\Omega}} + M_{zz}^{\mathrm{L\Omega}})\Omega_z + N_{zy}^{\mathrm{L\Omega}}\Omega_y + M_{zy}^{\mathrm{L\Omega}}(\Omega_y - \omega) \approx 0$. We have scaling relations

$$\begin{aligned} N_{zx}^{\mathrm{LU}}, M_{zx}^{\mathrm{LU}} &\sim L^2, \\ N_{zz}^{\mathrm{L\Omega}}, M_{zz}^{\mathrm{L\Omega}} &\sim L^3, \\ N_{zy}^{\mathrm{L\Omega}}, M_{zy}^{\mathrm{L\Omega}} &\sim bL^2, \end{aligned}$$

where L and b are the characteristic length and helix radius respectively (of both head and flagellum). From these scaling relations and $U_x = \Omega_y d$ (due to infinite γ), we have

$$-\Omega_z \sim \frac{b}{L}(\omega - \Omega_y) + \frac{d}{L}\Omega_y. \tag{2.12}$$

From torque balance in the y-direction $N_{yy}^{\mathrm{L\Omega}}\Omega_y + M_{yy}^{\mathrm{L\Omega}}(\Omega_y - \omega) \approx 0$, we have

$$\frac{\omega - \Omega_y}{\Omega_y} \sim \frac{\log(d/r_{\mathrm{flag}})}{\log(d/r_{\mathrm{head}})}, \tag{2.13}$$

where $r_{\mathrm{head,flag}}$ is the width of head of flagellum filament, and $r_{\mathrm{head}} >> r_{\mathrm{flag}}$. Putting this in equation (2.10) we have

$$R_{\min} \sim \frac{\pi d}{\sin\left(\frac{b\log(d/r_{\mathrm{flag}})}{L\log(d/r_{\mathrm{head}})} + \frac{d}{L}\right)}. \tag{2.14}$$

Since $d > r_i$, the ratio of the log terms is $O(1)$. For flagella $b/L, d/L \sim O(0.1)$, so we can use the small angle approximation $\sin(x) \approx x$, and we can write equation (2.14) as

$$R_{\min} \sim \frac{\pi d}{\frac{b\log(d/r_{\mathrm{flag}})}{L\log(d/r_{\mathrm{head}})} + \frac{d}{L}}. \tag{2.15}$$

Using the experimentally derived parameters and taking a length scale $L = 4\mu\mathrm{m}$, this scaling argument yields a value $R_{\min} \approx 4\mu\mathrm{m}$, which matches the value $R_{\mathrm{curv}} = 4\mu\mathrm{m}$ that we get in the model for large $\gamma = 0.1$. It is also very close to the measured radius of curvature in orbiting cells of $3\mu\mathrm{m}$.

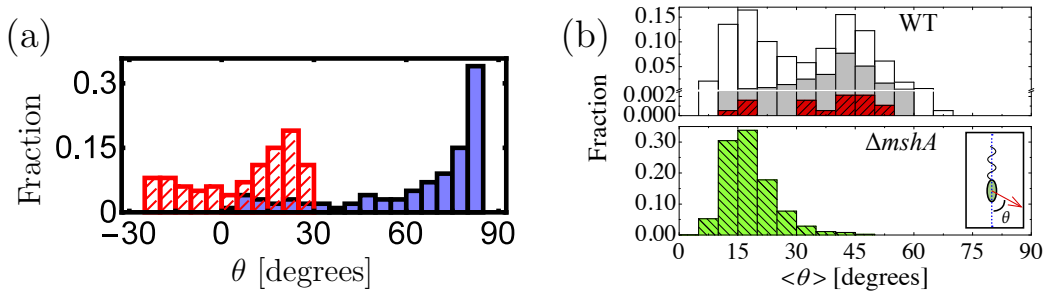


Figure 2.6: Angles between cell orientation and swimming direction: (a) distribution of angles in the model for roaming cell $\gamma = 0.002$ (red) and orbiting cell $\gamma = 0.1$ (blue); (b) distribution of swimming angles observed in WT cells (orbiting: grey, roaming: red) and mutant $\Delta mshA$ (green), measured by Andrew Utada and reproduced with his permission.

2.2.2 Swimming angle

Figures 2.4(b,c) show that there is a non-zero angle between the swimming direction and the cell orientation that varies over a head rotation cycle. The experimental observations also find variation in angle between the cell orientation and swimming direction along the trajectory. Figure 2.6 shows the distribution of angles in the model and the distribution of observed angles in WT and $\Delta mshA$ cells.

Observations of WT cells show a bimodal distribution, with one peak at a small angle corresponding to the single peak that occurs for the mutant $\Delta mshA$, and another peak that occurs at a large angle. In the model, when the pili friction is small, $\gamma = 0.002$ the distribution of angles is spread about zero with a small mean of 7.4° and a maximum angle of 25.8°. When the pili friction is large, $\gamma = 0.1$, there is a wide range of swimming angles with a large mean of 63.6° and a peak near the maximum value of 84.0°. These results show that a larger pili interaction leads to a higher swimming angle, suggesting that the large angle peak observed in WT cells is due to the interaction of the pili with the surface, while comparison with the $\Delta mshA$ mutant suggests that the the small angle peak in WT cells corresponds to the swimming angle when the pili do not interact with the surface (for example, when the pili point away from the surface).

If we use constant pili friction instead of time dependent friction in the model, then the radius of curvature results are the same, but there is a smaller spread of swimming angles. A spread of angles is observed in WT cells, suggesting that the friction between the pili and the surface varies as the cell head rotates.

2.3 Discussion

Experimental observations of WT *V. cholerae* show two distinct motility modes: many cells are orbiting and move repetitvely around small circles and a few cells are roaming and meander further across the surface. These two motility modes are not observed in $\Delta mshA$, a mutant lacking MSHA pili. We have developed a hydrodynamic model that includes an interaction between the pili and the surface. There is a nonlinear dependence of the average radius of curvature of the trajectory on the pili interaction strength, which leads to the two motility types in cell populations with a range of interaction strengths. Interaction strength varies with parameters including distance from surface, number and distribution of pili, length and thickness of pili, impurities on the surface. The model also demonstrates that the spread of swimming angles arises from the varying friction between the pili and the surface as the cell rotates.

These results are interesting when considering biofilm formation. Reversible attachments are observed for roaming and orbiting cells, but these pauses have higher frequency and longer duration for orbiting cells than roaming cells, as expected when the surface interaction is stronger [40]. Irreversible attachments are observed in orbiting cells. *V. cholerae* does not have surface motility modes, unlike the model organism *Pseudomonas aeruginosa*. *P. auruginosa* use their TFP to move across a surface using 'walking' or 'crawling' motility [54] and they follow Psl trails to organise into microcolonies [56]. Surface motility has not been observed in *V. cholerae*, so how does it organise into biofilms? The observations described in section 2.1 and the model we have developed suggests that *V. cholerae* could use its near surface motility modes: roaming motility can be used to explore the surface, and in regions where surface interactions are strong, orbiting motility can be used to scan a small patch of surface. Further stages of biofilm formation are discussed in reference [53].

The model demonstrates that friction between the pili and the surface gives the two motility modes. The model is robust and we find that changes in the head shape or a time-independent pili friction also produce the two motility modes, however there are limitations to the model. We notice discrepancy between experiments and the model in the spread of swimming angles, shown in figure 2.6. In experimental observations, we find similar bimodal distributions of swimming angles between orbiting and roaming cells and a narrower distribution with a single peak for the mutant $\Delta mshA$. In the model, the distribution of swimming angles for an orbiting cell has a larger range than for the roaming cell and the centre of the distribution is at a larger angle for the orbiting cell than for the roaming cell. The model could be improved by

using higher order hydrodynamics, for example using slender body theory instead of resisitve force theory. Another improvement would be to consider the entire length of pili filaments, also using slender body theory. It would be interesting to investigate further the interaction between the pili and the surface. Here, we have considered hydrodynamic friction, but specific interactions with particular molecules on the surface and the effects of electrostatic repulsion could have a different form to the friction we have included in the model.

To test whether the orbiting and motility modes are due to the friction between pili and the surface, a similar experiment could be performed, but tracking cells that swim further from the surface. For example, if cells that are 1 - 3 μm from the surface are tracked, the surface interaction would be weaker so we expect to see more cells roaming and fewer cells orbiting. If the distance between the cells and the surface is larger than the pili length, then we expect to see the same behaviour in WT cells and $\Delta mshA$ cells, however, we would also lose other hydrodynamic surface effects, for example circular swimming and cells would not stay at a constant height above the surface.

Another way to test the model without losing other hydrodynamic effects would be an experiment that could accurately measure the distance from the surface simultaneously with the tracking just above the surface. We predict that cells swimming closer to the surface are orbiting cells and that cells further from the surface are more likely to be roaming cells. It would be even more interesting if an experiment could be performed where the interaction strength between the pili and the surface could be measured simulateously with the tracking, but this would be more challenging to perform.

Chapter 3

Shewanella at a surface

Tracking experiments by Wong's lab show *Shewanella* cells moving at a surface [58]. Surface motility is important for understanding the initial stages of biofilm formation and detachment. In this chapter we develop a hydrodynamic model with surface constraints to understand how these different types of behaviour occur. In the previous chapter we studied the near surface motility of freely swimming *V. cholerae*, but here we study bacteria that is attached to the surface by its flagellum. Detachment of *Shewanella* from a biofilm has been studied and hydrodynamic flow which provides oxygen induces rapid detachment of cells from the biofilm [135]. The effects of changes in oxygen and other nutrients have been considered [136, 137], but hydrodynamic effects are not well studied. In this chapter we show how hydrodynamics are important for a variety of behaviours in cells attached to a surface.

3.1 Experimental observations

The experimental results we describe here were produced by Calvin Lee. *Shewanella oneidensis* were cultured overnight then injected into a sterile flow cell. The bacteria were imaged for 5-20 minutes at 30°C with a high speed camera collecting bright-field images at 200 frames per second.

The videos that were produced show different types of behaviour when the cells are constrained by the surface. The observed behaviour includes the following: (i) free swimming close to the surface; (ii) the cell lies along the surface and twitches but does not move; (iii) the cell lies parallel to the surface and rotates in the surface plane with occasional changes of rotation direction; (iv) the cell transitions from lying down to standing up and rotates faster when standing; (v) the cell rotates while standing up then lies down again (reverse of (iv)); (vi) the cell rotates while standing up then detaches from the surface; (vii) the cell comes down from above the surface

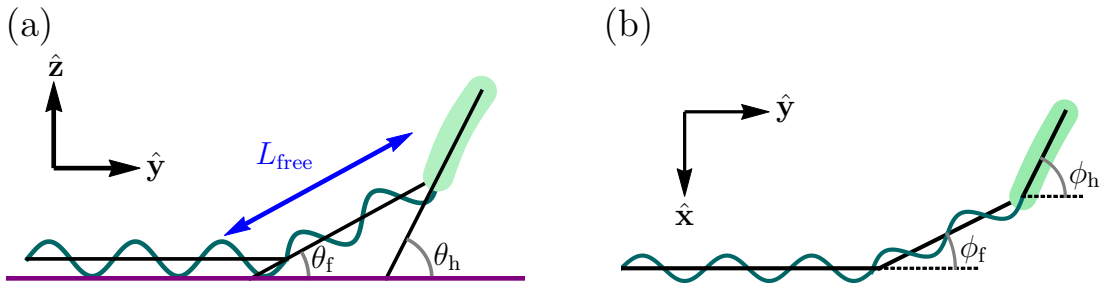


Figure 3.1: Model of *Shewanella* with part of flagellum stuck to a surface. (a) The free part of the flagellum of length L_{free} makes angle θ_{f} with surface and head makes angle θ_{h} with surface. (b) The model from above the surface: projecting into the surface plane the free part of the flagellum makes an angle ϕ_{f} with the stuck part of the flagellum, which we define as the $\hat{\mathbf{y}}$ axis, and the head makes an angle ϕ_{h} with the $\hat{\mathbf{y}}$ axis.

and attaches in an upright position (reverse of (vi)); (viii) the cell continues to rotate in an upright position; (ix) the cell swims parallel to the surface and attaches parallel to the surface; (x); the cell lies parallel to the surface then detaches horizontally.

3.2 The Model

We consider a similar model to the hydrodynamic model of *Vibrio cholerae* described in section 2.2, but with the following differences: (i) the angle between the flagellum axis and the head axis is no longer fixed and there is a torsional spring acting to align the head and flagellum; (ii) part of the flagellum is stuck to the surface and the free part of flagellum can make an angle with the fixed part of the flagellum which also has a spring acting to align the free part with the fixed part; (iii) we do not consider the effect of pili; (iv) *Shewanella* is less curved than *V. cholerae*, so we use a smaller helix radius for the head.

Figure 3.1 shows the model. Part of the helical flagellum is fixed to the surface and does not move. The remaining length of the flagellum can bend away from the fixed part of the flagellum and a torsional spring acts to align the free part of the flagellum with the fixed part of the flagellum. By considering the flagellum as a bent rod, the spring constant varies with the free length of flagellum as $k_{\text{f}} = \kappa / L_{\text{free}}^2$, where κ is constant and L_{free} is the free length of flagellum [138]. We choose the $\hat{\mathbf{y}}$ axis to lie along the axis of the fixed part of the flagellum and we define the directions of the free part of flagellum and the head as $\hat{\mathbf{n}}_{\text{f}}$ and $\hat{\mathbf{n}}_{\text{h}}$ respectively. The angle that the free part of the flagellum makes with the fixed part of the flagellum is χ_{f}, where $\cos\chi_{\text{f}} = \hat{\mathbf{y}} \cdot \hat{\mathbf{n}}_{\text{f}}$. The angle that the head makes with the free part of the flagellum is χ_{h}, where $\cos\chi_{\text{h}} = \hat{\mathbf{n}}_{\text{f}} \cdot \hat{\mathbf{n}}_{\text{h}}$. The angles that the flagellum and head make with

the surface are $\theta_\mathrm{f}, \theta_\mathrm{h}$ and are shown in figure 3.1(a). The free part of the flagellum and head can also rotate about the $\hat{\mathbf{z}}$ axis (normal to the surface) and the angles of rotation about $\hat{\mathbf{z}}$ are $\phi_\mathrm{f}, \phi_\mathrm{h}$, as shown in figure 3.1(b). We also consider the case where the flagellum is constrained only by a point at its end, so it can rotate about its own axis (an additional degree of freedom) but cannot translate.

The flagellar motor rotates the flagellum counterclockwise (CCW) relative to the head. Since the flagellum is constrained by the surface, the torque exerted by the motor rotates the head. The total torque on the head cell head is

$$\mathit{\Gamma}_\mathrm{h} = -\mathbf{M}_\mathrm{h}\mathbf{v}_\mathrm{h} + \mathit{\Gamma}\hat{\mathbf{n}}_\mathrm{h} - k_\mathrm{h}\frac{\hat{\mathbf{n}}_\mathrm{f} \times \hat{\mathbf{n}}_\mathrm{h}}{|\hat{\mathbf{n}}_\mathrm{f} \times \hat{\mathbf{n}}_\mathrm{h}|} = 0, \tag{3.1}$$

where $\mathbf{M}_\mathrm{h}$ is the mobility matrix of the head, $\mathbf{v}_\mathrm{h}$ is the angular velocity of the head, $\mathit{\Gamma}$ is the torque exerted by the flagellar motor and k_h is the spring constant of the torsional spring between the head and flagellum which is related to the flexibility of the flagellar hook. We calculate the mobility matrix using both resistive force theory and results for a rotating cylinder near a wall [29, 36, 139].

The total torque on the free part of the flagellum is

$$\mathit{\Gamma}_\mathrm{f} = -\mathbf{M}_\mathrm{f}\mathbf{v}_\mathrm{f} - \mathit{\Gamma}\hat{\mathbf{n}}_\mathrm{h} + k_\mathrm{h}\frac{\hat{\mathbf{n}}_\mathrm{f} \times \hat{\mathbf{n}}_\mathrm{h}}{|\hat{\mathbf{n}}_\mathrm{f} \times \hat{\mathbf{n}}_\mathrm{h}|} - k_\mathrm{f}\frac{\hat{\mathbf{y}} \times \hat{\mathbf{n}}_\mathrm{f}}{|\hat{\mathbf{y}} \times \hat{\mathbf{n}}_\mathrm{f}|} + \mathit{\Lambda}\hat{\mathbf{n}}_\mathrm{f}, \tag{3.2}$$

where $\mathit{\Lambda}$ is the constraint imposed by the fixed part of the flagellum that prevents the flagellum from spinning about its own axis. We solve for the angular velocities of the free part of the flagellum and the cell head using the torque free condition on the head and the torque free condition on the combined head and flagellum in the directions perpendicular to $\hat{\mathbf{n}}_\mathrm{f}$ (i.e. in the directions perpendicular to the constraining torque). We include a short range repulsive potential with the surface to prevent the head and free part of the flagellum from crashing into the surface.

The parameters we use in the model are as follows. Flagellum wavelength: 2μm; total flagellum length: 10μm; flagellum filament thickness: 0.02μm; flagellum helix radius: 0.4μm; head wavelength: 4.4μm; total head length 2.2μm; head filament thickness: 0.3μm; head helix radius 0.1μm. The behaviour varies depending on the ratios $k_\mathrm{f}/\mathit{\Gamma}$ and $k_\mathrm{h}/\mathit{\Gamma}$. We choose $\kappa/\mathit{\Gamma} = 40$ and L_free varies between 0 and L_T, where L_T is the total flagellum length. We vary $k_\mathrm{h}/\mathit{\Gamma}$ between 0.05 and 25.

3.3 Results of model

The angle that the free part of the flagellum makes with the surface, θ_f, and the angle that the head makes with the surface, θ_h, are shown in figure 3.2 for different

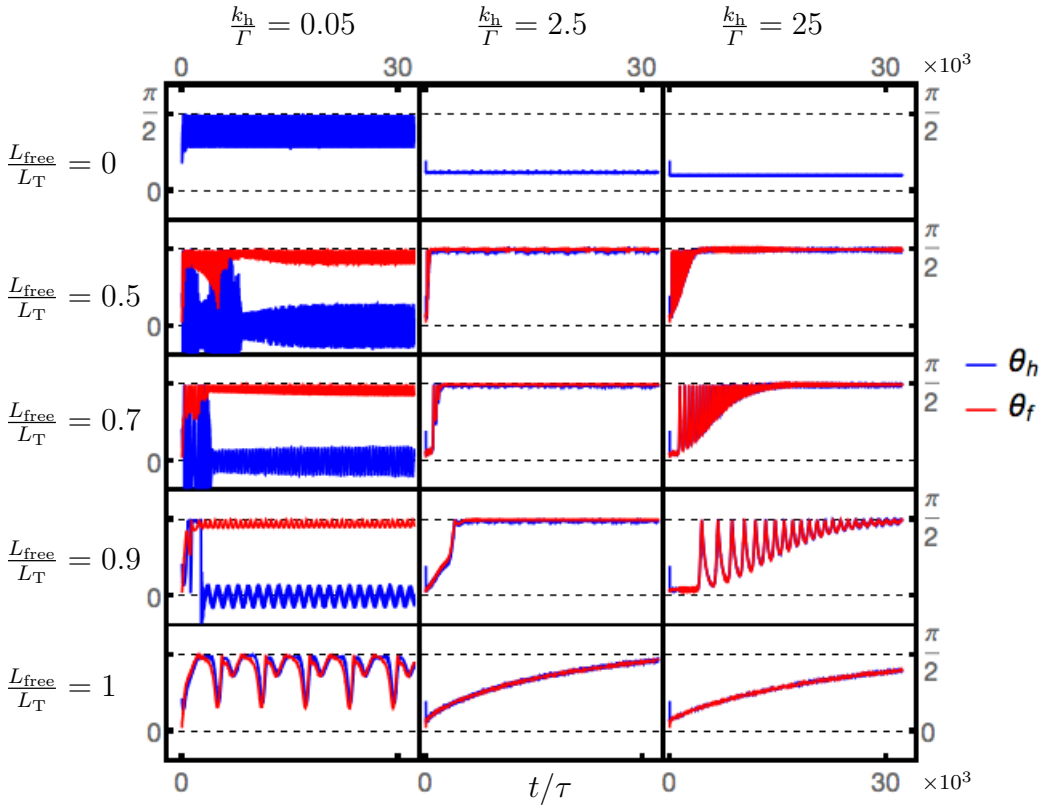


Figure 3.2: Angles between free part of the flagellum and surface (red) and cell head and surface (blue). From top to bottom row: $L_{\text{free}}/L_{\text{T}} = 0$, so flagellum is completely stuck to surface; $L_{\text{free}}/L_{\text{T}} = 0.5$, so half of the flagellum is stuck to the surface; $L_{\text{free}}/L_{\text{T}} = 0.7$; $L_{\text{free}}/L_{\text{T}} = 0.9$; $L_{\text{free}}/L_{\text{T}} = 1$, so flagellum is stuck only by point at end and is completely free to rotate but cannot translate. From left column to right column: $k_{\text{h}}/\Gamma = 0.05$, $k_{\text{h}}/\Gamma = 2.5$, $k_{\text{h}}/\Gamma = 25$. The timescale τ is the hydrodynamic timescale $\tau = 4\pi\eta L_{\text{h}} r_{\text{h}}^2/\Gamma \sim 0.001$s.

flagellar constraints and for different values of k_h. In many cases when the flagellum is partially constrained, the free part of the flagellum stands up and makes an angle $\pi/2$ with the surface, and the time that the flagellum takes to stand increases with increasing k_h/Γ.

When the flagellum is completely stuck the behaviour depends on k_h/Γ. From the top row of figure 3.2 we see that when $k_\mathrm{h}/\Gamma = 0.05$ the cell head makes a large oscillating angle with the surface and when $k_\mathrm{h}/\Gamma = 2.5, 25$ the head makes a small angle with the surface which we find to depend on the strength of surface repulsion. We see another important difference in behaviour when we consider rotation about the $\hat{\mathbf{z}}$ axis, as shown in figure 3.3(a,b). We find that for $k_\mathrm{h}/\Gamma = 0.05$ the cell head rotates about the $\hat{\mathbf{z}}$ axis but for $k_\mathrm{h}/\Gamma = 2.5, 25$ the head does not rotate about the $\hat{\mathbf{z}}$ axis and just spins about its own axis while pointing in a fixed direction.

If the flagellum is completely free to rotate, then for $k_\mathrm{h}/\Gamma = 2.5, 25$ the angle that both the head and the flagellum make with the surface gradually increases at a rate that decreases with increasing k_h/Γ. While the head and flagellum stand up they rotate slowly about the $\hat{\mathbf{z}}$ axis. When $k_\mathrm{h}/\Gamma = 0.05$ the angle that both the head and the flagellum make with the surface oscillates. There is also rotation about the $\hat{\mathbf{z}}$ axis, resulting in the interesting trajectory shown in figure 3.3(e).

Figure 3.3 shows the three-dimensional motion of the cell and free part of the flagellum for the different types of behaviour we have identified. In figure 3.3(a) the flagellum is completely fixed and the spring constant between the head and flagellum is small so the cell head can rotate about the $\hat{\mathbf{z}}$ axis. The angle between the head and the surface oscillates between large angles which reduce drag due to the surface, and medium angles which reduce the spring torque. In figure 3.3(b), the spring constant is large and prevents the cell head from standing up or rotating about $\hat{\mathbf{z}}$ so the head stays close to the surface and just spins about its own axis.

In figure 3.3(c) a small part of the flagellum is constrained by the surface. The free part of the flagellum stands upright, while the angle that the head makes oscillates. The angle between the free part of the flagellum and the fixed part is $\pi/2$, which seems large, however it allows the flagellum to rotate about $\hat{\mathbf{z}}$ without the free part of the flagellum approaching an even larger angle close to π. The length of the upright flagellum keeps the head far from the surface and $\frac{k_\mathrm{h}}{\Gamma}$ is small, allowing the angle between the head and the flagellum to oscillate. When $\frac{k_\mathrm{h}}{\Gamma} = 2.5$, the head remains aligned with the flagellum and they both stand up to make an angle $\pi/2$ with the surface, as shown in figure 3.3(d).

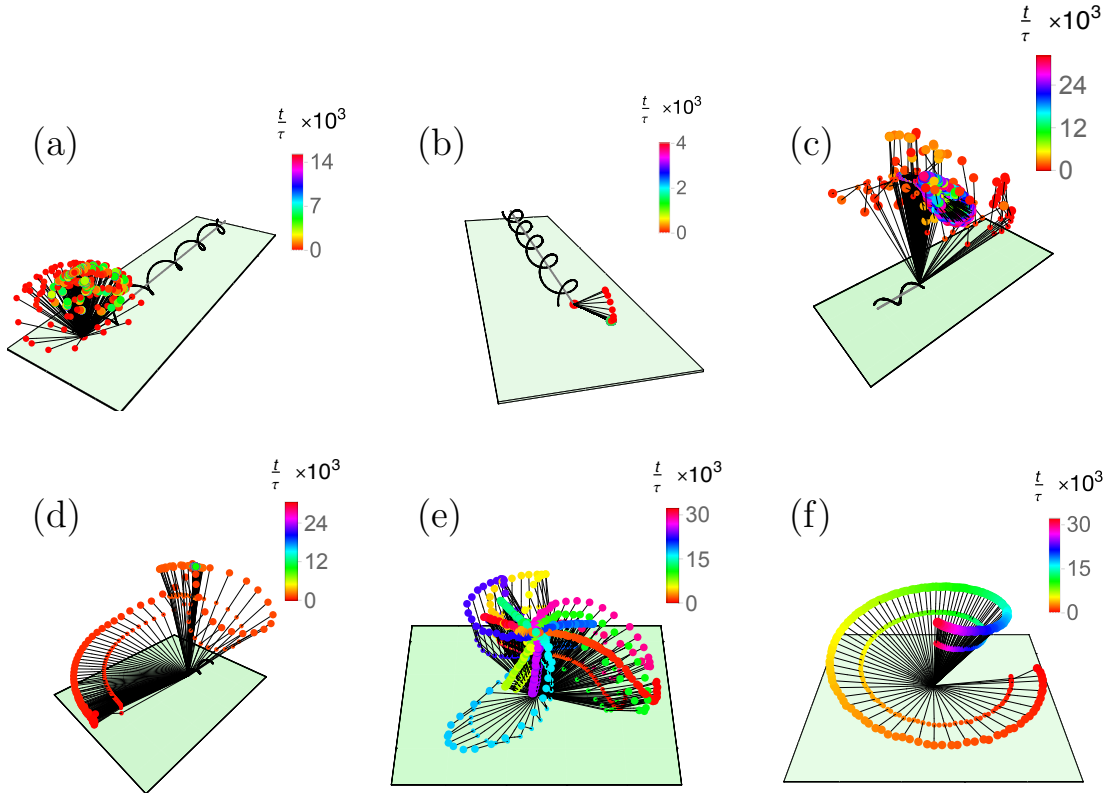


Figure 3.3: Trajectories of *Shewanella* model with partially stuck flagellum. (a) $\frac{L_{\text{free}}}{L_{\text{T}}} = 0$ and $\frac{k_{\text{h}}}{\Gamma} = 0.05$; (b) $\frac{L_{\text{free}}}{L_{\text{T}}} = 0$ and $\frac{k_{\text{h}}}{\Gamma} = 25$; (c) $\frac{L_{\text{free}}}{L_{\text{T}}} = 0.7$ and $\frac{k_{\text{h}}}{\Gamma} = 0.05$; (d) $\frac{L_{\text{free}}}{L_{\text{T}}} = 0.7$ and $\frac{k_{\text{h}}}{\Gamma} = 2.5$; (e) $\frac{L_{\text{free}}}{L_{\text{T}}} = 1$ and $\frac{k_{\text{h}}}{\Gamma} = 0.05$; (f) $\frac{L_{\text{free}}}{L_{\text{T}}} = 1$ and $\frac{k_{\text{h}}}{\Gamma} = 25$. The black lines represent the axis of the head and the flagellum at snapshots in time. The end of the flagellum at each snapshot is shown by a small coloured spot and the end of the head is shown by a larger coloured spot, where the colours correspond to the time of the snapshot.

Figures 3.3(e,f) show the behaviour when the flagellum is completely free to rotate and is only constrained from translation by a point at the end of the flagellum.When $k_{\text{h}}/\Gamma = 25$ the head and the flagellum slowly stand up while rotating about the $\hat{\mathbf{z}}$ axis. When $k_{\text{h}}/\Gamma = 0.05$ the head and flagellum remain aligned and they follow an interesting trajectory, repeatedly moving close to the surface then standing upright and repeating this pattern while they move around the $\hat{\mathbf{z}}$ axis.

3.4 Discussion

In this chapter we have considered behaviour observed in *Shewanella* when it is close to a surface but not forming a biofilm. We have developed a hydrodynamic model that considers different degrees of constraint on the flagellum - completely constrained, par-

tially constrained with bending between free and constrained parts of the flagellum, and completely free to rotate but constrained from translation.

The model produces different types of behaviour when we vary how much of the flagellum is stuck to the surface and when we vary the ratio k_{h}/Γ. It is unlikely that the flexibility of the flagellar hook, which determines k_{h}, varies much between cells, but it is possible that the torque exerted by the flagellar motor, Γ, varies. Features in the behaviour that we reported in section 3.1 are observed in our model, as shown in section 3.3. Our model shows the different types of oscillations in the angle with the surface while rotating about the $\hat{\mathbf{z}}$ axis; the head lying down and rotating about its own axis, which gives a wobbling effect when viewed from above; the head and flagellum both standing upright and spinning; the head and flagellum slowly standing up. When viewed on shorter time scales the behaviour shown in figure 3.3(f) could look like rotations while lying down or rotations while partially standing, depending on the time at which the cell is viewed and the initial condition.

Transitions between the different types of behaviour occur when there is a change in the proportion of the flagellum that is stuck to the surface. Changes in rotation direction are observed which occur when the flagellar motor reverses its direction. If the motor also changes the magnitude of the torque it exerts then changes in behaviour can occur. The flagellar attachment we have considered here is reversible and not sufficient to form biofilms; the process of flagellar attachment is beyond the scope of this model.

We have not considered the effect of pili which attach the head to the surface and are essential for biofilm formation [60]. Chapter 2 showed that pili also play an important in near surface motility so it would be interesting to develop the model further by adding pili to understand how pili hydrodynamics effect the behaviour.

The model could be further improved by using the higher order slender body theory instead of resistive force theory. When the bacteria stand upright and most of their body is far from the surface, the higher order terms are not important, but when the cell lies close to the surface then the higher order effects could be more significant. It would be interesting to study the effects of Brownian noise, since *Shewenalla* has a head length of $\sim 3\mu$m and Brownian motion is important on this length scale.

The model produces also produces a similar variety of behaviours when we change the curvature of the head - either more curved to model *Vibrio cholerae*, or a straight rod to model *Pseudomonas aeruginosa*. In future work we plan to compare the results of the model with different curvatures with observations of *V. cholerae* and *P. aeruginosa*. Initial observations suggest that the model produces the behaviour

observed in all three bacteria and correctly predicts the orientation before detachment for the different curvatures [58]. Measurements of the flexibility of the flagella and the hooks and torques exerted by the different bacteria would test the validity of the model: the model must produce the observed behaviour for measured value of the parameters.

We have shown that transitions between different types of behaviour can occur when there is a change in how much of the flagellum is stuck to the surface. We have not investigated how parts of the flagellum attach or detach from the surface. It would be interesting to see experimental observations of the flagellum at the same time as the spinning of the head to see if there are changes in the proportion of the flagellum that is stuck at the same time as transitions in the spinning behaviour.

Chapter 4

Simple model of *Chlamydomonas*: Synchronisation and run-and-tumble

Chlamydomonas swims by beating its two flagella synchronously and is a model organism for synchronisation. *Chlamydomonas* has a cell body diameter of $\sim 10\mu$m so is less susceptible to rotational diffusion than bacteria, but it swims along a random walk following run-and-tumble behaviour [67]. The cell runs in a straight line when the flagella beat synchronously, and short asynchronies cause the cell to tumble.

Flagella are well represented as Stokeslets and previous models have studied the hydrodynamic synchronisation of two fixed rotors [88, 89, 93, 98]. However, we find that the rotation dynamics are important for synchronisation so we develop a free model that considers rotation and translation of the cell. We find that the stability of synchronisation is sensitive to the beat pattern and show that run-and-tumble behaviour emerges from intrinsic noise [99]. Goldstein *et al.* developed a model to study noise and hydrodynamic synchronisation in *Chlamydomonas*, however they do not consider rotation dynamics and they compare their model with cells held fixed on micropipettes [140].

4.1 The Model

Measurements of the flow field around *Chlamydomonas* are well represented by three Stokeslets [141, 142]. Inspired by these measurement, we model *Chlamydomonas* with three spheres: one that represents the cell body, and two that represent the flagella and move around circular trajectories relative to the cell body [99, 100]. Each flagellar bead is driven by a tangential driving force. Hydrodynamic synchronisation between

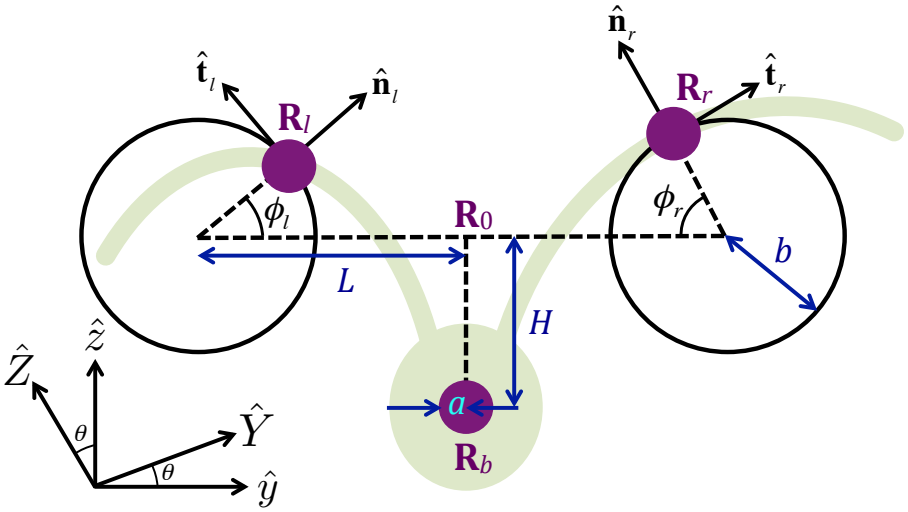


Figure 4.1: Three-sphere model of *Chlamydomonas*: The flagella are represented by beads moving around circular trajectories of radius b and a third bead models the cell body. The black scaffold does not interact with the fluid. The cell frame $\hat{y}, \hat{z}$ makes an angle θ with the lab frame $\hat{Y}, \hat{Z}$. The green underlay shows a schematic of a *Chlamydomonas* cell with its two flagella in the plane of the page.

two beads moving on rigid trajectories requires phase dependent forcing [88, 89] or flexibility in the trajectories [93], so we use a phase dependent driving force in our model. Although the trajectories of the flagellar beads are fixed relative to the cell body, translation and rotation of the entire body provide an alternative degree of flexibility and rotation of the body is sufficient for synchronisation [90].

Figure 4.1 shows the model. The cell body bead and left and right flagellar beads are at positions $\mathbf{R}_\mathrm{b}, \mathbf{R}_\mathrm{l}, \mathbf{R}_\mathrm{r}$, respectively. The positions and velocities of the three beads are

$$\mathbf{R}_\mathrm{l} = \mathbf{R}_0 - L\hat{\mathbf{y}} + b\hat{\mathbf{n}}_\mathrm{l}, \qquad \dot{\mathbf{R}}_\mathrm{l} = \dot{\mathbf{R}}_0 + L\dot{\theta}\hat{\mathbf{z}} + b(\dot{\phi}_\mathrm{l} - \dot{\theta})\hat{\mathbf{t}}_\mathrm{l}, \tag{4.1}$$

$$\mathbf{R}_\mathrm{r} = \mathbf{R}_0 + L\hat{\mathbf{y}} + b\hat{\mathbf{n}}_\mathrm{r}, \qquad \dot{\mathbf{R}}_\mathrm{r} = \dot{\mathbf{R}}_0 - L\dot{\theta}\hat{\mathbf{z}} + b(\dot{\phi}_\mathrm{r} + \dot{\theta})\hat{\mathbf{t}}_\mathrm{r}, \tag{4.2}$$

$$\mathbf{R}_\mathrm{b} = \mathbf{R}_0 - H\hat{\mathbf{z}}, \qquad \dot{\mathbf{R}}_\mathrm{b} = \dot{\mathbf{R}}_0 - H\dot{\theta}\hat{\mathbf{y}}. \tag{4.3}$$

where $\mathbf{R}_0$ is the origin of the cell reference frame, $\hat{\mathbf{n}}_i$ and $\hat{\mathbf{t}}_i$ are the normal and tangent directions of the circular trajectory of bead $i = \mathrm{l}, \mathrm{r}$. The left and right beads are driven by tangential forces $F_\mathrm{l}^\mathrm{t}(\phi_\mathrm{l})$ and $F_r^\mathrm{t}(\phi_\mathrm{r})$ respectively. Normal forces F_l^n and F_r^n constrain the beads to the circular trajectories. Since there are no external forces or torques, we have the force free and torque free conditions

$$\mathbf{F}_\mathrm{l} + \mathbf{F}_\mathrm{r} + \mathbf{F}_\mathrm{b} = 0, \qquad \mathbf{T}_\mathrm{l} + \mathbf{T}_\mathrm{r} + \mathbf{T}_\mathrm{b} = 0, \tag{4.4}$$

where $\mathbf{F}_i = F_i^t\hat{\mathbf{t}}_i + F_i^n\hat{\mathbf{n}}_i$ for $i = l, r$ and $\mathbf{T}_j = \mathbf{R}_j \times \mathbf{F}_j$ for $j = \mathrm{b}, \mathrm{l}, \mathrm{r}$. The cell is at low Reynolds number $Re \sim 10^{-3}$ so the velocities are linearly related to the forces:

$$\dot{\mathbf{R}}_\mathrm{l} = \tfrac{1}{\xi}\mathbf{F}_\mathrm{l} + (\mathbf{G}_\mathrm{lr} - \mathbf{G}_\mathrm{lb}) \cdot \mathbf{F}_\mathrm{r} - \mathbf{G}_\mathrm{lb} \cdot \mathbf{F}_\mathrm{l}, \tag{4.5}$$

$$\dot{\mathbf{R}}_\mathrm{r} = \tfrac{1}{\xi}\mathbf{F}_\mathrm{r} + (\mathbf{G}_\mathrm{rl} - \mathbf{G}_\mathrm{rb}) \cdot \mathbf{F}_\mathrm{l} - \mathbf{G}_\mathrm{rb} \cdot \mathbf{F}_\mathrm{r}, \tag{4.6}$$

$$\dot{\mathbf{R}}_\mathrm{b} = -\tfrac{1}{\xi}(\mathbf{F}_\mathrm{l} + \mathbf{F}_\mathrm{r}) + \mathbf{G}_\mathrm{bl} \cdot \mathbf{F}_\mathrm{l} + \mathbf{G}_\mathrm{br} \cdot \mathbf{F}_\mathrm{r}, \tag{4.7}$$

where $\xi = 6\pi\eta a$ is the Stokes friction coefficient of each bead and η is the viscosity of the fluid. In the limit where the bead radius, a, is small compared with the other length scales, b, L, H, the hydrodynamic interactions are included using Oseen tensor $\mathbf{G}_{ij} = \frac{1}{8\pi\eta|\mathbf{r}_{ij}|}(\mathbf{I} + \hat{\mathbf{r}}_{ij}\hat{\mathbf{r}}_{ij})$, where $\mathbf{r}_{ij} = \mathbf{r}_i - \mathbf{r}_j$ [95].

From equations (4.1), (4.2), (4.3), (4.4), the phase difference $\delta = \phi_r - \phi_l$ evolves as

$$\begin{aligned}\dot{\delta} = \quad & \tfrac{1}{b}\Bigg[(\dot{\mathbf{R}}_r - \dot{\mathbf{R}}_b) \cdot \hat{\mathbf{t}}_r - (\dot{\mathbf{R}}_l - \dot{\mathbf{R}}_b) \cdot \hat{\mathbf{t}}_l + \\ & 2\dot{\theta}\Big(\cos(\delta/2)\big(L\cos\phi - H\sin\phi\big) - b\Big)\Bigg],\end{aligned} \tag{4.8}$$

where $\phi = (\phi_l + \phi_r)/2$, and the orientation of the cell, θ, follows

$$\begin{aligned}\dot{\theta} = \quad & \tfrac{1}{2}\Bigg[\frac{(\dot{\mathbf{R}}_l - \dot{\mathbf{R}}_b)\cdot\hat{\mathbf{n}}_l}{H\cos(\phi - \delta/2) + L\sin(\phi - \delta/2)} - \\ & \frac{(\dot{\mathbf{R}}_r - \dot{\mathbf{R}}_b)\cdot\hat{\mathbf{n}}_r}{H\cos(\phi + \delta/2) + L\sin(\phi + \delta/2)}\Bigg].\end{aligned} \tag{4.9}$$

We solve equation (4.8) numerically for different choices of beat patterns $F_i^t(\phi_i)$, $i = \mathrm{l}, \mathrm{r}$. The long term behaviour of the phase difference, δ, depends on the beat pattern and the initial condition.

4.2 Swimming velocity in the synchronised state

First, let's consider the swimming velocity in the synchronised state where $F_l^t(\phi) = F_r^t(\phi)$ and $\delta = 0$, so that $\phi_l = \phi_r = \phi$. We will consider the stability of the synchronised state in the next section, and for now assume that the swimmer remains synchronised. We are in the low Reynolds number regime, so it is not immediately obvious if this model can achieve net propulsion. Without hydrodynamic interactions, the cell moves forwards during the power stroke and backwards during the recovery stroke by the same amount so there is no net motion. Hydrodynamic interactions are weaker in the power stroke when the beads are further away from each other than in

the recovery stroke when the beads are close together; if hydrodynamic interactions are included the symmetry in the swimming stroke is broken and net propulsion is achieved. With hydrodynamic interactions, the cell moves backwards and forwards, but the displacement in one half of the cycle is greater than the displacement in the opposite direction in the other half of the cycle. This backwards and forwards motion is observed in swimming *Chlamydomonas* cells [143].

The magnitude and direction of the net swimming velocity depend on the geometric parameters H/b and L/b. Figure 4.2 shows the net swimming velocity in the $\hat{z}$ direction for a range of parameters $(H/b, L/b)$ with a constant driving force $F^t(\phi) = F_0$. When $L \gtrsim 2.25|H|$, the cell swims forwards, otherwise the cell swims backwards. Polotzek and Friedrich explain why the cell can swim in either direction in reference [102]: The instantaneous velocity $v = f/g$ is the ratio of the force $-f\hat{z}$, which is required to prevent the back bead from moving, and the friction coefficient g of forcing the swimmer in the $\hat{z}$ direction. The force f oscillates during a stroke cycle and also varies with hydrodynamic interactions which are strongest when the beads are closest together, and which reduce the magnitude of f. The friction coefficient g is largest when the beads are furthest apart. The effect that dominates, and therefore the net swimming direction, depends on geometry. Herein we fix the geometric parameters to the values $a/L = 1/33, H/b = 1/5$ and $L/b = 2$, which gives forwards swimming for $F_0 > 0$.

The force profile also affects the net swimming velocity. We consider driving forces

$$F^t(\phi) = F_0(1 + \sum_{n=1}^{\infty} a_n \cos(n\phi) + b_n \sin(n\phi)) \tag{4.10}$$

with $|a_n|, |b_n| < 1$. The net velocity, $\bar{v}$, is $\bar{v} = 1/T \int_0^T \mathrm{d}t \dot{R}_b = 1/T \int_0^T \mathrm{d}t \dot{R}_b = 1/T \int_0^{2\pi} \mathrm{d}\phi \dot{R}_b(\phi)/\dot{\phi}(\phi)$, where $\dot{R}_b = \dot{\mathbf{R}}_b \cdot \hat{\mathbf{y}}$, $T = \int_0^{2\pi} \mathrm{d}\phi/\dot{\phi}$ is the period. In the synchronised state the force dependence cancels in the ratio $\dot{R}_b/\dot{\phi}$, so the force only enters the net velocity expression through the $1/T$ term. We maximise the net velocity by minimising the period $T = \int_0^{2\pi} \mathrm{d}\phi/\dot{\phi}(\phi)$, where $\dot{\phi}(\phi) = F^t(\phi)\Phi(\phi)$. Minimising T for a fixed F_0 tells us that constant forcing $F^t(\phi) = F_0$ maximises the net velocity. However, in section 4.3 we show that the synchronised state is unstable when we have constant forcing in the forwards direction.

4.3 Synchronisation and stability

We consider force profiles in the form of equation (4.10). Here, our definition of the synchronised state is that the phase difference is zero (or integer multiples of 2π),

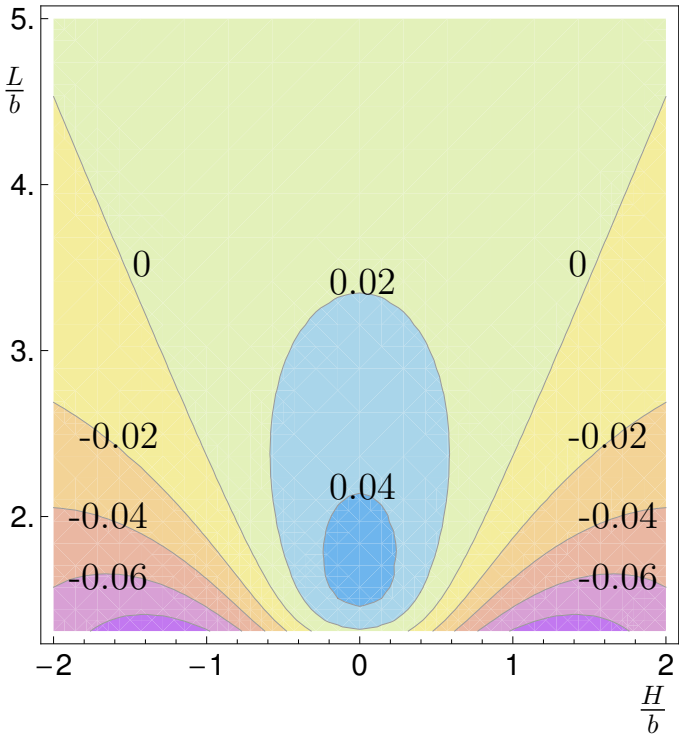


Figure 4.2: Contour plot showing how net swimming velocity varies with the geometric parameters. Labels on the contours show velocities in units of $F_0/(6\pi\eta b)$. For sufficiently large H/b, the zero contour follows $L = 2.25|H|$.

$\delta = 2\pi n$, $n \in \mathbb{Z}$. A first idea is to use linear stability analysis to analyse the stability of synchronisation, but we are unable to do this because we cannot perform a valid Taylor expansion when $H\cos\phi + L\sin\phi = 0$; for further details see appendix A. Instead, we solve the equations numerically and observe the long time behaviour for different initial conditions and force profiles.

For a given force profile and initial condition, the phase difference either evolves into the synchronised state, $\delta = 0$, or the phase difference evolves into a state that oscillates about a non-zero value. A surprising result is that there are force profiles and initial conditions that evolve into the synchronised state when we do not include hydrodynamic interactions. The synchronisation is caused by the rotation of the cell: a phase difference results in rotation of the cell body and the Stokes friction on each bead is proportional to the velocity, so the friction that each bead feels either increases or decreases depending on the direction of rotation [90, 102, 104]. Hydrodynamic interactions are a second order effect. The synchronisation results that we present in this chapter neglect hydrodynamic interactions. However, when we consider trajectories of the cell, we need to include hydrodynamic interactions because they are required to break time reversal symmetry and allow the cell to swim forwards.

We categorise force profiles into five classes of synchronisation stability to identify general features in the behaviour. There is a range of stabilities and we choose to divide force profiles into stability classes in the following way: For a particular force profile we look at how δ evolves from initial conditions $\delta(\phi_0) = 0.1$ with 24 equally spaced ϕ_0 in the range $\phi_0 \in [0, 2\pi)$, where ϕ_0 is the initial average phase. We then assign one the following stability types: (i) All the initial conditions $\delta(\phi_0) = 0.1$ evolve into the synchronised state for all ϕ_0 (stable synchronisation). (ii) Most initial conditions lead to the synchronised state. This type of stability is assigned when the number of initial conditions leading to the synchronised state is 14 - 23 out of the 24 which are tested. (iii) There are similar numbers of initial conditions which lead to the synchronised state and to an oscillating state. This type of stability is assigned when the number of initial conditions leading to the synchronised state is 11 - 13 out of the 24 which are tested. (iv) Most initial conditions lead to an oscillating state. This type of stability is assigned when the number of initial conditions leading to the synchronised state is 1 - 10 out of the 24 which are tested. (v) All tested initial conditions, ϕ_0, evolve into an oscillating state.

The choice of initial condition $\delta_0 = 0.1$ is arbitrary and we have chosen it because we want to know how likely it is that a small perturbation from the synchronised state

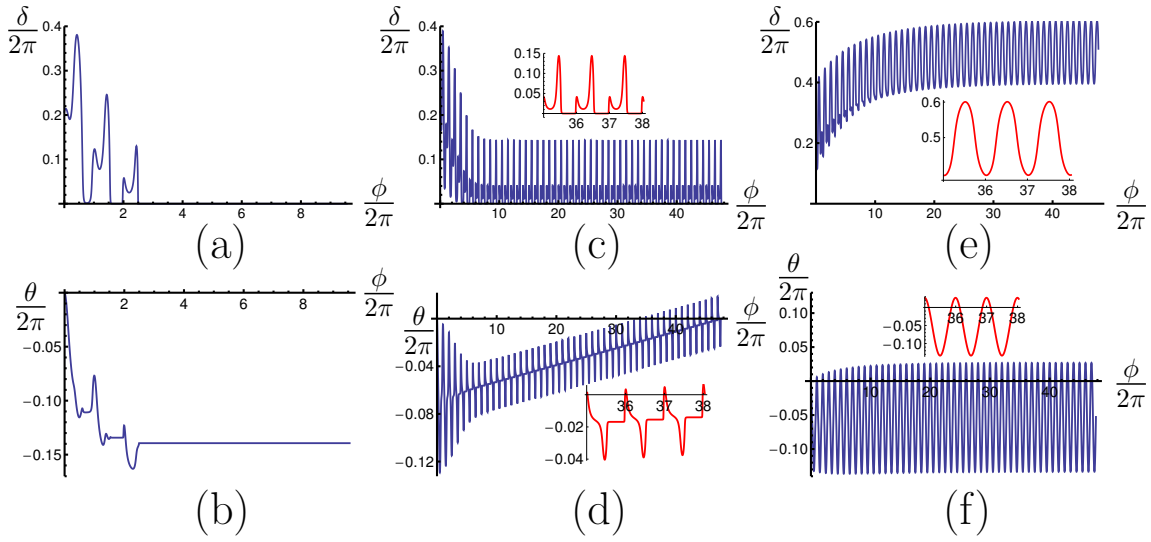


Figure 4.3: Evolution of (a,c,e) phase difference, δ, and (b,d,f) corresponding orientation, θ, for driving force $F^t(\phi) = F_0(1+b^{(1)}\sin\phi)$ and initial condition $\delta(\phi = 0) = 1.3$ with (a,b) $b^{(1)} = 0.7$, (c,d) $b^{(1)} = 0.4$, (e,f) $b^{(1)} = -0.1$. The insets show the shape of the oscillations. The horizontal axis $\phi/2\pi$ is the number of cycles, which increases monotonically with time.

will decay back to synchronisation, or whether it is likely to evolve into an oscillating state. The choice $\delta_0 = 0.1$ is suitable for this purpose.

4.3.1 Equal beat patterns

We consider the case where the left and right beads follow the same stroke pattern $F_l^t(\phi) = F_r^t(\phi)$. For each choice of coefficient and initial condition, we see three general types of long term behaviour: δ evolves to an integer multiple of 2π and remains at that value (synchronisation); δ reaches a state where it oscillates sinusoidally about an odd integer multiple of π; or δ oscillates close to zero, but never reaching zero. Figure 4.3 shows examples of these three behaviours with the corresponding orientation, θ, with an initial condition $\delta(\phi = 0) = 1.3$. In these examples, $\delta \geq 0$ because we start with an initial condition $\delta_0 > 0$ and $\delta = 0$ is a fixed point. If $\delta = 0$ is a stable fixed point then when δ reaches zero it remains in the synchronised state. If $\delta = 0$ is an unstable fixed point, then an initial condition $\delta_0 > 0$ never reaches zero so there is no cross over to $\delta < 0$. Figure 4.3(c) shows that δ can get very close to zero without ever quite reaching synchronisation. Noise would be required to kick δ over to $\delta < 0$ [99].

The orientation is constant during synchronised beating. When δ oscillates about π the orientation oscillates about some fixed value. The cell travels in a straight line

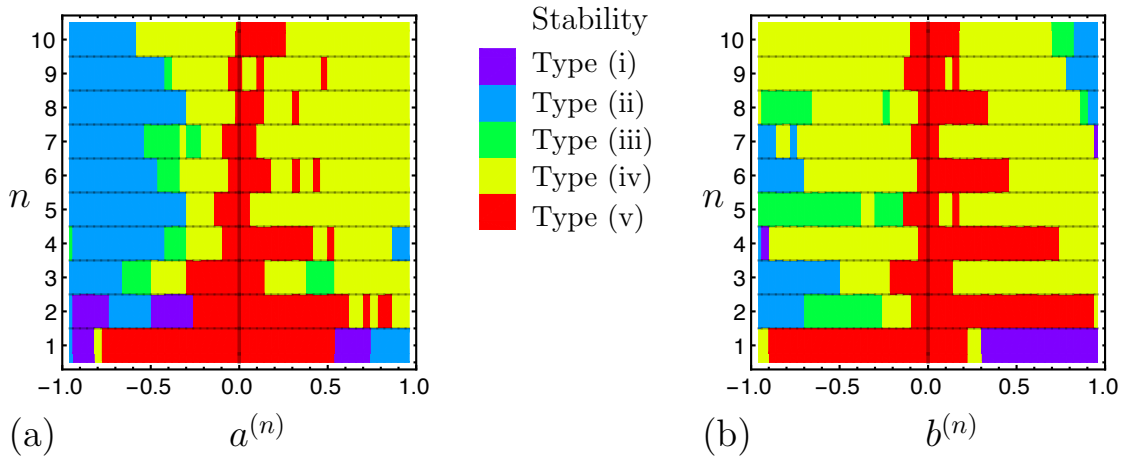


Figure 4.4: Stabilities for different harmonics and coefficients in the driving force (a) $F_i^t(\phi_i) = F_0\big(1 + a^{(n)} \cos n\phi_i\big)$ and (b) $F_i^t(\phi_i) = F_0\big(1 + b^{(n)} \sin n\phi_i\big)$. Each horizontal band corresponds to a harmonic and is broken up into 49 blocks for different coefficients $a^{(n)}$. The colour of each segment represents the stability type of that driving force. Purple - stability (i); blue - stability (ii); green - stability (iii); yellow - stability (iv); and red - stability (v). (Stability types defined at beginning of section 4.3.)

on average, but the cell swings from side to side as well as backwards and forwards within each beat cycle. When $b^{(1)} = 0.4$, the oscillations are close to zero and there is net drift in the orientation; on average the cell moves along a curved trajectory.

Figure 4.4 shows the stability of the synchronised state for the first 10 harmonics for a discrete range of coefficients, using the five classes we defined above. In the first 10 harmonics we see more type (i) and type (ii) behaviour for the cosine harmonics in figure 4.4(a) than for the sine harmonics in figure 4.4(b). Let us now focus on the cosine harmonics in figure 4.4(a). There are more type (i) and (ii) force profiles for negative coefficients than for positive, so evolution into the synchronised state is more likely if a negative coefficient is chosen than if a positive coefficient is used. We see that for $n > 2$ there is no type (i) behaviour, so synchronisation is susceptible to disruption from noise at these higher harmonics. The unstable type (v) band around $a^{(n)} = 0$ gets narrower as n increases, so only weak phase dependence is required for the possibility of synchrony being reached from a non-zero initial δ. However, at these higher harmonics only a small number of initial conditions lead to the synchronised state and noise could easily drive the system away from synchrony. The stability tends to increase as $|a^{(n)}|$ increases for each harmonic, although there are a few exceptions. For example, when $n = 1$ and $a^{(1)} > 0$, if we start with $a^{(1)}$ in the type (i) region, then as $a^{(1)}$ increases we move into a type (ii) region. Also, for $n = 3$ and $a^{(3)} > 0$, there is a type (iii) region surrounded by type (iv) regions on both sides.

The red band of type (v) stability down the centre of figure 4.4 shows that some form of phase dependence is required in order to achieve synchronisation. If the driving force is constant, then δ evolves into an oscillating state for all initial conditions and even if we start in the synchronised state, a small amount of numerical noise can drive the system away from synchrony. Friedrich *et al.* showed that a constant driving force can give stable synchronisation if the beads rotate backwards, $F_0 < 0$ [90, 102], which is equivalent to changing the sign of H with $F_0 > 0$. When there is a phase difference, the cell rotates so that the net torque is zero. The direction of cell rotation depends on the force profile and the positions of the beads; if the position of the back bead is moved from $H \to -H$, then the direction of cell rotation needed to balance the torque is reversed. Force is proportional to velocity at low Reynolds number, so cell rotation affects the hydrodynamic friction that each bead feels, and for small phase difference the friction increases on one bead and decreases on the other bead, causing one bead to slow down and the other to speed up along its trajectory [104]. If friction increases on the leading bead and decreases on the trailing bead, then synchrony is restored, but if friction decreases on the leading bead and increases on the trailing bead, then the cell moves away from synchronisation. Reversing the direction of cell rotation reverses the change in friction on each bead, therefore changes whether the system restores or moves away from synchrony. Here we choose $F_0 > 0$ and $H > 0$, to represent the flagella beating ahead of the cell body, as observed in *Chlamydomonas*.

4.3.2 Initial conditions

The initial conditions determine the long term behaviour for many choices of $F^t(\phi)$. Figure 4.5 shows how the long term behaviour of δ depends initial condition for force profiles $F^t(\phi) = F_0(1+a^{(1)}\cos\phi)$. We use a 63×69 grid with each square representing an initial condition (ϕ_0, δ_0). An initial condition for which $\delta \to 0$ after a sufficiently long time is marked with a black square; an initial condition for which δ oscillates periodically as $t \to \infty$ is marked with a black square.

When $a^{(1)} = 0.4$, all initial conditions evolve to an oscillating state; the synchronised state is unstable (type (v)). In figure 4.5(a), we many squares along the line $\delta = 0$ are white, so an initial condition in the synchronised state is driven into an oscillating state by a small amount of numerical noise. There are white squares on the line $\delta_0 = 2\pi$, however this is because the grid does not lie exactly on the 2π line: the grid contains points $\delta = 6.2$ and $\delta = 6.3$ and this small deviation from the synchronised state $\delta = 2\pi$ is enough for evolution into an oscillating state for a few

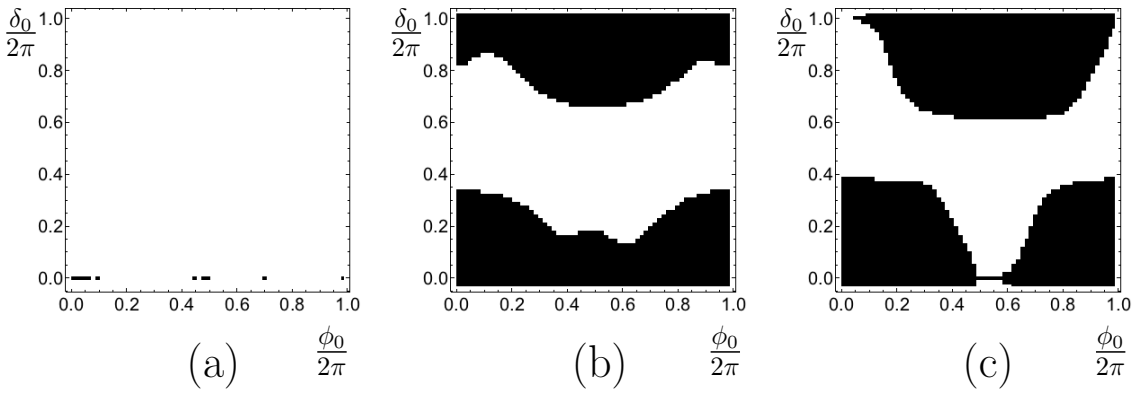


Figure 4.5: Phase diagrams showing the evolution of the phase difference, δ, for different initial conditions for $F^t(\phi) = 1 + a^{(1)} \cos\phi$ with (a) $a^{(1)} = 0.4$, (b) $a^{(1)} = 0.6$, (c) $a^{(1)} = 0.8$. Black squares show initial conditions which lead to the synchronised state and white squares show initial conditions which lead to a periodic oscillating state. The stability of the synchronised state is: (a) type (v) unstable; (b) type (i) stable; (c) type (ii) - synchronisation is unstable in a small part of the cycle.

choices of ϕ_0. For $a^{(1)} = 0.6$, if the initial phase difference is small then it evolves into the synchronised state and if the initial phase difference is large then it evolves into an oscillating state (type (i) stability). For $a^{(1)} = 0.8$, initial phase differences close to $\delta = 0$ evolve into the synchronised state for most ϕ_0, but there is a small range of ϕ_0 where a phase difference close to $\delta = 0$ evolves into an oscillating state (type (ii) stability). In an oscillating state the cell can still swim, but it also jiggles from side to side.

In figure 4.6 we show the full initial condition phase diagrams for examples of force profiles that show each type of stability. In the type (i) stable case, oscillating states can still evolve (see also figure 4.5), but only if the initial difference is sufficiently far from $\delta = 0, 2\pi$. In a few cases we find all initial conditions lead to the synchronised state, for example, the force profile $F^t(\phi) = F_0(1 + b^{(1)} \sin\phi)$ for $b^{(1)} \gtrsim 0.6$.

4.3.3 Combinations of harmonics

So far we have considered force profiles with a single harmonic. Now let's consider driving forces with contributions from two harmonics. For simplicity we consider equal profiles, $F_l^t(\phi) = F_r^t(\phi)$, of the form $F^t(\phi) = F_0(1 + a^{(m)} \cos m\phi + a^{(n)} \cos n\phi)$, $m \neq n$ and with the $a^{(i)}$'s satisfying $F^t(\phi) > 0$ for all $\phi \in \mathbb{R}$. The stability of the synchronised state for $m = 1, n = 2$ and $m = 1, n = 3$ is shown in figure 4.7. Each grid square corresponds to a driving force with coefficients $(a^{(1)}, a^{(j)})$, $j = 2, 3$ and the colour represents the stability of the synchronised state for each driving force.

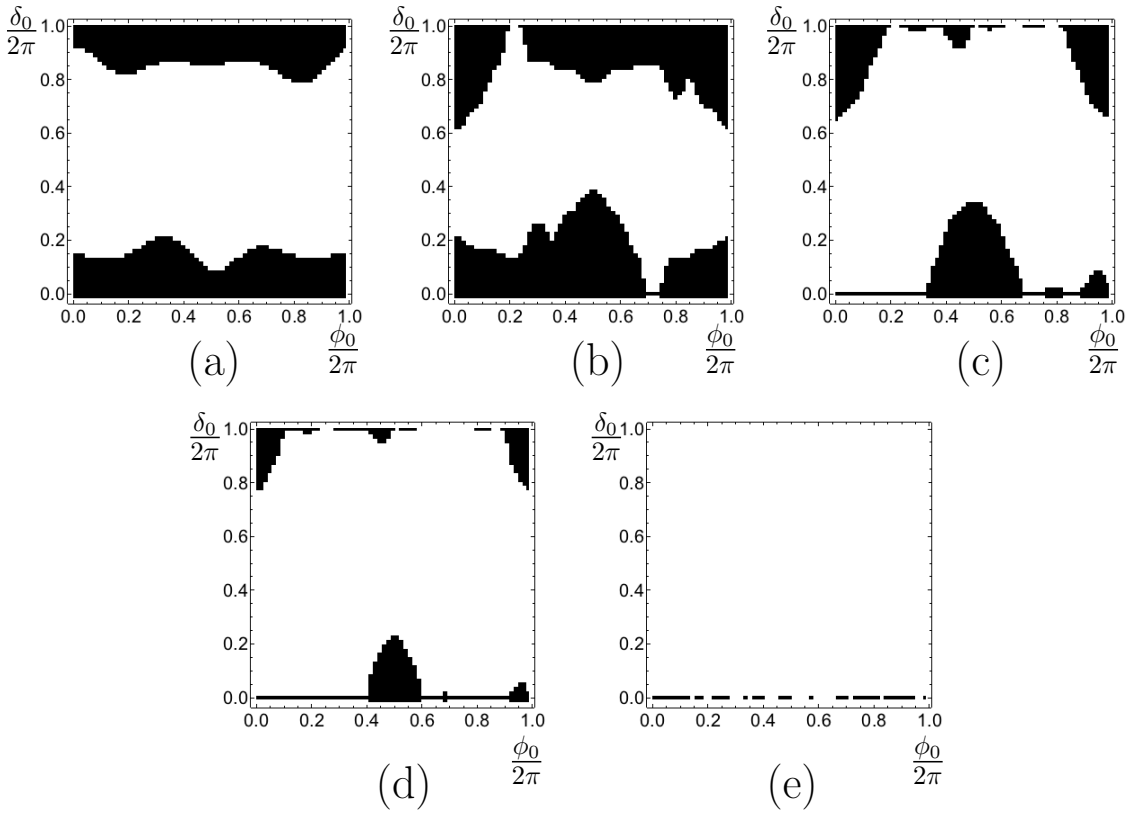


Figure 4.6: Initial condition phase diagrams showing examples of each stability type with force profile $F^t(\phi) = F_0(1 + a^{(n)} \cos n\phi)$. (a) Type (i) stable: $n = 2$ and $a^{(n)} = -0.44$. (b) Type (ii) stability: $n = 7$ and $a^{(n)} = -0.8$. (c) Type (iii) stability: $n = 7$ and $a^{(n)} = -0.44$. (d) Type (iv) stability: $n = 8$ and $a^{(n)} = -0.24$. (e) Type (v) stability: $n = 6$ and $a^{(n)} = -0.04$. The horizontal axis is the initial average phase and the vertical axis is the initial phase difference.

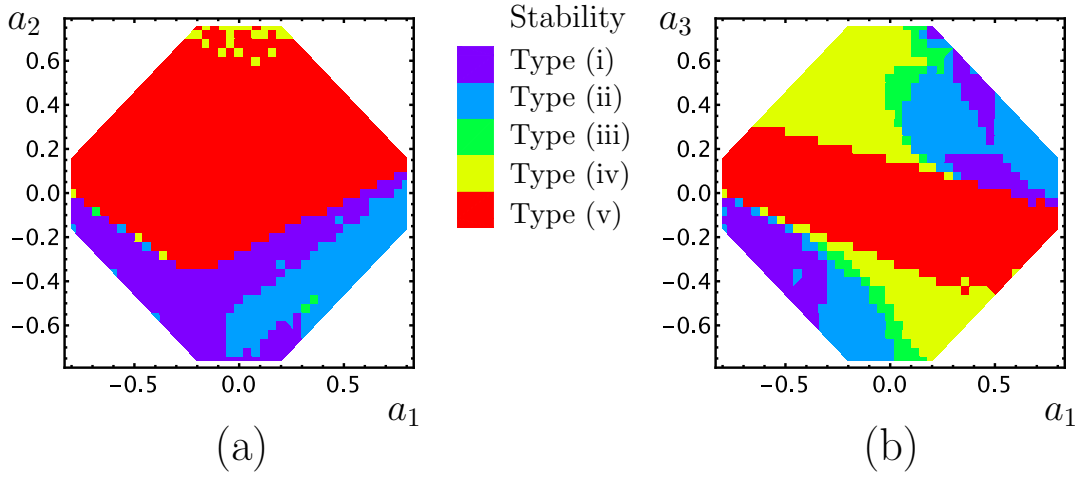


Figure 4.7: Phase diagrams showing stability of synchronised state for force profiles with two harmonics (a) $F^t(\phi) = F_0(1 + a^{(1)} \cos\phi + a^{(2)} \cos 2\phi)$, (b) $F^t(\phi) = F_0(1 + a^{(1)} \cos\phi + a^{(3)} \cos 3\phi)$. The colour of each square represents the stability type: Purple - type (i); blue - type (ii); green - type (iii); yellow - type (iv); red - type (v).

There are large regions for which the synchronised state is type (i) stable. Adding the second or third harmonic increases the range of values of $a^{(1)}$ which give stable synchronisation, with stronger additional harmonics (i.e. larger $|a^{(2,3)}|$) having an increased effect on the range of stable choices of $a^{(1)}$. We see that for all values of $a^{(1)}$, with the exception of large $a^{(1)}$, we need $a^{(2)} \leq 0$ for a stable synchronised state. If we use the third harmonic then we require $a^{(3)} \leq 0$ when $a^{(1)} \leq 0$ and $a^{(3)} \geq 0$ when $a^{(1)} \geq 0$ for a stable synchronisation.

4.3.4 Mismatched coefficients

Now let's consider $F_l^t(\phi) \neq F_r^t(\phi)$. If we start in the synchronized state, then

$$\left.\frac{\mathrm{d}\delta}{\mathrm{d}\phi}\right|_{\delta=0} = \left(\frac{F_l^t - F_r^t}{F_l^t + F_r^t}\right)\Phi(\phi),$$

which is non-zero for $F_l^t \neq F_r^t$, so the system moves away from synchrony. Let's focus on the first harmonic, $n = 1$, and consider the case $F_l^t = F_0(1 + a_l \cos\phi_l)$ and $F_r^t = F_0(1 + a_r \cos\phi_r)$ where $a_l \neq a_r$ (and we have dropped the upper index on the coefficient). There are three cases to consider: equal magnitudes and opposite signs; equal signs and different magnitudes; opposite signs and different magnitudes.

When $a_l = -a_r$ and $|a_i| \gtrsim 0.6$, synchronisation is frustrated and δ oscillates about $2\pi n$, $n \in \mathbb{Z}$, as shown in figure 4.8(a) for $-a_l = a_r = 0.7$. Figure 4.8(b) shows that the orientation of the cell drifts, so the cell swims along a curved trajectory. For

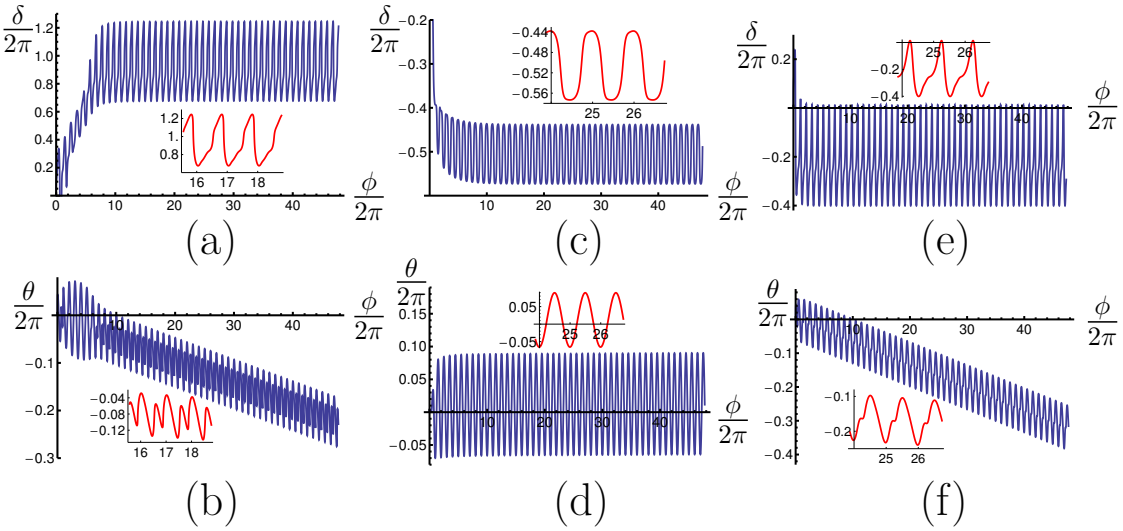


Figure 4.8: Mismatched coefficients: (a), (c), (e) Evolution of δ and (b), (d), (f) corresponding orientation θ for force profiles $F_i^t(\phi_i) = F_0(1 + a_i \cos\phi_i)$ and initial conditions $\delta(\phi = 0) = 0$, $\theta(\phi = 0) = 0$ and with (a), (b) $-a_l = a_r = 0.7$; (c), (d) $a_l = 0.7, a_r = 0.8$; (e), (f) $a_l = -0.7, a_r = 0.8$. Each inset shows the shape if the oscillations.

$|a_i| < 0.6$, oscillations in δ are not centred on the synchronised state. Changing the signs of the coefficients switches the direction of the drift in orientation.

When the coefficients have equal sign but different magnitudes, δ oscillates about $(2n+1)\pi$ and the orientation oscillates. Figure 4.8(c) shows the evolution of δ for $a_l = 0.7, a_r = 0.8$. This is similar to the behaviour for some choices of equal coefficients, for example, in figure 4.3(e), (f) where $b_l^{(1)} = b_r^{(1)} = -0.1$. Coefficients that give this type of behaviour can be used to model antiphase beating which is seen in a mutant of *Chlamydomonas*, *ptx1* [144]. The beat frequency of antiphase beating in the model is higher than in-phase beating, which has also been observed in *ptx1* cells.

When the coefficients have opposite signs and different magnitudes, we see two distinct types of behaviour. For $|a_l| < |a_r|$ and $\mathrm{sgn}(a_l) = -1$ or $|a_r| < |a_l|$ and $\mathrm{sgn}(a_r) = -1$, δ oscillates periodically and the orientation drifts in the negative direction for the case $|a_l| < |a_r|$ and in the positive direction for the case $|a_r| < |a_l|$. Figure 4.8(e), (f) shows this behaviour for $a_l = -0.7, a_r = 0.8$. For $|a_l| < |a_r|$ and $\mathrm{sgn}(a_l) = +1$ or $|a_r| < |a_l|$ and $\mathrm{sgn}(a_r) = +1$, the phase difference also drifts. When $|a_l| < |a_r|$ and $\mathrm{sgn}(a_l) = +1$ the oscillations in δ drift in the negative direction and the orientation drifts in the positive direction. When $|a_r| < |a_l|$ and $\mathrm{sgn}(a_r) = +1$ the oscillations in δ drift in the positive direction and the orientation drifts in the negative direction. Figure 4.9 shows examples of the drift in phase difference, where

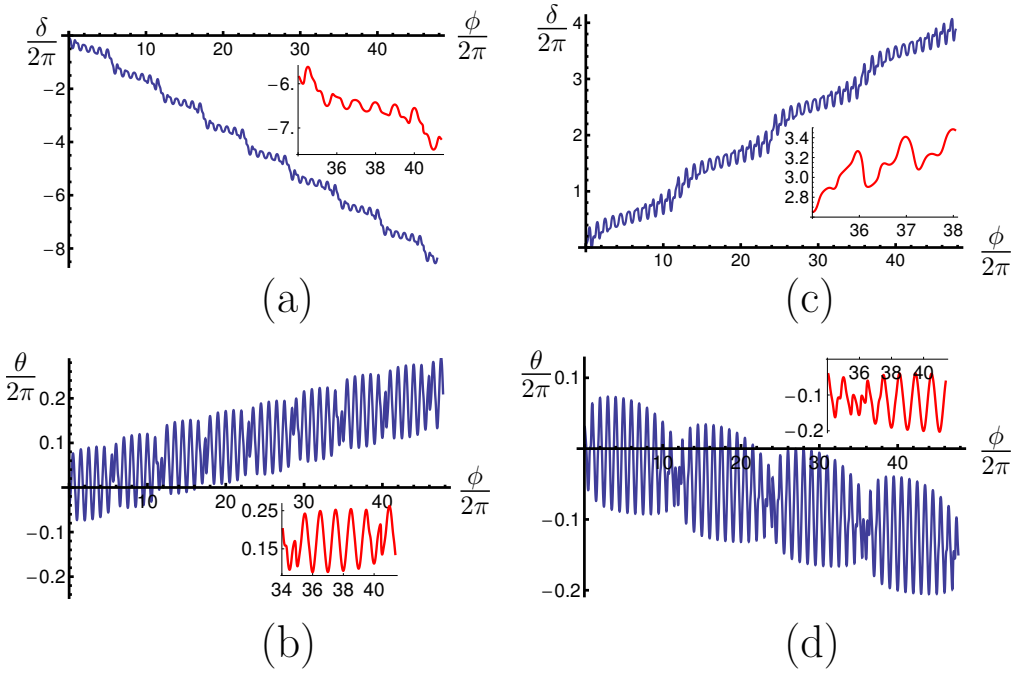


Figure 4.9: Evolution of phase difference and orientation for mismatched coefficients that give drifting δ with (a), (b) $F_l^t = F_0(1 + 0.2\cos\phi_l)$ and $F_r^t = F_0(1 - 0.6\cos\phi_r)$; (c), (d) $F_l^t = F_0(1-0.4\cos\phi_l)$ and $F_r^t = F_0(1+0.3\cos\phi_r)$. The insets show the shape of the oscillations.

one bead completes more cycles than the other bead. The beads have different mean angular velocities even though F_0 is the same for each bead.

4.4 Run-and-tumble

Figure 4.4 shows that the behaviour of the model is sensitive to the parameter $a^{(n)}$. For example, if $a^{(1)} = 0.7$ the synchronised state is stable, but if $a^{(1)} = 0.8$, we have type (ii) stability and there is a small region in each beat cycle where noise could drive the system away from synchronisation. This sensitivity provided the inspiration to use the model for run-and-tumble behaviour [99]. *Chlamydomonas* shows run-and-tumble behaviour, where the cell swims along long straight lines during synchronous beating, interspersed with short asynchronies that cause sharp changes in the orientation [67]. Here, we add white noise to the coefficient in the driving force and show that run-and-tumble behaviour emerges from the model with intrinsic noise.

We choose a driving force $F_i(\phi_i)/F_0 = 1 + (a_i + \zeta_i)\cos\phi_i$ where ζ_i is Gaussian distributed, $\langle\zeta_i(t)\zeta_j(t')\rangle = \sigma^2\delta_{ij}\delta(t-t')$, $\langle\zeta_i(t)\rangle = 0$. First we consider $a_\mathrm{l} = a_\mathrm{r}$ and choose a values so that we have stable synchronised beating in the absence of noise.

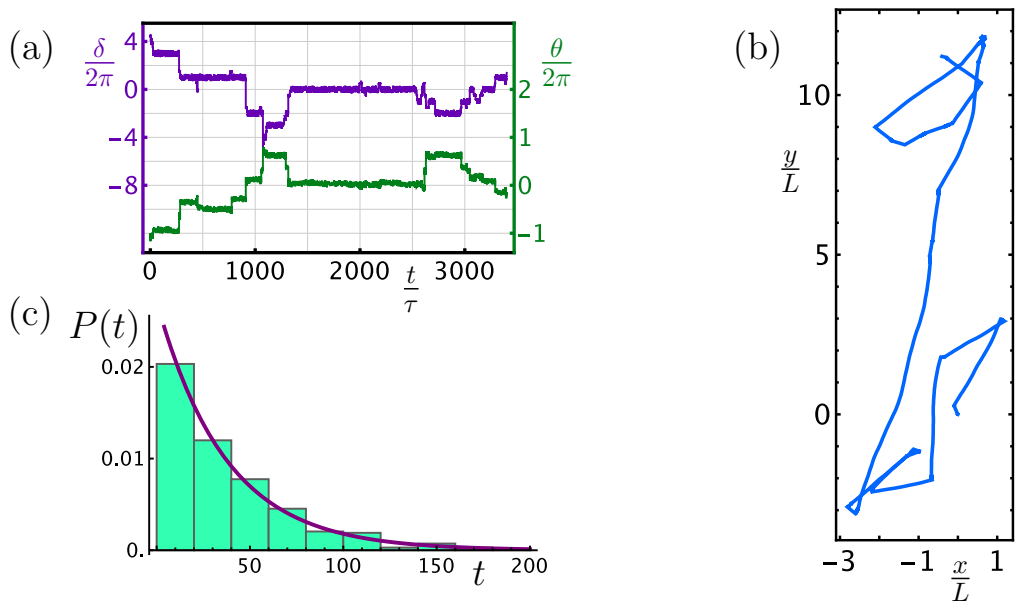


Figure 4.10: (a) Phase difference (purple) and orientation (green) for run-and-tumble cell with coefficient $a_\mathrm{l} = a_\mathrm{r} = 0.6$ and $\sigma = 4 \cdot 10^{-3}$. (b) Corresponding trajectory for the run-and-tumble cell. The characteristic length scale L is shown in figure 4.1 and the characteristic time scale is $\tau = \xi L/F_0$. (c) Distribution of run times for $a_0 = 0.6, \sigma = 10^{-2}$. Fit for histogram is $1/\tau_\mathrm{run} \exp(-t/\tau_\mathrm{run})$.

We solve the SDE numerically using Euler's scheme [145, 146]. Figure 4.10 shows the phase difference, orientation, trajectory and distribution of run durations for the cell with $a_\mathrm{l} = a_\mathrm{r} = 0.6$ and $\sigma = 3 \cdot 10^{-3}$. The phase difference oscillates about $2\pi n$ for a time τ before rapidly moving away and oscillating about $2\pi m$, with $m \neq n$, $m, n \in \mathbb{Z}$. During oscillations about $2\pi n$, the orientation is constant on average, but when the phase difference changes rapidly and moves to a new synchronised state, there is a corresponding change in the phase difference. The distribution of durations for which the cell travels in the same direction (run times), τ, decays exponentially indicating Poisson behaviour in agreement with the observations of Polin *et al.* [67], and is shown in figure 4.10(c).

In section 4.3.4 we saw that if we have coefficients with opposite signs and the same magnitude in the noiseless case, synchronisation is frustrated and the cell moves along a curved trajectory. We add noise to the case $-a_\mathrm{l} = a_\mathrm{r} = 0.6$ and find that we still get run-and-tumble behaviour, but with curved run sections. We also find run-and-tumble-like behaviour for some values of a_0 that do not give stable synchronisation in the absence of noise: we see antiphase beating during 'runs', where the cell jiggles along its trajectory, which is interrupted by 'tumbles' where the cell reorients.

4.5 Summary and discussion

We have presented a simple model of *Chlamydomonas* where the flagella are represented by beads driven around circular trajectories by phase dependent forces. *Chlamydomonas* swims at low Reynolds number and we have seen that hydrodynamic interactions break the symmetry required for net swimming, since hydrodynamic interactions are stronger in the recovery stroke than in the power stroke. The net swimming velocity depends on the geometric parameters.

Synchronisation of the flagella is sensitive to the beat pattern and we require phase dependence for stable synchronisation. We do not require hydrodynamic interactions for synchronisation; the rotation of the cell body modifies the friction that each bead feels as it moves along its trajectory, providing the flexibility required for synchronisation. When we add intrinsic noise we exploit the beat pattern sensitivity and run-and-tumble behaviour emerges. In bacteria, such as *E. coli*, discrete switches between 'runs' and 'tumbles' are controlled by chemical signals of CheY, but we have shown that run-and-tumble in *Chlamydomonas* can emerge from the nonlinear mechanics of the noisy system. Run-and-tumble behaviour in *Chlamydomonas* does not involve discrete changes in beat direction of a flagellum, instead the cell 'runs' during synchronous beating and 'tumbles' during short asynchonies [67]. Our model produces this behaviour, with sharp changes in orientation occurring when the phase difference changes rapidly.

E. coli uses run-and-tumble as a biased random walk for chemotaxis by increasing the mean run duration as it moves up a concentration gradient [110]. There is evidence for different mechanisms of chemotaxis towards different chemoattractants in *Chlamydomonas* and one of these mechanisms could be based on run-and-tumble [147]. Currently, we do not know enough about the response of *Chlamydomonas* to concentration gradients of chemoattractants to develop our model to study chemotaxis. However, we find that the average run time increases with decreasing intrinsic noise strength, and changes in concentration could affect the relative internal noise, allowing for a possible chemotaxis mechanism. *Chlamydomonas* is also a phototactic organism and we use the three-sphere model to elucidate a steering mechanism in chapter 5.

The coefficient a_0 in our model needs to be tuned to get run-and-tumble with synchronised beating during the runs and asynchronies corresponding to tumbles. However, we also find run-and-tumble-like behaviour with different 'run' characteristics for coefficients with opposite signs or for some coefficients which give antiphase

beating, suggesting that we do not need fine tuning to get stochastic tumbles.

We have considered noise in the coefficient of the driving force a_0 but another question is what would happen if we put the noise in the magnitude of the driving force, F_0? Would this also give run-and-tumble behaviour? If so, how would it change the distribution of run durations?

Hydrodynamic synchronisation of fixed rotors requires either phase dependent forcing or flexibility in the trajectories [88, 89, 93, 98]. Here, we have considered synchronisation by rotation dynamics which is a lower order effect than synchronisation by hydrodynamic interactions, and we have considered phase dependent forcing. It would be interesting to study the how flexibility affects synchronisation and run-and-tumble behaviour in our model. When solving for the phase difference we have neglected hydrodynamic interactions and it would be interesting to study their contribution and whether they affect the stability of synchronisation for different force profiles.

One of the problems we faced in this chapter was that we could not perform the linear stability analysis. This was due to the mathematical set-up of the model and not due to any underlying physical problems. This work could be improved if we used a different method of solving the model so that we could do some analytic stability calculations. For example, we could try working with different variables $\phi_i \rightarrow \Phi_i$ where the intrinsic velocity of each bead in the new variables is constant.

As we saw in chapter 2, surfaces can significantly affect the motility of microorganisms so an interesting problem would be to study this model near a boundary. How would the surface affect synchronisation? Tumbling in *E. coli* is suppressed when it swims close to a solid surface [148], so an important question is how the surface affects run-and-tumble in our model. It would also be interesting to observe experimentally *Chlamydomonas* cells at a surface to see how synchronisation and run-and-tumble dynamics are effected.

Chapter 5

Phototaxis in *Chlamydomonas*

5.1 Coupling light intensity to beat pattern

Chlamydomonas is a phototactic organism that can steer towards or away from a light source. In chapter 4, we saw that the three-sphere model of *Chlamydomonas* is useful for understanding synchronisation of the flagella and how stochastic tumbles emerge from the nonlinear mechanics when there is intrinsic noise in the beat pattern. Now we develop the model further by coupling the beat pattern to the light intensity to study phototactic steering in *Chlamydomonas*.

Rüffer and Nultsch performed experiments on fixed cells and studied two responses to light stimuli: beat frequency changes and beat amplitude changes [122, 123]. High speed films were made of cells were held on micropipettes stimulated by white light. Single step changes in light were applied and periodic irradiation at 1 or 2 Hz was also applied to simulate the rotation of free swimming cells. Both flagella show the same frequency response, either both increasing or both decreasing frequency, so frequency changes cannot steer the cell, but one flagellum increases its beat amplitude and the other flagellum decreases its beat amplitude in response to a light stimulus. Inspired by these results, we couple the amplitude of the beat pattern in our model to the light intensity seen by the cell's eyespot [101].

The eyespot is on the equator and lies 45° ahead of the flagellar beat plane (the y-z plane shown in figure 5.1). We denote the axes of the lab reference frame $(\hat{X}, \hat{Y}, \hat{Z})$ and the axes of the moving cell frame $(\hat{x}, \hat{y}, \hat{z})$. The eyespot looks in the direction $(\hat{x}+\hat{y})/\sqrt{2}$ and we choose the light source to point in the $-\hat{Z}$-direction with intensity I_0. We approximate the cell as opaque so the light seen by the eyespot is

$$I(t) = I_b + I_0 \hat{Z} \cdot (\hat{x} + \hat{y}) H\big(\hat{Z} \cdot (\hat{x} + \hat{y})\big)/\sqrt{2}, \tag{5.1}$$

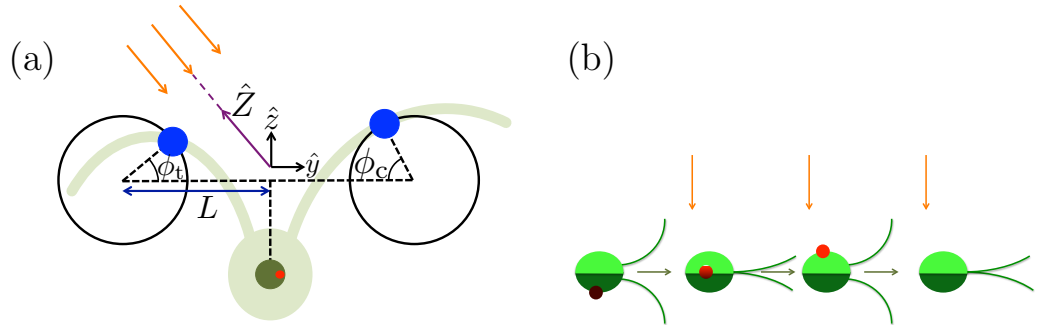


Figure 5.1: (a) The three-sphere model with incoming light: The flagella are represented by the blue beads with phase $\phi_{c,t}$, which are driven around circular trajectories by phase-dependent tangential forces. A third dark green sphere represents the cell body and the red spot indicates the position of the eyespot. The green underlay shows a schematic of the real cell, and the incoming light is represented by orange arrows. (b) The eyespot is on the equator so as the cell rotates about the z-axis it sees a varying light signal when it swims perpendicular to the light direction (orange arrows). The eyespot is shaded by the cell body for half the cycle; in the light half of the cycle the light signal varies as $\cos\vartheta$, where ϑ is the angle between the outward normal from the eyespot and the direction towards the light.

where I_b is isotropic background light and H is the Heaviside step function. The cell rotates about the z-axis as it swims forwards, so the light signal that the eyespot receives varies. The model rotates about the z-axis if we rotate the flagellar trajectories about the y-axis by a small angle in opposite directions.

The flagella are driven by a phase dependent tangential force $F(\phi_i) = F_0(1 + a_i \sin(n\phi_i + \Delta))$ where $i = \mathrm{c}, \mathrm{t}$ is the cis or trans flagellum and Δ is a constant phase. The cis flagellum is closest to the eyespot, in the $y > 0$ half-space in the cell frame, and the trans flagellum is furthest from the eyespot, in the $y < 0$ half-space. We couple the coefficient a_i to the light intensity at the eyespot

$$\begin{aligned} a_\mathrm{c} &= a_0 + p\log(1 + I(t)) + \zeta_\mathrm{c}(t), \\ a_\mathrm{t} &= a_0 - p\log(1 + I(t)) + \zeta_\mathrm{t}(t), \end{aligned} \tag{5.2}$$

where p is the coupling strength which controls how sharply the cell steers towards the light and sign(p) determines the direction of phototaxis. $I(t)$ is the intensity of light at the eyespot which varies as the cell rotates according to equation 5.1. The noise, $\zeta_i(t)$, has Gaussian probability distribution with zero mean and correlation function $\langle \zeta_i(t)\zeta_j(t')\rangle = \sigma^2\delta_{ij}\delta(t - t')$. The noise is not required for the phototactic steering mechanism we present here, but it is included to show that the mechanism is robust in the presence of noise. The noise allows the cell to run-and-tumble in the dark. We choose $a_0 = 0.6$ so that the cell swims with stable synchronised beating

in the absence of the coupling term and noise. The opposite signs on the cis and trans coupling terms in equation (5.2) are motivated by observations that the beat amplitudes of the flagella respond in opposite ways to light stimuli [123]. The light is coupled logarithmically to allow responses over a large range of light intensity and choose p such that $|a_i| < 1$.

The mismatch between the two coefficients results in an angular velocity about the x-axis that can be approximated as

$$\omega_x = \omega_0(a_\mathrm{t} - a_\mathrm{c}) + \omega_1 \tanh\left(K(a_\mathrm{t} - a_\mathrm{c})\right) \cos\left(\Omega_\mathrm{b} t\right) \tag{5.3}$$

where $K \approx 100$ and Ω_b is the flagellar beat frequency. The observed magnitude of rotation about the z-axis is $\Omega_z \approx \Omega_\mathrm{b}/20$. We also include a phase shift between light and dark, which allows the cell to steer well in the light and perform run-and-tumble in the dark: $\Delta = 0$ if $I > 0$ and $\Delta = \pi/2$ if $I = 0$. If we do not include this phase shift, so that $\Delta = 0$ in light and dark, then the characteristic run time in the dark is longer than our simulation times so we do not see run-and-tumble behaviour. If we have $\Delta = \pi/2$ in both light and dark, then the drift angular velocity, ω_0 in equation (5.3), is too small to get the steering the effect that we describe below in section 5.3. We include the phase shift to optimise the observed behaviours in light and dark conditions.

5.2 Results of the model

We choose an initial condition such that the y-z plane is parallel to the Y-Z plane. The initial angle between the cell's orientation $\hat{z}$ and the direction towards the light $\hat{Z}$ is denoted by θ_0. We find that for all initial orientations θ_0 and light intensities I_b, I_0 that satisfy $|a_{\mathrm{c,t}}| < 1$, the model steers towards the light when $p > 0$ and steers away from the light when $p < 0$. Even if we start the cell on a trajectory directly away from the light, if $p > 0$ the negative phototaxis direction is unstable and the cell steers towards the light. Similarly, when $p < 0$, if the cell starts on a trajectory towards the light then it will turn around and swim away from the light. Figure 5.2 shows example trajectories of the model showing run-and-tumble behaviour in the dark and swithcing to phototactic steering when a light source is switched on. The cell travels on a helical path when we average over a beat cycle, as shown in the inset of figure 5.2(a).

We have included noise and see that this does not prevent the cell from swimming towards or away from the light; if a tumble occurs then the cell quickly reorients

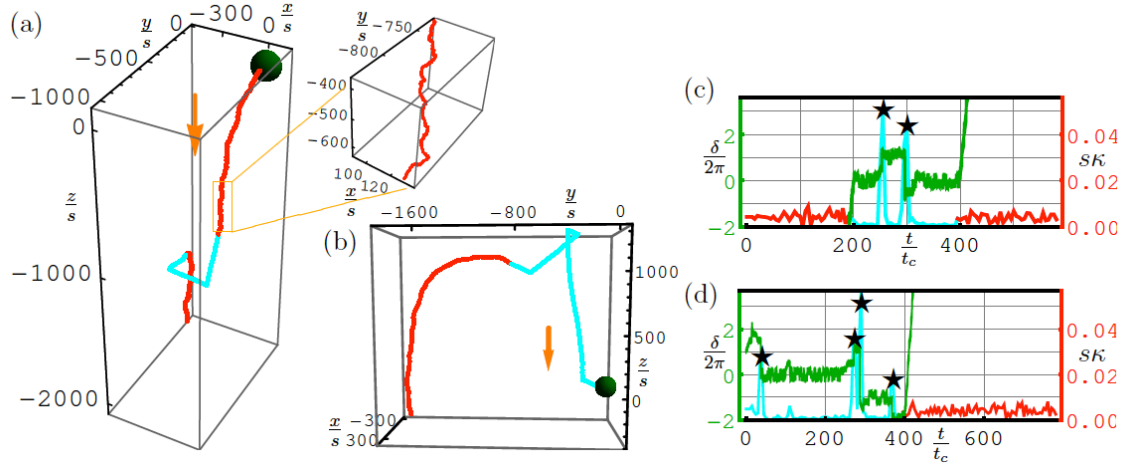


Figure 5.2: Model trajectories alternating between light and dark. The length scale L is shown in figure 5.1, where $2L$ is the average distance between flagella beads, and the time scale is $t_c = 6\pi\eta aL/F_0$, where η is the fluid viscosity and a is radius of the beads. We use parameters $p = -1$, $I_b = 0.1$, $I_0 = 0.1$, $\sigma = 4.7\text{x}10^{-3}$ and initial condition $\theta_0 = \pi/2$. (a) The light is on when $0 < t < T/3$ and $2/3T < t < T$ (red), where T is the total time of trajectory. The cell is in the dark for $T/3 < t < 2/3T$ (blue) and shows run-and-tumble behaviour. The direction of incoming light is shown by the orange arrow and the initial position of the cell is shown by the green sphere (not to scale). The helical shape of the trajectory is shown in the inset. (b) An example trajectory where the cell starts in the dark and the light is off for $t < T/2$, then the light is switched on for $t > T/2$. The duration of darkness is twice as long as in (a) and we see twice as many tumbles. (c, d) (Red/blue) Curvature of the helix axis, κ, of the trajectories shown in (a) and (b) respectively. The sharp peaks in the curvature during darkness correspond to tumbles, which is confirmed by looking at the phase difference, δ, of the beating flagella during darkness, shown by the green line. The black stars highlight the peaks in curvature and we see rapid changes in the phase difference at these points.

itself towards or away from the light again. We have tested noise strengths $\sigma \in [10^{-4}, 5\text{x}10^{-3}]$ and we find direct steering towards or away from the light with only an occasional tumble which is followed quickly by reorientation.

The model can steer effectively towards a periodic light source if the period is shorter than the characteristic run duration in the dark and longer than the rotation period. If the period is less than the characteristic run duration, then the probability of a tumble event occurring during the dark phase is small and the cell follows its path towards the light with minimal interruptions. In periodic light the initial steering of the cell towards or away from the light is slowed by dark phases, but once the cell has reached the correct orientation, short periodic dark phases do not disturb the motion towards or away from the light.

Figures 5.2(c,d) show the curvature and phase difference of the trajectories shown in figures 5.2(a,b) when we average over the helical motion and small fluctuations. When the light is on (shown in red) the curvature is small. During darkness (shown in blue) we see peaks in the curvature that correspond to the tumbles and sections where the curvature is very small curvature, which correspond to straight runs. In section 4.4 we showed that tumbles (rapid changes in orientation) occur at the same time as jumps in the phase difference. The green line in figures 5.2(c,d) shows the phase difference and we see that jumps in phase difference correspond to peaks in curvature, confirming that the peaks in curvature are tumbles in the dark.

Stronger coupling gives sharper turning towards or away from the light. This is shown in figure 5.3, where the initial bending of the trajectory towards the light is greater when p is greater. Larger values of p increase the mismatch between the cis and trans beat amplitudes, giving faster rotations about the x-axis.

5.3 Understanding the steering mechanism

Averaging over fast oscillations within a flagellar beat cycle, the cell swims along a helical path. We consider how changes in the light intensity at the eyespot causes the helix axis to bend towards or away from the light. The cell swims with time averaged linear velocity u in the $\hat{z}$-direction and angular velocities $-\Omega_z$ about the z-axis, $\Omega_z > 0$, and ω_x about the x-axis. This combination results in the cell swimming along a left-handed helix with radius $r = u|\omega_x|/\Omega_z^2$ and pitch length $\lambda = 2\pi u/\Omega_z$. The angle the cell trajectory makes with the helix axis is

$$\gamma = \tan^{-1}(2\pi r/\lambda) = \tan^{-1}(|\omega_x|/\Omega_z). \tag{5.4}$$

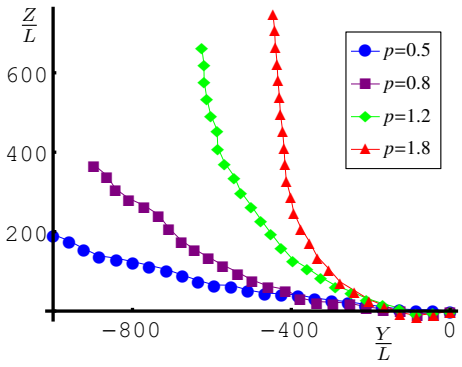


Figure 5.3: 2D projections into Y-Z plane of trajectories of the cell with different values of coupling strength p, for an initial steering time $t/t_c \leq 180$. Blue circles: $p = 0.5$; purple squares: $p = 0.8$; green diamonds: $p = 1.2$; red triangle: $p = 1.8$. Initially the cell is oriented in the $-\hat{y}$ direction, then it turns towards the light coming from the $\hat{Z}$ direction. At $t/t_c = 180$, the cells with $p = 1.2$ and $p = 1.8$ have already turned towards the light, but the cells with $p = 0.5$ and $p = 0.8$ take longer to orient and are continuing to turn towards the light.

When $\omega_x > 0$ the y-axis points in the outwards radial direction and in the inward radial direction when $\omega_x < 0$. We can approximate the x-component of angular velocity using equation (5.3) and average over the fast oscillations:

$$\omega_x \approx -2p\omega_0 \log\left(1 + I(t)\right). \tag{5.5}$$

For either choice of sign(p), we see from equations (5.4) and (5.5) that when $I(t)$ decreases /increases, then $|\omega_x|$, and hence γ, decreases/increases. We denote the angle between the helix axis and the Z-axis (light direction) as χ. There are two possible ways for the cell to change the helix angle γ: either the cell changes its trajectory by rotating about its y-axis or the helix axis changes direction. However, since the flagella beat in the y-z plane, the cell cannot generate the required rotation about the y-axis. Therefore, the changes in γ are produced by a changes in direction of the helix axis, as shown in figure 5.4(a). Changes in the helix axis direction change the angle χ between the light direction and the helix axis.

Increasing and decreasing light produce opposite changes in γ, but since the cell sees increasing and decreasing light at different positions along the helix, the opposite changes in γ work together to produce the same directional change in χ. We denote $\varphi \in [0, 2\pi)$ as the phase of the cell on the helix where $\varphi = 0$ is the position furthest from the incoming light, marked with a red triangle in figure 5.4(c). When $\varphi \in (0, \pi)$, an increase/decrease in γ causes the helix axis to bend away from/towards the light

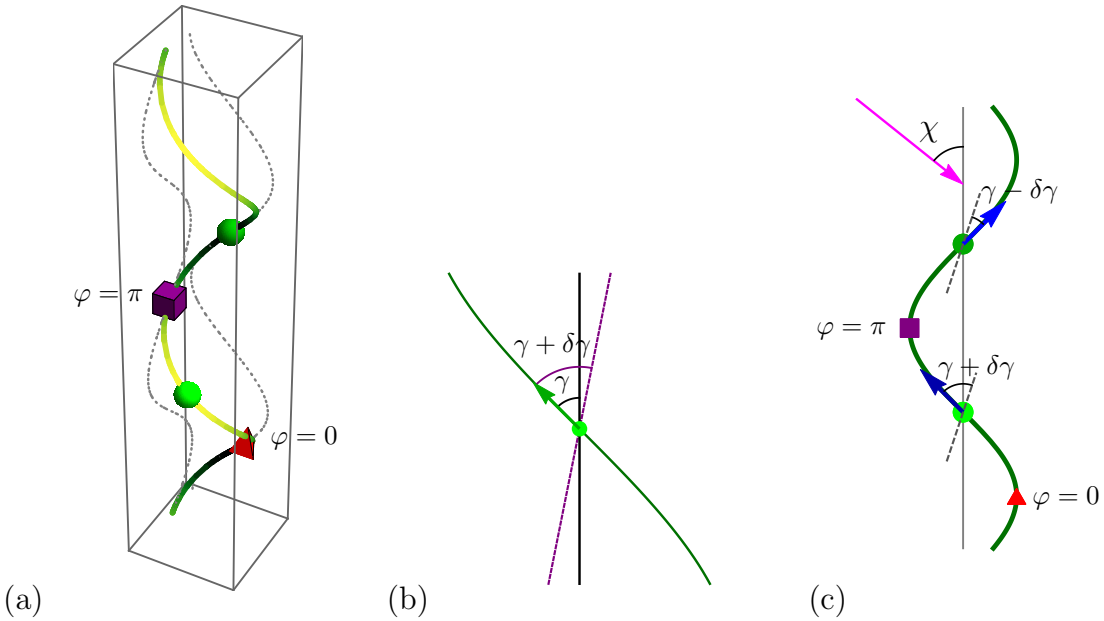


Figure 5.4: (a) Diagram of helix showing phases $\varphi = 0$ (red tetrahedron), when cell is on opposite side of helix from light, and $\varphi = \pi$ (purple cube), when cell is on same side of helix as light source. The green spheres show $\varphi = \pi/2, 3\pi/2$. (b) A change in γ occurs when the helix axis changes direction by $\delta\gamma$. The purple dashed line shows the new helix axis after the change in helix angle $\gamma \to \gamma + \delta\gamma$. (c) The change in χ due to a change in γ depends on the phase of the cell: $\delta\chi = \delta\gamma \sin\varphi$. The red triangle, purple square and green circles mark the positions $\varphi = 0$, $\varphi = \pi$ and $\varphi = \pi/2, 3\pi/2$, respectively, corresponding to the red tetrahedron, purple cube and green spheres shown in (a). When the cell has phase $\varphi \in (0, \pi)$, an increase/decrease in γ causes the helix axis to bend away from/towards the light; a corresponding decrease/increase in γ when $\varphi \in (\pi, 2\pi)$ also causes the helix axis to bend away from/towards the light. The pink arrow marks the incoming light and the blue arrows show the direction of the cell motion. The new directions of the helix axis if γ increases and decreases by $\delta\gamma$ at phases $\varphi = \pi/2$ and $\varphi = 3\pi/2$, respectively, are shown by the dashed lines.

and a decrease/increase in γ when $\varphi \in (\pi, 2\pi)$ also causes the helix axis to bend away from/towards the light.

We consider how the cell responds for each choice of sign(p). First let's consider $p > 0$, where $\omega_x < 0$ so the eyespot moves around the inside of the helix. As the cell moves from $\varphi = 0$ to $\varphi = \pi$, the eyespot goes from facing the light to being shaded by the cell body, so on average the cell sees a decrease in the light intensity and therefore γ decreases, causing the helix axis to bend towards the light. Similarly, as the cell moves from $\varphi = \pi$ to $\varphi = 2\pi$, the eyespot moves from being shaded by the cell body to facing the light again and on average the cell sees an increase in the light intensity so γ increases, also resulting in the helix axis bending towards the light. Therefore we have positive phototaxis for $p > 0$.

If $p < 0$, then $\omega_x > 0$ and the eyespot moves around the outside of the helix. When the cell moves from $\varphi = 0$ to $\varphi = \pi$ the eyespot moves from being shaded by the cell body to pointing towards the light, so the light intensity at the eyespot increases, γ increases, and the helix axis bends away from the light. When the cell moves from $\varphi = \pi$ to $\varphi = 2\pi$, the cell moves from an exposed to a shaded position so the light intensity decreases, γ decreases, and the helix axis bends away from the light. Therefore we have negative phototaxis for $p < 0$.

As we have shown, the direction of phototaxis is controlled by sign(p). If the coupling in equation (5.2) is linear (or another monotonically increasing form) instead of logarithmic then the phototaxis direction is the same for each choice of sign(p) by of the same mechanism as described above, provided the condition $|a_i| < 1$ is held.

The rate that the cell bends towards or away from the light depends on the coupling parameter $|p|$. The rate of bending is $\dot{\chi} = \dot{\gamma} \sin \varphi$, where

$$\dot{\gamma} \approx \frac{2|p|\omega_0 \dot{I}}{\Omega_z\big(1 + I(t)\big)}. \tag{5.6}$$

$\dot{I}$ changes sign at approximately the same time as $\sin \varphi$, so increasing $|p|$ increases the rate at which χ moves towards 0 or π. Equation (5.6) appears to suggest that increasing (decreasing) the spinning frequency, Ω_z, decreases (increases) the rate of steering, $\dot{\chi}$. However, increasing (decreasing) Ω_z also increases (decreases) the rate of change in light intensity seen by the eyespot, $\dot{I}$, linearly with Ω_z, so the effect of changing Ω_z is cancelled. We do not see significant variation of the steering rate with Ω_z in our numerical results if the spinning frequency, Ω_z, is at least an order of magnitude slower than the beat frequency Ω_b. We need to consider nonlinear terms in equation (5.6) if the spinning and beat frequencies become comparable, however

observations of *Chlamydomonas* show $\Omega_z \approx \Omega_\mathrm{b}/20$, so we do not need to consider this limit.

The direction of phototaxis is controlled by sign(p) in our model. *Chlamydomonas* usually steers towards light in low to moderate light intensities and steers away from light in high light intensity, so we suggest $p = 2H(I_\mathrm{b} + I_0 - I_c(\lambda_\mathrm{b}, \lambda_0)) - 1$ as a good choice for a basic model, where the critical light intensity $I_c(\lambda_\mathrm{b}, \lambda_0)$ depends on the wavelength of both isotropic background light and directional light.

5.4 Summary and discussion

Here, and in chapter 4, we have presented a simple model of *Chlamydomonas* that successfully meets our complex engineering needs of low Reynolds swimming, synchronised beating, run-and-tumble in darkness and phototaxis.

Simple coupling of the amplitude in the flagellar driving force to the intensity at the eyespot leads to positive and negative phototactic steering. The direction of phototaxis and the steering rate are controlled by the sign and magnitude, respectively, of the parameter p. As the cell rotates about its body axis, the light intensity viewed by the eyespot varies and produces different changes in the beat pattern of the two flagella, resulting in changes in the angular velocity. The cell swims along a helical trajectory and changes in the angular velocity causes the helix axis to bend. The position of the cell along the helix affects whether the helix axis bends towards or away from the light so opposite changes in light intensity that occur on opposite sides of the helix work together to bend the cell exclusively towards or away from the light.

Noise is included in the model to show that the steering mechanism is robust. The noise is not required for phototaxis, but it is essential for the run-and-tumble behaviour that is observed in the dark and discussed in section 4.4. The model includes a phase shift in the beat pattern between light and darkness and this gear change enables the cell to run-and-tumble in the dark and steer in the light effectively.

A prediction of our model is that in periodic light, if the period is shorter than the characteristic run duration, there are very few tumbles and the cell maintains its path towards or away from the light in the same way as it does with a constant light source, although the initial orienting time can be longer. It would be interesting to observe whether real *Chlamydomonas* cells phototax as effectively in periodic light as they do in constant light when the period is shorter than the typical run duration and longer than the period of rotation about the body axis. It would be interesting to observe the trajectories of individual cells, but an easier experiment which would

also test the effectiveness of periodic light is to observe a population of cells and compare how a population of cells move in periodic light compared to constant light. Rüffer and Nultsch observed free swimming cells in periodic light of 1 or 2 Hz, which is comparable to the frequency of cell body rotation [123]. They found that cells did not orient phototactically, but moved irregularly with forwards, backwards and circular movement. Our predication that cells can swim phototactically in periodic light is only valid when the period is several times longer than the rotation period of the cell and shorter than the mean run duration.

As discussed in chapter 4, the stability of the synchronised state is sensitive to the parameter a_0. We only get the desired behaviour of phototactic steering in the light and run-and-tumble in the dark for a narrow range of a_0. The phase dependence of the driving force is essential for the model to produce the different types of observed behaviour. Further development would be required to see if there is an increased range of a_0 that gives phototaxis and run-and-tumble if we include hydrodynamic interactions or flexibility in the bead trajectory. We have averaged over oscillation on the timescale of the flagellar beat and further work would also be required to see how the amplitude of fast oscillations affect the phototaxis behaviour and whether oscillations become important if the amplitude of oscillations is large.

We do not know of many experiments that have tracked individual phototaxing cells and we would like to see such experiments to compare with our model. We would like to know how sharply the cell steers so we can determine a realistic value of the parameter p, or find if different cells steer at different rates corresponding to a spread in values of p. We would like to see if any tumbles are observed when during phototaxis and see how the time between tumbles varies in different light intensities.

There are many factors that affect the direction of phototaxis including the intensity of the light source, pre-irradiation, concentration of cations, the wavelength of background monitoring light and photosynthesis [122, 123, 131–133]. Usually cells move towards the light at low and moderate intensities and away from the light at high intensities. We have suggested a basic model where the sign of p switches from positive to negative when the light intensity increases above a critical value. It would be interesting to see if there is a discrete change between positive and negative phototaxis or if there is a continuous change and cells have a decreasing value of p as the light intensity approaches a critical light intensity, if such a critical light intensity exists. However, such a study could be difficult because of the various other factors that affects the direction of phototaxis and the critical intensity (if it exists).

This work on phototaxis leads to the question: what about chemotaxis? Can we develop the model to understand chemotactic mechanisms? *Chlamydomonas* has different chemoresponses to different attractants [147], so more experimental results are needed before we can couple our model appropriately to the concentration field. Tracking experiments to show how *Chlamydomonas* cells move up a concentration gradient would help to identify whether *Chlamydomonas* uses run-and-tumble as a search mechanism or if it uses other strategies.

Chapter 6

Metachronal waves in arrays of cilia

We consider an array of independent cilia and study emergence of metachronal waves when the cilia are coupled by long range hydrodynamic interactions. Two-dimensional arrays of cilia are important for motility and for pumping fluid. Guirao and Joanny studied two-dimensional arrays and showed that metachronal waves emerge from the internal cilia mechanism and hydrodynamic interactions and that metachronism minimises the ATP threshold for beating [78]. They solve for a particular wavevector by requiring a stationary flow. They also show how randomly oriented cilia align through hydrodynamic interactions and how an array of symmetrically beating cilia spontaneously break the symmetry and creates flow. Elgeti and Gompper studied a model where cilia are modelled as beads driven around trajectories and coupled hydrodynamically. They solved the model numerically to show that metachronal waves emerge from random initial conditions through the hydrodynamic interactions [76]. Here, we also model cilia as beads driven around trajectories, but we use analytics so we can begin to understand how the waves emerge and why a particular wave vector is chosen.

Cilia have two parts of their stroke: the power stroke where the cilium is quite straight to increase the force against the fluid and the recovery stroke, where the cilium is more curved. In general the beat has a three-dimensional pattern and the 'beat direction' is in the direction of the power stroke. Metachronal waves that travel in the beat direction are known as symplectic waves, waves that travel opposite to the beat direction are known as antiplectic waves and waves that travel perpendicular to the beat direction are known as laoplectic waves.

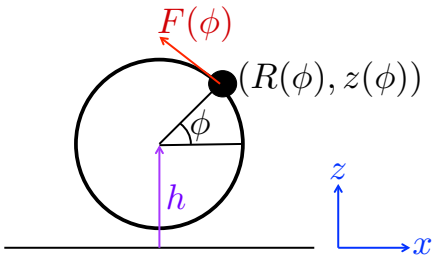


Figure 6.1: An individual rotor on a lattice point with trajectory $(R(\phi), z(\phi))$

6.1 The model

Each cilium is an independent rotor above a flat substrate on a lattice point, modelled as a bead moving around a trajectory. Here we consider a square lattice with lattice spacing d, with circular trajectories at an angle χ to the vertical and an angle θ with the lattice direction. All the cilia beat in the same direction in mature cells and it has been shown that hydrodynamic coupling can cause this alignment [78]. The position of bead i is $(r_i + R(\phi_i), h + z(\phi_i))$, where r_i is the lattice point, the centre of the orbit is height h above the substrate and $(R(\phi), z(\phi))$ describes the beat trajectory.

$$\begin{aligned} R(\phi) &= b(\cos\phi\cos\theta + \sin\chi\sin\phi\sin\theta, \cos\phi\sin\theta - \sin\chi\sin\phi\cos\theta) \\ z(\phi) &= b\cos\chi\sin\phi \end{aligned} \tag{6.1}$$

Each bead is driven by a phase dependent tangential driving force $F(\phi)$. The rotors are coupled by hydrodynamic interactions, which we approximate with the Blake tensor $\mathbf{G}$ [96, 97]. The phase velocity of each bead is

$$\dot{\phi}_i = \frac{F(\phi_i)}{\xi|R'(\phi)|} + \frac{1}{8\pi\eta|R'(\phi)|}\sum_j \hat{\mathbf{t}}(\phi_i)\cdot\mathbf{G}(r_i+R_i, h+z_i, r_j+R_j, h+z_j)\cdot\hat{\mathbf{t}}(\phi_j)F(\phi_j), \tag{6.2}$$

where $\xi = 6\pi\eta a$, we have denoted $R_i = R(\phi_i), z_i = z(\phi_i)$, $R'(\phi) = \frac{\partial R}{\partial \phi}$ and

$$\hat{\mathbf{t}}(\phi) = \begin{pmatrix} -\sin\phi\cos\theta + \sin\chi\cos\phi\sin\theta \\ -\sin\phi\sin\theta - \sin\chi\cos\phi\cos\theta \\ \cos\chi\cos\phi \end{pmatrix} \tag{6.3}$$

is the tangent of the trajectory. We consider $b << d$ and $h \sim d$.

6.1.1 The Blake tensor

Consider a surface at $z = 0$ with a point force acting at $Y_\mathrm{f} = (Y_1, Y_2, H')$, which has an image at $Y_\mathrm{im}(Y_1, Y_2, -H')$ due to the surface. We use the Blake tensor to calculate

the velocity of the fluid at point $y = (y_1, y_2, H)$. Let $x = y - Y_{\rm f}$ and $X = y - Y_{\rm im}$. The Blake tensor is given by

$$\begin{aligned}\mathbf{G}_{ij}(y, Y_{\rm f}) &= \tfrac{\delta_{ij}}{x} + \tfrac{x_i x_j}{x^3} - \left(\tfrac{\delta_{ij}}{X} + \tfrac{X_i X_j}{X^3}\right) \\ &+2H'(\delta_{j\alpha}\delta_{\alpha k} - \delta_{j3}\delta_{3k})\tfrac{\partial}{\partial X_k}\left[\tfrac{H'X_i}{X^3} - \left(\tfrac{\delta_{i3}}{X} + \quad \frac{X_i X_3}{X^3}\right)\right] \quad \alpha = 1, 2 \end{aligned} \tag{6.4}$$

Let $r = (y_1, y_2)$ and $r' = (Y_1, Y_2)$. Taking the Fourier transform of the components of $\mathbf{G}$, we have the following, with $\alpha, \beta = 1, 2$:

$$\begin{aligned}\mathbf{G}_{\alpha\beta} &= 2\pi \int \frac{d^2q}{(2\pi)^2}\frac{e^{{\rm i}q.(r-r')}}{|q|}\big[\delta_{\alpha\beta}(e^{-|q||H-H'|} - e^{-|q|(H+H')}) \\ &\quad -2HH'q_\alpha q_\beta e^{-|q|(H+H')}\big] \end{aligned} \tag{6.5}$$

$$\begin{aligned}\mathbf{G}_{3\alpha} &= 2\pi{\rm i} \int \frac{d^2q}{(2\pi)^2}\frac{e^{{\rm i}q.(r-r')}}{|q|}q_\alpha\big[(H-H')(e^{-|q|(H+H')} - e^{-|q||H-H'|}) \\ &\quad -2HH'|q|e^{-|q|(H+H')}\big] \end{aligned} \tag{6.6}$$

$$\begin{aligned}\mathbf{G}_{\alpha 3} &= 2\pi{\rm i} \int \frac{d^2q}{(2\pi)^2}\frac{e^{{\rm i}q.(r-r')}}{|q|}q_\alpha\big[(H-H')(e^{-|q|(H+H')} - e^{-|q||H-H'|}) \\ &\quad +2HH'|q|e^{-|q|(H+H')}\big] \end{aligned} \tag{6.7}$$

$$\begin{aligned}\mathbf{G}_{33} &= 2\pi \int \frac{d^2q}{(2\pi)^2}\frac{e^{{\rm i}q.(r-r')}}{|q|}\big[e^{-|q||H-H'|} - e^{|q|(H+H')} + |q||H-H'|e^{-|q||H-H'|} \\ &\quad -|q|(H+H')e^{-|q|(H+H')} - 2HH'q^2e^{|q|(H+H')}\big] \end{aligned} \tag{6.8}$$

Inserting these into equation (6.2) and expanding to first order in the trajectory we have the phase velocity

$$\begin{aligned}
\dot{\phi} \;=\; & \frac{F(\phi_i)}{\xi|R'(\phi)|} + \sum_{r'} \frac{F(\phi')}{8\pi\eta|R'(\phi')|}\Bigg(t_\alpha t'_\beta 2\pi \int \frac{d^2q}{(2\pi)^2}\frac{e^{\mathrm{i}q.(r-r')}}{|q|}\Big[\delta_{\alpha\beta}(1-e^{-2h|q|}) \\
& -2h^2 q_\alpha q_\beta e^{-2h|q|} + \delta_{\alpha\beta}(-|q||z-z'| - |q|(z+z')e^{-2h|q|}) \\
& -2h(z+z')q_\alpha q_\beta e^{-2h|q|}(1-h|q|) + \mathrm{i}q.(R-R')\big(\delta_{\alpha\beta}(1-e^{-2h|q|}) \\
& -2h^2 q_\alpha q_\beta e^{-2h|q|}\big)\Big] + t_3 t'_\alpha 2\pi\mathrm{i}\int \frac{d^2q}{(2\pi)^2}\frac{e^{\mathrm{i}q.(r-r')}}{|q|}q_\alpha\Big[\\
& -2h^2|q|e^{-2h|q|} + (z-z')(e^{-2h|q|}-1) \\
& -2h|q|(z+z')e^{-2h|q|}(1-h|q|) - \mathrm{i}q.(R-R')2h^2|q|e^{-2h|q|}\Big] \\
& + t_\alpha t'_3 2\pi\mathrm{i}\int \frac{d^2q}{(2\pi)^2}\frac{e^{\mathrm{i}q.(r-r')}}{|q|}q_\alpha\Big[2h^2|q|e^{-2h|q|} + (z-z')(e^{-2h|q|}-1) \\
& +2h|q|(z+z')e^{-2h|q|}(1-h|q|) + \mathrm{i}q.(R-R')2h^2|q|e^{-2h|q|}\Big] \\
& + t_3 t'_3 2\pi\int \frac{d^2q}{(2\pi)^2}\frac{e^{\mathrm{i}q.(r-r')}}{|q|}\Big[1 - e^{-2|q|h} - 2h|q| \\
& \cdot(1+h|q|)e^{-2h|q|} + 2h^2q^3(z+z')e^{-2h|q|} \\
& + \mathrm{i}q.(R-R')\big(1-e^{-2h|q|} - 2h|q|(1+h|q|)e^{-2h|q|}\big)\Big]\Bigg). \qquad (6.9)
\end{aligned}$$

Let

$$\begin{aligned}
f_1 &= \cos\theta \qquad & g_1 &= \sin\chi\sin\theta \\
f_2 &= \sin\theta \qquad & g_2 &= -\sin\chi\cos\theta \\
f_3 &= \cos\chi. & & \qquad (6.10)
\end{aligned}$$

Then we can write

$$\begin{aligned}
R_\alpha &= b(f_\alpha\cos\phi + g_\alpha\sin\phi), \qquad & z &= bf_3\sin\phi, \\
t_\alpha &= -f_\alpha\sin\phi + g_\alpha\cos\phi, \qquad & t_3 &= f_3\cos\phi.
\end{aligned}$$

The expression in equation (6.9) using this notation is shown in equation (B.1) in appendix B, where near field terms are highlighted in blue. In the following analysis we only consider the far field terms.

6.2 Constant velocity gauge

We move into a gauge Φ where the intrinsic velocity is constant,

$$\frac{d\Phi_{\text{intrinsic}}}{dt} = \frac{F(\phi_i)}{\xi|R'(\phi)|} = \Omega,$$

where the constant Ω is chosen such that ϕ and Φ have the same periodicity. This gives the relation between ϕ and Φ

$$\frac{d\Phi}{d\phi} = \frac{\Omega b\xi}{F(\phi)}. \tag{6.11}$$

The periodic driving force is

$$F(\phi) = F_0\big(1 + \sum_n (A_n \cos n\phi + B_n \sin n\phi)\big), \tag{6.12}$$

so integrating equation (6.11) and approximating to first order in A_n, B_n, we have the relation

$$\phi(\Phi) = \Phi + \sum_n \big(\frac{A_n}{n}\sin n\Phi - \frac{B_n}{n}\cos n\Phi\big), \tag{6.13}$$

where we have set $\Omega = F_0/(b\xi)$ for the correct periodicity. The time evolution equation for Φ is

$$\dot{\Phi} = \frac{F_0}{F(\phi)}\dot{\phi}(\Phi), \tag{6.14}$$

where $\dot{\phi}(\Phi)$ is obtained by substituting equation (6.13) into equation (B.1).

We consider the variables $\varphi = \Phi + \Phi'$ (fast) and $\Delta = \Phi - \Phi'$ (slow), so that $\Phi = (\varphi + \Delta)/2$ and $\Phi = (\varphi - \Delta)/2$. Averaging over the fast variable φ, we have the following expression for Φ to first order in b, A_n, B_n.

$$\begin{aligned}
\dot{\Phi} \;=\; & \frac{F_0}{\xi b} + \frac{F_0}{4\eta b}\sum_{r'}\int \frac{d^2q}{(2\pi)^2} e^{\mathrm{i}q.(r-r')}\Big\{\frac{1}{|q|}\big(\delta_{\alpha\beta}(1-e^{-2h|q|}) - 2h^2 q_\alpha q_\beta e^{-2h|q|}\big) \\
& \cdot\Big[f_\alpha f_\beta\Big(\cos\Delta(\frac{1}{2}+\frac{A_2}{4}) + \frac{B_2}{2}\sin\Delta\Big) + g_\alpha g_\beta\Big(\frac{1}{2}\cos\Delta(1-\frac{A_2}{2}) - \frac{B_2}{2}\sin\Delta\Big) \\
& - f_\alpha g_\beta\Big(\frac{1}{2}(\sin\Delta - \frac{B_2}{2}\cos\Delta) + \frac{A_2}{2}\sin\Delta\Big) - g_\alpha f_\beta\Big(\frac{1}{2}(-\sin\Delta - \frac{B_2}{2}\cos\Delta) \\
& + \frac{A_2}{2}\sin\Delta\Big)\Big] - \mathrm{i}q_\alpha 2h^2 e^{-2h|q|}\Big[-f_3 f_\alpha\Big(-\frac{1}{2}(\frac{B_2}{2}\cos\Delta + \sin\Delta) + \frac{A_2}{2}\sin\Delta\Big) \\
& + f_3 g_\alpha\Big(\cos\Delta(\frac{1}{2}-\frac{A_2}{4}) - \frac{B_2}{2}\sin\Delta\Big)\Big] + \mathrm{i}q_\alpha 2h^2 e^{-2h|q|}\Big[-f_\alpha f_3\Big(\frac{1}{2}(-\frac{B_2}{2}\cos\Delta \\
& + \sin\Delta) + \frac{A_2}{2}\sin\Delta\Big) + g_\alpha f_3\Big(\cos\Delta(\frac{1}{2}-\frac{A_2}{4}) - \frac{B_2}{2}\sin\Delta\Big)\Big] + f_3^2\Big(\frac{1-e^{-2h|q|}}{|q|} \\
& - 2h(1+h|q|)e^{-2h|q|}\Big)\Big[\cos\Delta(\frac{1}{2}-\frac{A_2}{4}) - \frac{B_2}{2}\sin\Delta\Big] \\
& + \text{near field terms}\Big\}
\end{aligned} \tag{6.15}$$

We look for solutions that are plane waves with perturbations:

$$\Phi \;= \omega t - k.r + \delta\Phi \tag{6.16a}$$

$$\Rightarrow\quad \dot{\Phi} \;= \omega + \partial_t\delta\Phi, \tag{6.16b}$$

so

$$\Delta = -k.(r - r') + (\delta\Phi - \delta\Phi') \tag{6.17}$$

We insert equation (6.17) into (6.15) and expand to linear order in $\delta\Phi - \delta\Phi'$. The expression is shown in equation (B.2) in appendix B. Comparing terms in equation (B.2) with equation (6.16b), the terms independent of the perturbation $(\delta\Phi - \delta\Phi')$ give the dispersion relation $\omega(k)$, and the linear terms in $(\delta\Phi - \delta\Phi)$ give the time evolution of the perturbation.

6.3 The dispersion relation

We get the dispersion relation from the terms in equation (B.2) that are independent of the perturbation $(\delta\Phi - \delta\Phi')$. The terms are given in equation (B.3) in appendix B. We sum over lattice sites r' using

$$\sum_r e^{\mathrm{i}q.r} = \frac{(2\pi)^2}{d^2} \sum_G \delta^2(q + G) \tag{6.18}$$

where we sum over Brillouin zones $G = \frac{2\pi}{d}(m\hat{x} + n\hat{y}), \quad m, n \in \mathbb{Z}$. We can then integrate using the delta functions

$$\int d^2q f(q)\delta(q \mp k + G) = f(\pm k - G).$$

Summing over r' and integrating over q in equation (B.3) gives the dispersion relation:

$$\begin{aligned}
\omega \;=\; & \frac{F_0}{\xi b} + \frac{F_0}{4\eta b d^2} \sum_G \Bigg\{ \frac{1}{|k+G|} \Big(\delta_{\alpha\beta}(1 - e^{-2h|k+G|}) \\
& - 2h^2(k_\alpha + G_\alpha)(k_\beta + G_\beta) e^{-2h|k+G|} \Big) \Big[f_\alpha f_\beta \Big(\frac{1}{4}(1 + \frac{A_2}{2}) - \frac{B_2}{4\mathrm{i}} \Big) \\
& + g_\alpha g_\beta \Big(\frac{1}{4}(1 - \frac{A_2}{2}) + \frac{B_2}{4\mathrm{i}} \Big) + f_\alpha g_\beta \Big(\frac{1 + A_2}{4\mathrm{i}} + \frac{B_2}{8} \Big) + g_\alpha f_\beta \Big(\frac{-1 + A_2}{4\mathrm{i}} + \frac{B_2}{8} \Big) \Big] \\
& + \frac{1}{|k-G|} \Big(\delta_{\alpha\beta}(1 - e^{-2h|k-G|}) - 2h^2(k_\alpha - G_\alpha)(k_\beta - G_\beta) e^{-2h|k-G|} \Big) \\
& \cdot \Big[f_\alpha f_\beta \Big(\frac{1}{4}(1 + \frac{A_2}{2}) + \frac{B_2}{4\mathrm{i}} \Big) + g_\alpha g_\beta \Big(\frac{1}{4}(1 - \frac{A_2}{2}) - \frac{B_2}{4\mathrm{i}} \Big) + f_\alpha g_\beta \Big(-\frac{1 + A_2}{4\mathrm{i}} \\
& + \frac{B_2}{8} \Big) + g_\alpha f_\beta \Big(-\frac{-1 + A_2}{4\mathrm{i}} + \frac{B_2}{8} \Big) \Big] - (k_\alpha + G_\alpha) h^2 e^{-2h|k+G|} f_3 f_\alpha \\
& - (k_\alpha - G_\alpha) h^2 e^{-2h|k-G|} f_3 f_\alpha + \Big(\frac{1 - e^{-2h|k+G|}}{|k+G|} - 2h(1 + h|k+G|) e^{-2h|k+G|} \Big) \\
& \cdot f_3^2 \Big(\frac{1}{4}(1 - \frac{A_2}{2}) + \frac{B_2}{4\mathrm{i}} \Big) + \Big(\frac{1 - e^{-2h|k-G|}}{|k-G|} - 2h(1 + h|k-G|) e^{-2h|k-G|} \Big) \\
& \cdot f_3^2 \Big(\frac{1}{4}(1 - \frac{A_2}{2}) - \frac{B_2}{4\mathrm{i}} \Big) \Bigg\},
\end{aligned} \tag{6.19}$$

where terms in red cancel due to symmetry.

The dominant term in equation (6.19) is

$$\begin{aligned}\omega &= \frac{F_0}{\xi b}+\frac{F_0}{4\eta b d^2}\sum_G\Bigg\{\frac{1}{|k+G|}\delta_{\alpha\beta}\Big[f_\alpha f_\beta\Big(\frac{1}{4}(1+\frac{A_2}{2})\Big)+g_\alpha g_\beta\Big(\frac{1}{4}(1-\frac{A_2}{2})\Big)\\ &+f_\alpha g_\beta\frac{B_2}{8}+g_\alpha f_\beta\frac{B_2}{8}\Big]+\frac{1}{|k-G|}\delta_{\alpha\beta}\Big[f_\alpha f_\beta\Big(\frac{1}{4}(1+\frac{A_2}{2})\Big)\\ &+g_\alpha g_\beta\Big(\frac{1}{4}(1-\frac{A_2}{2})\Big)+f_\alpha g_\beta\frac{B_2}{8}+g_\alpha f_\beta\frac{B_2}{8}\Big]+\frac{1}{|k+G|}f_3^2\Big(\frac{1}{4}(1-\frac{A_2}{2})\Big)\\ &+\frac{1}{|k-G|}f_3^2\Big(\frac{1}{4}(1-\frac{A_2}{2})\Big)\Bigg\},\end{aligned} \tag{6.20}$$

Using

$$f_1^2+g_1^2+f_2^2+g_2^2+f_3^2=2, \tag{6.21a}$$

$$f_1^2-g_1^2+f_2^2-g_2^2-f_3^2=0, \tag{6.21b}$$

$$f_1g_1+f_2g_2=0, \tag{6.21c}$$

which follow from definitions (6.10), we have

$$\omega=\frac{F_0}{\xi b}+\frac{F_0}{4\eta b d^2}\sum_G\left(\frac{1}{2|k+G|}+\frac{1}{2|k-G|}\right). \tag{6.22}$$

The sum diverges with system size mn. We split ω into k-independent and k-dependent parts:

$$\omega=\omega_0+\omega_k(k), \tag{6.23}$$

where

$$\omega_0=\frac{F_0}{\xi b}+\frac{F_0}{4\eta b d^2}\sum_{G\neq 0}\frac{1}{|G|}, \tag{6.24}$$

which diverges with system size, and

$$\omega_k(k)=\frac{F_0}{4\eta b d^2}\left[\sum_{G\neq 0}\Big(\frac{1}{2|k+G|}+\frac{1}{2|k-G|}-\frac{1}{|G|}\Big)+\frac{1}{|k|}\right]. \tag{6.25}$$

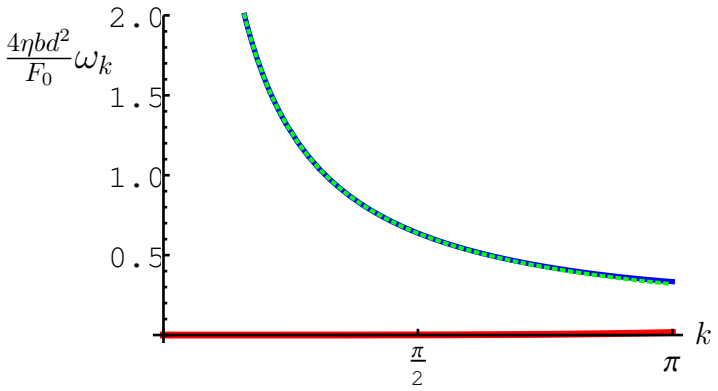


Figure 6.2: k-dependent part of the dispersion relation. Blue: $\omega_k(k)$; red: $\omega_k(k) - 1/|k|$; dotted green: $1/|k|$.

We consider the term ω_k.

$$\begin{aligned}
\sum_{G\neq 0}\left(\frac{1}{|k\pm G|}-\frac{1}{|G|}\right) &= \sum_{G\neq 0}\frac{|G|-\sqrt{k^2+G^2\pm 2k\cdot G}}{|G||k\pm G|} \\
&= \sum_{G\neq 0}\frac{|G|-|G|\sqrt{1+k^2/G^2\pm 2k\cdot G/G^2}}{|G||k\pm G|} \\
&\approx \sum_{G\neq 0}\frac{|G|-|G|(1+k^2/(2G^2)\pm k\cdot G/G^2)}{|G||k\pm G|} \\
&= \sum_{G\neq 0}\frac{-k^2/(2|G|)\mp k\cdot G/|G|}{|G||k\pm G|}
\end{aligned}$$

Note that the term $\sum_G k\cdot G/|k+G|$ is actually an even function in k, because of the sum over G; this term is negligible except for $|m|,|n|\leq 1$. By symmetry both the $+k$ and $-k$ terms give the same contribution, so we have

$$\omega_k(k)=\frac{F_0}{4\eta bd^2}\left(\sum_{G\neq 0}\frac{-k^2/2\mp k\cdot G}{G^2|k\pm G|}+\frac{1}{|k|}\right). \tag{6.26}$$

Figure 6.2 shows the k-dependent part of the dispersion relation. We see that the $1/|k|$ term dominates and the frequency decreases with increasing k. In the limit $k\to 0$, (infinite wavelength corresponding to all rotors beating with the same phase) the frequency diverges, however, in section 6.4 we find that small values of $|k|$ are unstable, so the system cannot evolve to this limit. This singularity arises because when all the rotors beat with the same phase, they all exert a force on the fluid in the same direction at the same time. In the low Reynolds number regime, the velocity of a fluid element in response to a Stokeslet is long range and instantaneous. If we sum

over an infinite lattice, then the long range nature of hydrodynamic interactions means there is an infinite number of Stokeslets instantaneously giving velocity to the fluid at a particular rotor so the phase velocity diverges. The low Reynolds approximation is not valid for infinite wavelengths.

6.4 Stability of the wave

The perturbative part of the equation has form

$$\begin{aligned} \partial_t \delta\Phi(r) &= \sum_{r'} (\delta\Phi - \delta\Phi') c(r - r') \\ \Rightarrow \partial_t \delta\tilde{\Phi}(q') &= \big(\tilde{c}(0) - \tilde{c}(q')\big)\delta\tilde{\Phi}(q') \end{aligned} \tag{6.27}$$

where $\tilde{c}(q') = \sum_{r'} e^{-\mathrm{i}q'.r'}$. For a stable wave we require $\Re[\tilde{c}(0) - \tilde{c}(q')] < 0$. The terms in $c(r - r')$ are shown in equation (B.2). We give the expression for the Fourier transform, $\tilde{c}(q')$, in equation (B.4) in appendix B. Performing the integration over q

in equation (B.4) gives

$$\begin{aligned}
\tilde{c}(q') &= \frac{F_0}{4\eta b d^2}\sum_G \Bigg\{ \frac{1}{|q'-k-G|}\Big(\delta_{\alpha\beta}(1-e^{-2h|q'-k-G|}) - 2h^2(q'_\alpha - k_\alpha - G_\alpha) \\
&\cdot(q'_\beta - k_\beta - G_\beta)e^{-2h|q'-k-G|}\Big)\Bigg[f_\alpha f_\beta\Big(\frac{1}{4\mathrm{i}}(1+\frac{A_2}{2}) + \frac{B_2}{4}\Big) \\
&+ g_\alpha g_\beta\Big(\frac{1}{4\mathrm{i}}(1-\frac{A_2}{2}) - \frac{B_2}{4}\Big) - f_\alpha g_\beta\Big(\frac{1}{4}(1+A_2) - \frac{B_2}{8\mathrm{i}}\Big) \\
&- g_\alpha f_\beta\Big(\frac{1}{4}(-1+A_2) - \frac{B_2}{8\mathrm{i}}\Big)\Bigg] + \frac{1}{|q'+k-G|}\Big(\delta_{\alpha\beta}(1-e^{-2h|q'+k-G|}) \\
&-2h^2(q'_\alpha + k_\alpha - G_\alpha)(q'_\beta + k_\beta - G_\beta)e^{-2h|q'+k-G|}\Big)\Bigg[f_\alpha f_\beta\Big(-\frac{1}{4\mathrm{i}}(1+\frac{A_2}{2}) \\
&+\frac{B_2}{4}\Big) + g_\alpha g_\beta\Big(-\frac{1}{4\mathrm{i}}(1-\frac{A_2}{2}) - \frac{B_2}{4}\Big) - f_\alpha g_\beta\Big(\frac{1}{4}(1+A_2) + \frac{B_2}{8\mathrm{i}}\Big) \\
&- g_\alpha f_\beta\Big(\frac{1}{4}(-1+A_2) + \frac{B_2}{8\mathrm{i}}\Big)\Bigg] - \mathrm{i}(q'_\alpha - k_\alpha - G_\alpha)4h^2 e^{-2h|q'-k-G|}\frac{f_3 f_\alpha}{4} \\
&-\mathrm{i}(q'_\alpha + k_\alpha - G_\alpha)4h^2 e^{-2h|q'+k-G|}\frac{f_3 f_\alpha}{4} + f_3^2\Big(\frac{1-e^{-2h|q'-k-G|}}{|q'-k-G|} \\
&-2h(1+h|q'-k-G|)e^{-2h|q'-k-G|}\Big)\Big(\frac{1}{4\mathrm{i}}(1-\frac{A_2}{2}) - \frac{B_2}{4}\Big) \\
&+f_3^2\Big(\frac{1-e^{-2h|q'+k-G|}}{|q'+k-G|} - 2h(1+h|q'+k-G|)e^{-2h|q'+k-G|}\Big) \\
&\cdot\Big(-\frac{1}{4\mathrm{i}}(1-\frac{A_2}{2}) - \frac{B_2}{4}\Big)\Bigg\}. \qquad (6.28)
\end{aligned}$$

We look for solutions where $\Re[\tilde{c}(0) - \tilde{c}(q')] < 0 \quad \forall q'$. Figure 6.3 shows density plots with the zero contour for $\Re[\tilde{c}(0) - \tilde{c}(q')] < 0$ over $q \in BZ_1$ for different wavevectors. We use parameters $k_\parallel$ and $k_\perp$ to define the components of the wavevector parallel and perpendicular to the beat direction:

$$\begin{aligned}
k &= k_\parallel(f_1\hat{x} + f_2\hat{y}) + k_\perp(-f_2\hat{x} + f_1\hat{y}) \qquad (6.29)\\
|k| &= \sqrt{k_\parallel^2 + k_\perp^2}
\end{aligned}$$

We note that in the far field limit there is $k \to -k$ symmetry. We require that $\Re[\tilde{c}(0) - \tilde{c}(q')]$ has the same sign for all q' (if all values are positive then we can reverse the sign by changing $A_2 \to -A_2$ and $B_2 \to -B_2$). We find that for symplectic and antiplectic waves, we get a stable solution for sufficiently large k, but smaller values of $|k|$ are unstable, as shown in figure 6.3(a - c). When $|k| = 1.5$, wave directions

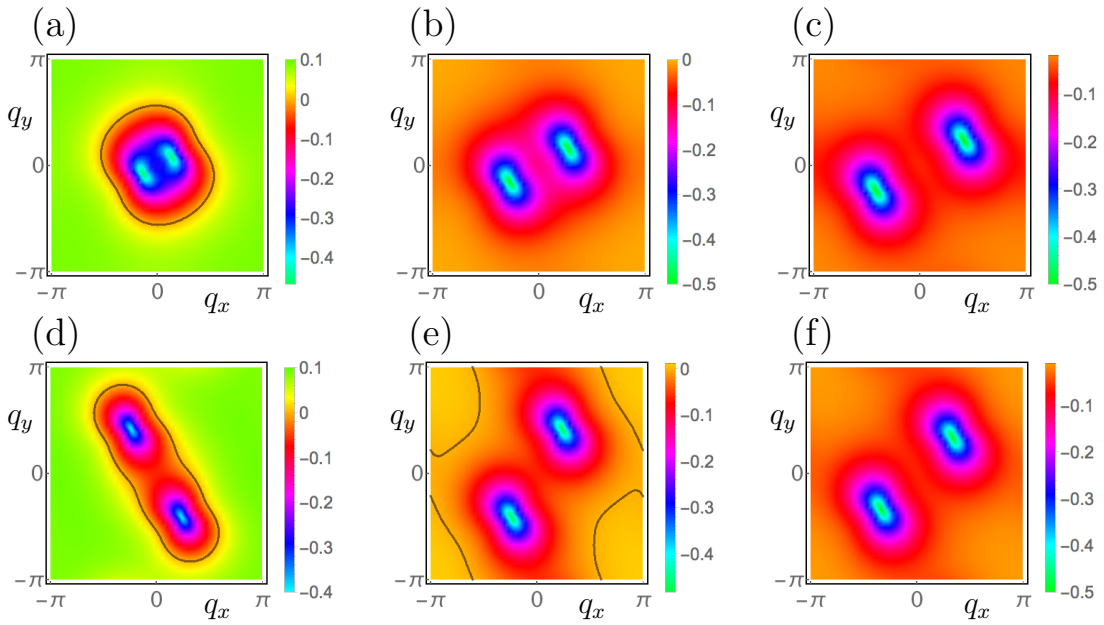


Figure 6.3: Density plots of $\Re[\tilde{c}(0) - \tilde{c}(q')]$ showing zero contour (black line) for (a - c) symplectic waves with different $|k|$. (d) - (g) Different wave directions with $|k| = 1.5$. Parameters used are $\chi = \pi/4$, $\theta = \pi/6$, $B_2 = 1$ and $A_2 = 0$, $k_\perp = 0$ and (a) $k_\parallel = 0.5$, (b) $k_\parallel = 1$, (c) $k_\parallel = 1.5$. Larger values of k give stable solutions, so we fix $|k| = 1.5$ and vary the direction with a parameter ν, where $k_\parallel = |k| \cos \nu$ and $k_\perp = |k| \sin \nu$. We show directions (d) $\nu = \pi/2$ (laoplectic), (e) $\nu = \pi/6$, (f) $\nu = \pi/12$. If $\text{sign}(\Re[\tilde{c}(0) - \tilde{c}(q')]) = -1 \quad \forall q'$ then the wave vector is stable, so the plots that do not have a zero contour have stable wavevectors.

that are close to symplectic or antiplectic, $k_\parallel << k_\perp$, are stable, but if $k_\perp \gtrsim k_\parallel$ then the perturbation becomes unstable, as shown in figure 6.3(d - f). We tried other values of A_2 and χ and found the same results: stable solutions for symplectic or antiplectic waves with sufficiently large $|k|$, but these parameters affect the minimum value of $|k|$ that will give stability and the maximum directional deviation away from a sym(anti)plectic wave that gives stability.

6.4.1 Looking for stability analytically

From looking at equation (6.28), it is not immediately obvious what choice of k gives stability. We require $\Re[\tilde{c}(0) - \tilde{c}(q')] < 0 \quad \forall q'$. First we look for k that satisfy the stability requirement for large q'. We then need to check if these solutions are also stable for small k. For large q', the $\tilde{c}(0)$ term dominates so we look for k such that $\Re[\tilde{c}(0)] < 0$, where

$$\begin{aligned}
\Re[\tilde{c}(0)] \;=\; & \frac{F_0}{4\eta b d^2}\sum_G \Bigg\{ \frac{1}{|k+G|}\Big(\delta_{\alpha\beta}(1-e^{-2h|k+G|}) \\
& -2h^2(k_\alpha+G_\alpha)(k_\beta+G_\beta)e^{-2h|k+G|}\Big)\Bigg[f_\alpha f_\beta\frac{B_2}{4} - g_\alpha g_\beta\frac{B_2}{4} \\
& -\frac{f_\alpha g_\beta}{4}(1+A_2) - \frac{g_\alpha f_\beta}{4}(-1+A_2)\Bigg] + \frac{1}{|k-G|}\Big(\delta_{\alpha\beta}(1-e^{-2h|k-G|}) \\
& -2h^2(k_\alpha-G_\alpha)(k_\beta-G_\beta)e^{-2h|k-G|}\Big)\Bigg[f_\alpha f_\beta\frac{B_2}{4} \\
& -g_\alpha g_\beta\frac{B_2}{4} - \frac{f_\alpha g_\beta}{4}(1+A_2) - \frac{g_\alpha f_\beta}{4}(-1+A_2)\Bigg] \\
& -f_3^2\Big(\frac{1-e^{-2h|k+G|}}{|k+G|} - 2h(1+h|k+G|)e^{-2h|k+G|}\Big)\frac{B_2}{4} \\
& -f_3^2\Big(\frac{1-e^{-2h|k-G|}}{|k-G|} - 2h(1+h|k-G|)e^{-2h|k-G|}\Big)\frac{B_2}{4}\Bigg\}, \qquad (6.30)
\end{aligned}$$

and terms in red cancel by symmetry and by identities (6.21b) and (6.21c). Let $f = f_1\hat{x} + f_2\hat{y}$ and $g = g_1\hat{x} + g_2\hat{y}$. Then by symmetry of the sum we can write (6.30)

as

$$\begin{aligned}\Re[\tilde{c}(0)] &= \frac{F_0}{4\eta b d^2}\sum_G \frac{e^{-2h|k+G|}}{|k+G|}\Big\{ -B_2h^2\Big((f\cdot k)^2-(g\cdot k)^2 \\ &\quad +2(f\cdot k)(g\cdot G)-2(g\cdot k)(f\cdot G)+(f\cdot G)^2-(g\cdot G)^2\Big) \\ &\quad +2A_2h^2\Big((f\cdot k)(g\cdot k)+2(f\cdot k)(g\cdot G)+2(f\cdot G)(g\cdot k)+(f\cdot G)(g\cdot G)\Big) \\ &\quad +f_3^2B_2h|k+G|\big(1+h|k+G|\big)\Big\}. \end{aligned} \tag{6.31}$$

Writing k in the form of equation (6.29), we have

$$\begin{aligned}\Re[\tilde{c}(0)] &= \frac{F_0}{4\eta b d^2}\sum_G \frac{e^{-2h|k+G|}}{|k+G|}h^2\Big\{ \\ &\quad -B_2\Big(k_\parallel^2-k_\perp^2\sin^2\chi+2k_\parallel(g\cdot G)+2k_\perp\sin\chi(f\cdot G)+(f\cdot G)^2-(g\cdot G)^2\Big) \\ &\quad +2A_2\Big(-k_\parallel k_\perp\sin\chi+2k_\parallel(g\cdot G)-2(f\cdot G)k_\perp\sin\chi+(f\cdot G)(g\cdot G)\Big) \\ &\quad +f_3^2B_2\frac{|k+G|}{h}\big(1+h|k+G|\big)\Big\}. \end{aligned} \tag{6.32}$$

Let us consider how each term contributes. When we sum over G, the dominant terms are the $m,n=0,\pm1$ terms; larger G terms are negligible. In the second line of equation (6.32), if we choose $B_2>0$ then this line gives a negative contribution to $\Re[\tilde{c}(0)]$ if the terms in the brackets add up to a positive number. This is the case if $k_\parallel^2-k_\perp^2\sin^2\chi$ is sufficiently large to overcome negative contributions from the terms in G (terms in G remain small because the contributions from different directions partially cancel). This shows that symplectic (in direction of beat) or antiplectic (opposite direction of beat) waves give stable solutions when $|k|$ is sufficiently large, but if $|k|$ is small then other terms can cause $\Re[\tilde{c}(0)]$ to become positive. We find numerically that for small q' the contribution from $c(q')$ does not affect the stability when $k_\parallel^2-k_\perp^2\sin^2\chi >> 0$. Another choice we consider is to let $B_2<0$ and $k_\parallel^2-k_\perp^2\sin^2\chi << 0$, which is a laoplectic wave with $|k|$ and χ sufficiently large. This gives $\Re[\tilde{c}(0)]<0$, however, we find that for small q' the contribution from $c(q')$ gives positive regions of $\Re[\tilde{c}(0)-\tilde{c}(q')]$.

Figure 6.4 shows the stable regions of k for parameters $A_2=0, B_2=\pm1, \chi=\pi/4, \theta=\pi/6$. This shows that there are no stable waves for $|k|\lesssim 1$, so we must have a wavelength $\lesssim 2\pi/d$. We also see that wave direction ν needs to be close to 0 or π, where $k_\parallel=|k|\cos\nu$ and $k_\perp=|k|\sin\nu$. We do not get close to the divergence in the

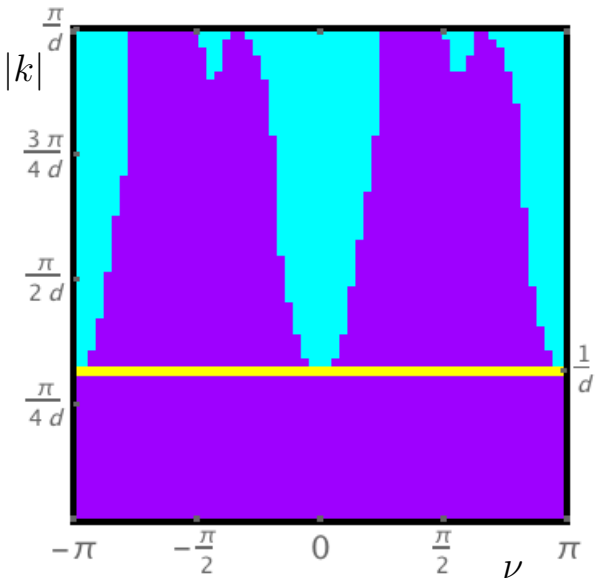


Figure 6.4: Stable and unstable wavevectors using parameters $A_2 = 0, B_2 = \pm 1, \chi = \pi/4, \theta = \pi/6$. Stable regions of k are shown in light blue, unstable regions of k in purple. Horizontal axis: direction of wavevector ν, where $k_\parallel = |k| \cos \nu$ and $k_\perp = |k| \sin \nu$; vertical axis: size of wavevector $|k|$. The yellow line shows the minimum value of $|k|$ required for stability.

dispersion relation (6.26) since small wavenumbers are unstable. We also note that wavelengths must be longer than the cilia spacing, d, so we only consider $k < \pi/d$.

6.5 Summary and further work

We have developed a hydrodynamic model to study metachronal coordination in arrays of cilia. Each cilium is modelled as an independently beating rotor on a lattice and the rotors are coupled hydrodynamically. We have looked at the dispersion relation and found that the wave frequency, ω, increases with system size and decreases with wavenumber as $1/|k|$. Hydrodynamic interactions are long range and instantaneous at low Reynolds number, so as wavelength $\to \infty$, an infinite number of rotors exert a force in the same direction, and the velocity at an individual cilium diverges. This is also the reason why ω increases with system size: increasing the system size increases the number of Stokeslets that act instantaneously and over long range on a particular cilium.

We considered the stability of different wavevectors and found that small wavenumbers are unstable. We require $|k| > 1$ and a direction close to symplectic or antiplectic for stable metachronism. It would be interesting to look at near field effects to see

how they reduce the range of wavevectors that give stable metachronism. The near field breaks the symmetry $k \to -k$ and includes the driving force coefficients A_1, B_1, as well as A_2, B_2 so forcing pattern could play an important role. Other effects that would be interesting to study include lattice shape, non-circular trajectory shapes and noise. Are there some lattice where metachronal waves emerge more quickly, and are these the shapes we see in nature? Flexibility is an important effect to study as it plays an important role in synchronisation.

Metachronal waves in the colony *Volvox* have been observed and the spacing between cilia is $\sim 20\mu$m, so the far field approximation is suitable, however, in other organisms such as *Paramecium* the cilia are closer together so near field and steric interactions should be considered. If cilia are very close together then elastic coupling through the substrate might also have some effect.

An interesting effect that has not been considered is curvature. Spherical *Volvox* colonies can have a radius as small as 60μm, so we expect the curvature to affect the behaviour. Brumley *et al.* observed metachronal waves in *Volvox* colonies and also observed periodic phase defects [71]. They used a hydrodynamic model to show that these periodic phase defects occur if there is a difference in the intrinsic beat velocity between the cells in the anterior and posterior hemispheres. However, it is possible that curvature could cause phase differences and this is an important effect to study in future work. Experimentally, this could be investigated by studying metachronal coordination in *Volvox* colonies of different sizes.

Here, we have considered beads that all beat with the same beat pattern, but another question is what if they have different beat patterns and comparable intrinsic phase velocities? This question has relevance when there is a reversal in beat direction, for example, *Paramecium* can switch its beat direction and swim backwards. What happens during the switch? Do all cilia reverse their beat pattern simultaneously, or is there a period when different cilia have different beat patterns and what happens in this period? It is important for robustness that cilia can form metachronal waves for motility or fluid pumping if a small number of cilia are not beating properly.

Chapter 7

Summary and Conclusions

We have used hydrodynamic models to understand the behaviour of microorganisms that swim in a low Reynolds number environment. We have considered motility near a surface, synchronisation and metachronism, run-and-tumble and phototaxis. Our models have demonstrated that physical interactions, particularly hydrodynamic friction, hydrodynamic interactions and mechanical constraints play important roles in the behaviour of microorganisms. Hydrodynamic interactions cause bacteria swimming near surfaces to swim in circles [35], and we showed that friction between pili and the surface gives the two distinct near-surface swimming motility modes that are observed in *V. cholerae* [40]. When *Shewanella* is partially stuck to the surface, varying the proportion of the flagellum that is stuck to the surface affects the behaviour of the cell body. Hydrodynamic friction on the flagella in *Chlamydomonas*, and the rotation of the flagella through their constraint to the cell body leads to different synchronisation properties, depending on the beat pattern. We demonstrated that internal noise in the beat pattern can lead to run-and-tumble behaviour. We showed how a simple coupling between the beat pattern and light intensity that is consistent with observations causes the cell to steer towards or away from a light source. We have seen how hydrodynamic interactions allow metachronal waves to emerge in arrays of cilia and studied the dispersion relation and the stability of different wavevectors.

In chapter 2 we saw that when *V. cholerae* swims near a surface, two distinct motility modes are observed: roaming and orbiting. During roaming motion, the cells meander across the surface and the curvature of the trajectory is small; orbiting cells move on small circular tracjectories, repeatedly moving over the same patch of surface. We have developed a hydrodynamic model of *V. cholerae* based on the model developed by Lauga *et al.* which they used to understand why bacteria swim in circles when they are close to a boundary [35]. Lauga's model demonstrates that *E. coli* cells swim in clockwise circles in order to maintain a torque free condition as the head and

flagellum rotate in opposite directions. When used with appropriate parameters for *V. cholerae*, the radius of curvature predicted by Lauga's motion is much larger than that observed in orbiting cells; we do not see orbiting motility in the mutant $\Delta mshA$, which does not have MSHA pili.

We developed Lauga's model by adding an interaction between the pili and the surface. The interaction varies as the head rotates and the pili sweep past the surface [40]. The strength of the interaction between the pili and the surface is described by a parameter γ. The radius of curvature has a nonlinear dependence on the interaction strength, γ; our model shows that if the interaction between the pili and the surface is small, then the cell travels with roaming motility, otherwise the interaction causes the cell to move with orbiting motility. Observations of the cell show the angle between the cell orientation and the swimming direction varies along the trajectory. Our model shows that this variation in angle can be caused by the time dependence of the interaction strength, which varies because the head rotates and the pili sweep past the surface then rotate away from the surface.

V. cholerae does not have surface motility modes, unlike the model organism *Pseudomonas aeruginosa*. In *V. cholerae* there is strong correlation between the site of irreversible attachment and the location of biofilms. The near-surface motility of *V. cholerae* provides the first step towards biofilm formation: roaming motility allows the cell to travel around the surface, but when the interaction is strong the cell moves with orbiting motility and stays over the same patch of surface, which the cell could attach to. Subsequent stages in biofilm formation are presented in reference [53].

We do not know of observations of other bacteria that swim with both orbiting and roaming motility close to a surface. Since our model only considers a general interaction between the cell and the surface and not an interaction specific to *V. cholerae*, we expect that other similar bacteria with pili should be able to perform similar motion. If orbiting and roaming motility is not found in other bacteria then a question for future work is what behaviour does the model produce if we include a chemical interaction with the surface that binds and unbinds during the motion? The strength of such an interaction would not depend on the velocity of the cell, but the binding and unbinding rate would depend on the rotational velocity of the cell head.

Different types of behaviour have been observed in *Shewanella* when it is partially constrained by a surface. In chapter 3 we developed a model with flexibility between the head and the flagellum, and flexibility between the constrained and free parts of the flagellum. The flexibility between the constrained and free parts of the flagellum

depends on the length of the free part of the flagellum. We showed that there is different behaviour in the free part of the bacterium for different degrees of constraint between the flagellum and the surface, as well as for different flexibilities of the flagellar hook and torque exerted by the flagellar motor.

When the flagellum is partially constrained, the free part of the flagellum stands upright and the behaviour of the head depends on the flexibility of the flagellar hook and motor torque. When the head is completely free to rotate and only fixed at the end to prevent translation, the head and flagellum align and their behaviour depends on the hook flexibility and the motor torque: for large flexibility or motor torque the flagellum and head sweep close to the surface then stand upright while rotating about the surface normal at the point of attachment; when the hook is stiff or the torque is small the flagellum and head slowly stand up while rotating about the surface normal at the point of attachment. When the flagellum is completely constrained, either the cell head partially stands with an oscillating angle and rotates about the surface normal when the hook flexibility or the motor torque is large, or the cell makes a small angle with the surface and spins about its own axis while maintaining a constant orientation when the hook flexibility or motor torque is small. Transitions between the different types of behaviour occur when there is a change in how much of the flagellum is constrained or a change in the torque exerted by the flagellar motor.

MSHA pili are required for biofilm formation, but flagella are essential for building the structure of the biofilm [60]. The flagellum is thought to play a role in overcoming repulsive surface forces and spreading the biofilm, and is also important for surface attachment on rough surfaces [61, 62]. The results of our model indicate that when the flagellum is partially constrained by the surface the free part of the flagellum usually stands up, keeping the head away from the surface. However, if the flagellum becomes completely constrained then the cell head stays close to the surface, giving the pili opportunity to attach irreversibly.

In further developments we are currently considering the effect of different head shapes and comparing with observations of *V. cholerae* and *P. aeruginosa*. Another development that would be interesting to study is the effect of pili, which we saw are important for near-surface motility in chapter 2. Our model considers the effect of how much of the flagellum is attached to the surface, so an important question is what controls flagellar attachment and how easily can part of the flagellum attach or detach from the surface?

In chapter 4 we studied swimming behaviour and flagellar synchronisation in the alga *Chlamydomonas*. During forward swimming of *Chlamydomonas*, the two flagella

beat synchronously with a breaststroke-like motion. Forward swimming is interrupted by brief asynchronies, where the cell rapidly reorients [67]. In chapter 4 we developed a model of *Chlamydomonas* where the flagella are represented as beads driven around circular trajectories and a third bead represents the cell body. This model was inspired by a comparison of the flow field around *Chlamydomonas* with the flow field around three Stokeslets [141].

Chlamydomonas swims in a low Reynolds number environment, so time reversal symmetry must be broken in order to achieve net propulsion. In our model, during the forwards half of the stroke the flagella beads are further from each other than in the backwards half of the stroke, so hydrodynamic interactions are stronger in the backwards half of the stroke. The difference in hydrodynamic interaction strength in the two halves of the stroke cycle breaks the time reversal symmetry and allows the model to swim.

Some degree of flexibility or phase dependent forcing is required for hydrodynamic synchronisation of two beads. We use a phase dependent driving force in our model and find that synchronisation is sensitive to the force profile [100]. Surprisingly, we find that hydrodynamic interactions are not necessary for synchronisation; the flagellar beads couple via the rotation of the cell body [90, 102]. Phase dependent driving is required for synchronisation during forward swimming.

We added intrinsic noise to the amplitude in the driving force and run-and-tumble behaviour emerged, where the flagella beat synchronously during straight 'runs', which are interrupted by short 'tumbles', asynchronies causing reorientation [99]. The distribution of run durations follows an exponential distribution, indicating a Poisson process. This model shows that run-and-tumble behaviour in *Chlamydomonas* can occur from nonlinearities and internal noise, and that biochemical signalling is not necessary. This is in contrast to run-and-tumble in bacteria, where tumbles result from a discrete change in the rotation direction of one or more of the flagella. In *E. coli* the direction changes are controlled by the concentration of CheY [109]. *E. coli* use run-and-tumble for chemotaxis by increasing their run duration when they move up a concentration gradient of an attractant. Bacteria measure concentration gradients by comparing the concentration of an attractant at different times [112–114] and larger eukaryotes measure concentration gradients by comparing concentrations at opposite ends of the cell [149, 150]. Evidence suggests that *Chlamydomonas* uses different mechanisms for chemotaxis towards ammonium and sugars [147]. In our model, the mean run duration increases with decreasing internal noise strength, and it is possible that the concentration of an attractant could affect the relative internal

noise, which could give a mechanism for phototactic steering using run-and-tumble with variable run durations. However, we do not know enough yet about chemotaxis in *Chlamydomonas* to develop our model for chemotaxis. We would like to see tracking experiments showing how *Chlamydomonas* moves up concentration gradients of different attractants so we can develop the model to elucidate a mechanism. Tracking experiments would reveal if *Chlamydomonas* uses run-and-tumble as a strategy for chemotaxis, and if it does not use run-and-tumble, we are left with the question why has *Chlamydomonas* evolved so that it performs run-and-tumble? It has been suggested as method to avoid predators [111], but it is likely that there are other reasons.

Chlamydomonas displays both positive and negative phototaxis. Observations on fixed cells showed that the beat amplitude of the two flagella respond in opposite senses to light stimuli [123]. In section 5 we used the three-sphere model to understand the mechanism of phototactic steering based on changes to the flagellar beat amplitude in response to light. The cell rotates slowly about its body axis, so it sees a varying light signal. The flagellar response to light causes the cell to rotate in the flagellar plane, and the combination of this angular velocity and the slow rotation around the body axis gives helical motion. The pitch angle of the helix varies as the light seen by the eyespot varies, and this change in pitch angle causes the helix axis (the net direction of the cell) to bend towards or away from the light, depending on whether the eyespot moves around on the inside or the outside of the helix. The sign of the parameter that controls the flagellar response determines the direction of the net angular velocity in the flagellar plane, which determines whether the eyespot moves on the inside or outside of the helix, and therefore the determines the direction of phototaxis. The magnitude of the parameter that controls flagellar response determines how sharply the cell turns towards or away from the light. The three-sphere model that we used to study synchronisation and run-and-tumble also provides us with insight into how the observed flagellar responses result in steering towards or away from the light [101].

We would like to see tracking experiments performed on phototaxing cells to see if they all steer at the same rate to the light or if there is a spread of steering rates. We would also like to observe cells in periodic light to test our prediction that cells should still phototax if the period is several times longer than the *Chlamydomonas* rate and shorter than the mean run duration. There are many factors that include the direction of phototaxis and a question for future work is how does an individual

cell and a population of cells transition from one direction of phototaxis to the other direction.

We also considered synchronisation in an array of cilia in chapter 6. Metachronal waves are observed in arrays of cilia, for example on the surface of *Paramecium*. We modelled beating cilia as beads driven around fixed trajectories close to a surface and coupled by hydrodynamic interactions in the far field limit. We looked at the dispersion relation and found that the beat frequency increases with wavelength. This is because the fluid flow at cilium i induced by its neighbour $i+1$ has a larger component in the beat direction of cilium i for longer wavelengths. We considered the stability of different wavevectors on a square lattice and found that long wavelengths are unstable and the direction needs to be close to parallel or antiparallel to the beat direction for stability.

The far field approximation is suitable for modelling the colony *Volvox* where the cilia are far apart, but for other organisms where the cilia are closer together, for example *Paramecium*, the near field effects should be considered in future work. Other effects which should be studied include lattice shape, curvature of the surface, differences in beat pattern and flexibility.

In this thesis we have studied several physical models of microorganisms which demonstrate that observed features in behaviour emerge from physical interactions including hydrodynamic friction, hydrodynamic interactions and rigid constraints. Microorganisms have evolved and adapted to their low Reynolds number environment and the behaviours that we have studied here are important for the survival and growth of the microorganisms: the near surface motility is important for biofilm formation; *Chlamydomonas* is photosynthetic so phototaxis is important and it has been suggested that it uses run-and-tumble motion to evade predators [111]; ciliated organisms use metachronal coordination to find nutrients, either by swimming or pumping fluid. There are many open questions about the behaviour of microorganisms and the success of our physical modelling here suggests that physical models will be useful in revealing further insights.

Appendix A

Linear stability and the three-sphere model

We note that linear stability analysis can not be used to probe the stability of synchronszation, as we cannot perform a valid Taylor expansion when $H\cos\phi + L\sin\phi = 0$. For linearised driving force profiles, $F_l^t(\phi - \delta/2) \approx F_0(\phi) - F_1(\phi)\delta/2$, $F_r^t(\phi + \delta/2) \approx F_0(\phi) + F_1(\phi)\delta/2$, if we Taylor expand, then the linearised expression for δ' is

$$\frac{\mathrm{d}\delta}{\mathrm{d}\phi} \approx \frac{f(\phi; F_0, F_1)}{(H\cos\phi + L\sin\phi)^2}\delta, \tag{A.1}$$

which has a singularity at $\phi = \phi_\mathrm{s}$, where $H\cos\phi_\mathrm{s} + L\sin\phi_\mathrm{s} = 0$. The apparent singularity actually occurs at $\phi_\mathrm{l} = \phi_\mathrm{s}$ and at $\phi_\mathrm{r} = \phi_\mathrm{s}$ in the full expression, but the constraining force ensures this zero in the denominator is cancelled by the numerator. However, when we expand in δ we shift the zero in the denominator so that it occurs at $\phi = \phi_\mathrm{s}$, then the numerator is no longer zero at this point. The zero in the denominator arises from over-constraining the torque free condition when $\phi_i = \phi_\mathrm{s}$. The torque free condition (4.4) is

$$\begin{aligned} 0 &= (\mathbf{R}_\mathrm{l} - \mathbf{R}_\mathrm{b}) \times \mathbf{F}_\mathrm{l} + (\mathbf{R}_\mathrm{r} - \mathbf{R}_\mathrm{b}) \times \mathbf{F}_\mathrm{r}, \\ &= \big(F_\mathrm{l}^t(-L\cos\phi_\mathrm{l} + H\sin\phi_\mathrm{l} + b) + F_l^n(-L\sin\phi_\mathrm{l} - H\cos\phi_\mathrm{l}) + \\ &\quad F_\mathrm{r}^t(L\cos\phi_\mathrm{r} - H\sin\phi_\mathrm{r} - b) + F_r^n(L\sin\phi_\mathrm{r} + H\cos\phi_\mathrm{r})\big)\hat{\mathbf{z}}. \end{aligned} \tag{A.2}$$

We use (A.2), along with (4.1,4.2,4.3,4.54.6,4.7), to solve for the constraining forces F_i^n, $i = \mathrm{l}, \mathrm{r}$. At $\phi_i = \phi_\mathrm{s}$, F_i^n is multiplied by a term which vanishes, so the torque free condition is be satisfied without specifying F_i^n. We over-constrain the system when we specify F_i^n at $\phi_i = \phi_\mathrm{s}$. Geometrically, ϕ_s corresponds to the phase where $\mathbf{R}_i - \mathbf{R}_b$ is parallel to $\hat{\mathbf{n}}_i$.

Appendix B

Cilia Phase Equations

B.1 Phase equation in original gauge

Using the notation defined in equation (6.10), we write the phase equation (6.9) as

$$
\begin{aligned}
\dot{\phi} \;=\; & \frac{F(\phi_i)}{\xi b} + \sum_{r'} \int \frac{d^2q}{(2\pi)^2} \frac{F(\phi')}{4\eta b} e^{\mathrm{i}q.(r-r')} \Bigg\{ \Big[f_\alpha f_\beta \sin\phi \sin\phi' \\
& + g_\alpha g_\beta \cos\phi \cos\phi' - f_\alpha g_\beta \sin\phi \cos\phi' - g_\alpha f_\beta \cos\phi \sin\phi' \Big] \\
& \cdot \frac{1}{|q|} \Big[\big(\delta_{\alpha\beta}(1 - e^{-2h|q|}) - 2h^2 q_\alpha q_\beta e^{-2h|q|} \big) + \delta_{\alpha\beta}(-b|q||f_3|\sin\phi - \sin\phi'| \\
& - e^{-2h|q|}|q|bf_3(\sin\phi + \sin\phi')) - 2hbf_3(\sin\phi + \sin\phi')q_\alpha q_\beta e^{-2h|q|}(1 - h|q|) \\
& + \mathrm{i}q_\gamma b(f_\gamma(\cos\phi - \cos\phi') + g_\gamma(\sin\phi - \sin\phi'))(\delta_{\alpha\beta}(1 - e^{-2h|q|}) \\
& - 2h^2 q_\alpha q_\beta e^{-2h|q|}) \Big] + \mathrm{i} \Big[- f_3 f_\alpha \cos\phi \sin\phi' + f_3 g_\alpha \cos\phi \cos\phi' \Big] \\
& \frac{q_\alpha}{|q|} \Big[- 2h^2|q|e^{-2h|q|} + bf_3(\sin\phi - \sin\phi')(e^{-2h|q|} - 1) \\
& - 2hbf_3(\sin\phi + \sin\phi')|q|e^{-2h|q|}(1 - h|q|) - \mathrm{i}2h^2|q|e^{-2h|q|}bq_\gamma \\
& \cdot \big(f_\gamma(\cos\phi - \cos\phi') + g_\gamma(\sin\phi - \sin\phi') \big) \Big] + \mathrm{i} \Big[- f_\alpha f_3 \sin\phi \cos\phi' \\
& + g_\alpha f_3 \cos\phi \cos\phi' \Big] \frac{q_\alpha}{|q|} \Big[2h^2|q|e^{-2h|q|} + bf_3(\sin\phi - \sin\phi')(e^{-2h|q|} - 1) \\
& + 2hbf_3(\sin\phi + \sin\phi')|q|e^{-2h|q|}(1 - h|q|) + \mathrm{i}2h^2|q|e^{-2h|q|}bq_\gamma \\
& \cdot \big(f_\gamma(\cos\phi - \cos\phi') + g_\gamma(\sin\phi - \sin\phi') \big) \Big] + f_3^2 \cos\phi \cos\phi' \Big[\frac{1 - e^{-2h|q|}}{|q|} \\
& - 2h(1 + h|q|e^{-2h|q|}) + 2h^2 q^2 bf_3(\sin\phi + \sin\phi')e^{-2h|q|} + \mathrm{i}bq_\gamma \big(f_\gamma(\cos\phi \\
& - \cos\phi') + g_\gamma(\sin\phi - \sin\phi') \big) \Big(\frac{1 - e^{-2h|q|}}{|q|} - 2h(1 + h|q|)e^{-2h|q|} \Big) \Big] \Bigg\}. \qquad \text{(B.1)}
\end{aligned}
$$

Terms coloured blue are near field contributions. The remaining terms in black are the far field contributions.

B.2 Phase equation in constant velocity gauge to first order in perturbation

We look for plane wave solutions of the form given in equation (6.17). Expanding the phase equation (6.15) to linear order in $\delta\Phi - \delta\Phi'$ gives the following expression:

$$
\begin{aligned}
\dot{\Phi} \;=\; & \frac{F_0}{\xi b} + \frac{F_0}{4\eta b}\sum_{r'}\int \frac{d^2q}{(2\pi)^2} e^{\mathrm{i}q.(r-r')}\Bigg\{ \frac{1}{|q|}\Big(\delta_{\alpha\beta}(1-e^{-2h|q|}) - 2h^2 q_\alpha q_\beta e^{-2h|q|}\Big) \\
& \cdot\Bigg[f_\alpha f_\beta \Bigg(\Big(1+\frac{A_2}{2}\Big)\Big[\frac{e^{\mathrm{i}k.(r-r')}+e^{-\mathrm{i}k.(r-r')}}{4} + (\delta\Phi-\delta\Phi')\frac{e^{\mathrm{i}k.(r-r')}-e^{-\mathrm{i}k.(r-r')}}{4\mathrm{i}}\Big] \\
& + B_2\Big[\frac{-e^{\mathrm{i}k.(r-r')}+e^{-\mathrm{i}k.(r-r')}}{4\mathrm{i}} + (\delta\Phi-\delta\Phi')\frac{e^{\mathrm{i}k.(r-r')}+e^{-\mathrm{i}k.(r-r')}}{4}\Big]\Bigg) \\
& + g_\alpha g_\beta\Bigg(\Big(1-\frac{A_2}{2}\Big)\Big[\frac{e^{\mathrm{i}k.(r-r')}+e^{-\mathrm{i}k.(r-r')}}{4} + (\delta\Phi-\delta\Phi')\frac{e^{\mathrm{i}k.(r-r')}-e^{-\mathrm{i}k.(r-r')}}{4\mathrm{i}}\Big] \\
& - B_2\Big[\frac{-e^{\mathrm{i}k.(r-r')}+e^{-\mathrm{i}k.(r-r')}}{4\mathrm{i}} + (\delta\Phi-\delta\Phi')\frac{e^{\mathrm{i}k.(r-r')}+e^{-\mathrm{i}k.(r-r')}}{4}\Big]\Bigg) \\
& - f_\alpha g_\beta\Bigg(\big(1+A_2\big)\Big[\frac{-e^{\mathrm{i}k.(r-r')}+e^{-\mathrm{i}k.(r-r')}}{4\mathrm{i}} + (\delta\Phi-\delta\Phi')\frac{e^{\mathrm{i}k.(r-r')}+e^{-\mathrm{i}k.(r-r')}}{4}\Big] \\
& - \frac{B_2}{2}\Big[\frac{e^{\mathrm{i}k.(r-r')}+e^{-\mathrm{i}k.(r-r')}}{4} + (\delta\Phi-\delta\Phi')\frac{e^{\mathrm{i}k.(r-r')}-e^{-\mathrm{i}k.(r-r')}}{4\mathrm{i}}\Big]\Bigg) \\
& - g_\alpha f_\beta\Bigg(\big(-1+A_2\big)\Big[\frac{-e^{\mathrm{i}k.(r-r')}+e^{-\mathrm{i}k.(r-r')}}{4\mathrm{i}} + (\delta\Phi-\delta\Phi')\frac{e^{\mathrm{i}k.(r-r')}+e^{-\mathrm{i}k.(r-r')}}{4}\Big] \\
& - \frac{B_2}{2}\Big[\frac{e^{\mathrm{i}k.(r-r')}+e^{-\mathrm{i}k.(r-r')}}{4} + (\delta\Phi-\delta\Phi')\frac{e^{\mathrm{i}k.(r-r')}-e^{-\mathrm{i}k.(r-r')}}{4\mathrm{i}}\Big]\Bigg)\Bigg] \\
& - \mathrm{i}q_\alpha 2h^2 e^{-2h|q|}\Bigg[- f_3 f_\alpha\Bigg((-1+A_2)\Big[\frac{-e^{\mathrm{i}k.(r-r')}+e^{-\mathrm{i}k.(r-r')}}{4\mathrm{i}} \\
& + (\delta\Phi-\delta\Phi')\frac{e^{\mathrm{i}k.(r-r')}+e^{-\mathrm{i}k.(r-r')}}{4}\Big] - \frac{B_2}{2}\Big[\frac{e^{\mathrm{i}k.(r-r')}+e^{-\mathrm{i}k.(r-r')}}{4} \\
& + (\delta\Phi-\delta\Phi')\frac{e^{\mathrm{i}k.(r-r')}-e^{-\mathrm{i}k.(r-r')}}{4\mathrm{i}}\Big]\Bigg) + f_3 g_\alpha\Bigg(\Big(1-\frac{A_2}{2}\Big)\Big[\frac{e^{\mathrm{i}k.(r-r')}+e^{-\mathrm{i}k.(r-r')}}{4} \\
& + (\delta\Phi-\delta\Phi')\frac{e^{\mathrm{i}k.(r-r')}-e^{-\mathrm{i}k.(r-r')}}{4\mathrm{i}}\Big] - B_2\Big[\frac{-e^{\mathrm{i}k.(r-r')}+e^{-\mathrm{i}k.(r-r')}}{4\mathrm{i}} + \ldots
\end{aligned}
$$

$$\ldots + (\delta\Phi - \delta\Phi')\frac{e^{\mathrm{i}k.(r-r')} + e^{-\mathrm{i}k.(r-r')}}{4}\Big]\Big)\Big] + \mathrm{i}q_\alpha 2h^2 e^{-2h|q|}\Big[- f_\alpha f_3\Big((1+A_2)$$
$$\cdot\Big[\frac{-e^{\mathrm{i}k.(r-r')} + e^{-\mathrm{i}k.(r-r')}}{4\mathrm{i}} + (\delta\Phi - \delta\Phi')\frac{e^{\mathrm{i}k.(r-r')} + e^{-\mathrm{i}k.(r-r')}}{4}\Big]$$
$$-\frac{B_2}{2}\Big[\frac{e^{\mathrm{i}k.(r-r')} + e^{-\mathrm{i}k.(r-r')}}{4} + (\delta\Phi - \delta\Phi')\frac{e^{\mathrm{i}k.(r-r')} - e^{-\mathrm{i}k.(r-r')}}{4\mathrm{i}}\Big]\Big)$$
$$+g_\alpha f_3\Big((1-\frac{A_2}{2})\Big[\frac{e^{\mathrm{i}k.(r-r')} + e^{-\mathrm{i}k.(r-r')}}{4} + (\delta\Phi - \delta\Phi')\frac{e^{\mathrm{i}k.(r-r')} - e^{-\mathrm{i}k.(r-r')}}{4\mathrm{i}}\Big]$$
$$-B_2\Big[\frac{-e^{\mathrm{i}k.(r-r')} + e^{-\mathrm{i}k.(r-r')}}{4\mathrm{i}} + (\delta\Phi - \delta\Phi')\cdot\frac{e^{\mathrm{i}k.(r-r')} + e^{-\mathrm{i}k.(r-r')}}{4}\Big]\Big)\Big]$$
$$+f_3^2\Big(\frac{1-e^{-2h|q|}}{|q|} - 2h(1+h|q|)e^{-2h|q|}\Big)\Big((1-\frac{A_2}{2})\Big[\frac{e^{\mathrm{i}k.(r-r')} + e^{-\mathrm{i}k.(r-r')}}{4}$$
$$+(\delta\Phi - \delta\Phi')\frac{e^{\mathrm{i}k.(r-r')} - e^{-\mathrm{i}k.(r-r')}}{4\mathrm{i}}\Big] - B_2\Big[\frac{-e^{\mathrm{i}k.(r-r')} + e^{-\mathrm{i}k.(r-r')}}{4\mathrm{i}}$$
$$+(\delta\Phi - \delta\Phi')\frac{e^{\mathrm{i}k.(r-r')} + e^{-\mathrm{i}k.(r-r')}}{4}\Big]\Big)\Big\} \tag{B.2}$$

The terms in red cancel.

B.3 Dispersion Relation

The leading order terms in equation (B.2) give the dispersion relation:

$$\begin{aligned}
\omega \;=\; & \frac{F_0}{\xi b} + \frac{F_0}{4\eta b}\sum_{r'}\int \frac{d^2q}{(2\pi)^2} e^{\mathrm{i}q.(r-r')}\Bigg\{ \frac{1}{|q|}\Big(\delta_{\alpha\beta}(1-e^{-2h|q|}) - 2h^2 q_\alpha q_\beta e^{-2h|q|}\Big) \\
& \cdot\Bigg[f_\alpha f_\beta\Bigg((1+\frac{A_2}{2})\Big[\frac{e^{\mathrm{i}k.(r-r')}+e^{-\mathrm{i}k.(r-r')}}{4}\Big] + B_2\Big[\frac{-e^{\mathrm{i}k.(r-r')}+e^{-\mathrm{i}k.(r-r')}}{4\mathrm{i}}\Big]\Bigg) \\
& + g_\alpha g_\beta\Bigg((1-\frac{A_2}{2})\Big[\frac{e^{\mathrm{i}k.(r-r')}+e^{-\mathrm{i}k.(r-r')}}{4}\Big] - B_2\Big[\frac{-e^{\mathrm{i}k.(r-r')}+e^{-\mathrm{i}k.(r-r')}}{4\mathrm{i}}\Big]\Bigg) \\
& - f_\alpha g_\beta\Bigg((1+A_2)\Big[\frac{-e^{\mathrm{i}k.(r-r')}+e^{-\mathrm{i}k.(r-r')}}{4\mathrm{i}}\Big] - \frac{B_2}{2}\Big[\frac{e^{\mathrm{i}k.(r-r')}+e^{-\mathrm{i}k.(r-r')}}{4}\Big]\Bigg) \\
& - g_\alpha f_\beta\Bigg((-1+A_2)\Big[\frac{-e^{\mathrm{i}k.(r-r')}+e^{-\mathrm{i}k.(r-r')}}{4\mathrm{i}}\Big] - \frac{B_2}{2}\Big[\frac{e^{\mathrm{i}k.(r-r')}+e^{-\mathrm{i}k.(r-r')}}{4}\Big]\Bigg)\Bigg] \\
& - \mathrm{i}q_\alpha 4h^2 e^{-2h|q|}\Bigg[f_3 f_\alpha\Bigg(\Big[\frac{-e^{\mathrm{i}k.(r-r')}+e^{-\mathrm{i}k.(r-r')}}{4\mathrm{i}}\Big]\Bigg)\Bigg] + f_3^2\Bigg(\frac{1-e^{-2h|q|}}{|q|} \\
& - 2h(1+h|q|)e^{-2h|q|}\Bigg)\Bigg((1-\frac{A_2}{2})\Big[\frac{e^{\mathrm{i}k.(r-r')}+e^{-\mathrm{i}k.(r-r')}}{4}\Big] \\
& - B_2\Big[\frac{-e^{\mathrm{i}k.(r-r')}+e^{-\mathrm{i}k.(r-r')}}{4\mathrm{i}}\Big]\Bigg)\Bigg\} \qquad \text{(B.3)}
\end{aligned}$$

We perform the sum over r' and integrate over q in the main text in section 6.3.

B.4 Stability of a plane wave

We look at whether a perturbation to a plane wave solution grows or decays to determine the stability of the wave. The Fourier transform of the growth rate in

equation (6.27) is the following:

$$
\begin{aligned}
\tilde{c}(q') \;=\; & \frac{F_0}{4\eta b d^2}\sum_G \int d^2q \Bigg\{ \frac{1}{|q|}\Big(\delta_{\alpha\beta}(1-e^{-2h|q|}) - 2h^2 q_\alpha q_\beta e^{-2h|q|}\Big)\Bigg[f_\alpha f_\beta \\
& \cdot\Big(\frac{1}{4\mathrm{i}}(1+\frac{A_2}{2})\big(\delta(q-q'+k+G)-\delta(q-q'-k+G)\big) \\
& +\frac{B_2}{4}\big(\delta(q-q'+k+G)+\delta(q-q'-k+G)\big)\Big) + g_\alpha g_\beta\Big(\frac{1}{4\mathrm{i}}(1-\frac{A_2}{2}) \\
& \cdot\big(\delta(q-q'+k+G)-\delta(q-q'-k+G)\big) - \frac{B_2}{4}\big(\delta(q-q'+k+G) \\
& +\delta(q-q'-k+G)\big)\Big) - f_\alpha g_\beta\Big(\frac{1}{4}(1+A_2)\big(\delta(q-q'+k+G) \\
& +\delta(q-q'-k+G)\big) - \frac{B_2}{8\mathrm{i}}\big(\delta(q-q'+k+G)-\delta(q-q'-k+G)\big)\Big) \\
& -g_\alpha f_\beta\Big(\frac{1}{4}(-1+A_2)\big(\delta(q-q'+k+G)+\delta(q-q'-k+G)\big) \\
& -\frac{B_2}{8\mathrm{i}}\big(\delta(q-q'+k+G)-\delta(q-q'-k+G)\big)\Big)\Bigg] - \mathrm{i}q_\alpha 4h^2 e^{-2h|q|}\frac{f_3 f_\alpha}{4} \\
& \cdot\big(\delta(q-q'+k+G)+\delta(q-q'-k+G)\big) + f_3^2\Big(\frac{1-e^{-2h|q|}}{|q|} \\
& -2h(1+h|q|)e^{-2h|q|}\Big)\Big(\frac{1}{4\mathrm{i}}(1-\frac{A_2}{2})\big(\delta(q-q'+k+G) \\
& -\delta(q-q'-k+G)\big) - \frac{B_2}{4}\big(\delta(q-q'+k+G) \\
& +\delta(q-q'-k+G)\big)\Big)\Bigg\}. \qquad \text{(B.4)}
\end{aligned}
$$

Bibliography

[1] E. M. Purcell. Life at low reynolds number. *Am. J. Phys.*, 45:3–11, 1977. doi: 10.1119/1.10903.

[2] Alfred Shapere and Frank Wilczek. Geometry of self-propulsion at low reynolds number. *J. Fluid Mech.*, 198:557–585, 1989. doi: 10.1017/S0022112089000261.

[3] Eric Lauga and Thomas R. Powers. The hydrodynamics of swimming microorganisms. *Rep. Prog. Phys.*, 72:096601, 2009. doi: 10.1088/0034-4885/72/9/096601.

[4] Ali Najafi and Ramin Golestanian. Simple swimmer at low reynolds number: Three linked spheres. *Phys. Rev. E*, 69:062901, 2004. doi: 10.1103/PhysRevE.69.062901.

[5] Rémi Dreyfus, Jean Baudry, and Howard A. Stone. Purcell's 'rotator': mechanical rotation at low reynolds number. *Eur. Phys. J. B*, 47:161–164, 2005. doi: 10.1140/epjb/e2005-00302-5.

[6] J. E. Avron, O. Kenneth, and D. H. Oaknin. Pushmepullyou: an efficient micro-swimmer. *New J. Phys.*, 7:234, 2005. doi: 10.1088/1367-2630/7/1/234.

[7] Marco Leoni, Jurij Kotar, Bruno Bassetti, Pietro Cicuta, and Marco Cosentino Lagomarsino. A basic swimmer at low reynolds number. *Soft Matter*, 5:472–476, 2009. doi: 10.1039/B812393D.

[8] Geoffrey I. Taylor. Analysis of the swimming of microscopic organisms. *Proc. R. Soc. A*, 209:447–461, 1951. doi: 10.1098/rspa.1951.0218.

[9] Christopher. Brennen and Howard Winet. Fluid mechanics of propulsion by cilia and flagella. *Ann. Rev. Fluid Mech.*, 9:339–398, 1977. doi: 10.1146/annurev.fl.09.010177.002011.

[10] Pietro Tierno, Ramin Golestanian, Ignacio Pagonabarraga, and Fransesc Sagues. Controlled swimming in confined fluids of magnetically actuated colloidal rotors. *Phys. Rev. Lett.*, 101:218304, 2008. doi: 10.1103/PhysRevLett.101.218304.

[11] Rémi Dreyfus, Jean Baudry, Marcus L. Roper, Marc Fermigier, Howard A. Stone, and Jérôme Bibette. Microscopic artificial swimmers. *Nature*, 437:862–865, 2005. doi: 10.1038/nature04090.

[12] A. Cēbers. Flexible magnetic filaments. *Curr. Opin. Colloid Interface Sci.*, 10: 167 – 175, 2005. doi: 10.1016/j.cocis.2005.07.002.

[13] Erik Gauger and Holger Stark. Numerical study of a microscopic artificial swimmer. *Phys. Rev. E*, 74:021907, 2006. doi: 10.1103/PhysRevE.74.021907.

[14] Marcus L. Roper, Rémi Dreyfus, Jean Baudry, Marc Fermigier, Jérôme Bibette, and Howard A. Stone. On the dynamics of magnetically driven elastic filaments. *J. Fluid Mech.*, 554:167–190, 2006. doi: 10.1017/S0022112006009049.

[15] Eric E. Keaveny and Martin R. Maxey. Spiral swimming of an artificial micro-swimmer. *J. Fluid Mech.*, 598:293– 319, 2008. doi: 10.1017/S0022112007009949.

[16] Brian J. Williams, Sandeep J. Anand, Jagannathan Rajagopalan, and M. Taher A. Saif. A self-propelled biohybrid swimmer at low reynolds number. *Nat. Commun.*, 5:3081, 2014. doi: 10.1038/ncomms4081.

[17] M. J. Lighthill. On the squirming motion of nearly spherical deformable bodies through liquids at very small Reynolds numbers. *Comm. Pure Appl. Math.*, 5: 109–118, 1952. doi: 10.1002/cpa.3160050201.

[18] J. R. Blake. A spherical envelope approach to ciliary propulsion. *J. Fluid Mech.*, 46:199–208, 1971. doi: 10.1017/S002211207100048X.

[19] Julia M. Yeomans, D. O. Pushkin, and Henry Shum. An introduction to the hydrodynamics of swimming microorganisms. *Eur. Phys. J. Special Topics*, 223: 1771–1785, 2014. doi: 10.1140/epjst/e2014-02225-8.

[20] Howard C. Berg. The rotary motor of bacterial flagella. *Annu. Rev. Biochem.*, 72:19–54, 2003. doi: 10.1146/annurev.biochem.72.121801.161737.

[21] Robert M. Macnab. Bacterial flagella rotating in bundles: A study in helical geometry. *Proc. Natl. Acad. Sci. U.S.A.*, 74:221–225, 1977.

[22] M. Reichert and H. Stark. Synchronization of rotating helices by hydrodynamic interactions. *Eur. Phys. J. E*, 17:493–500, 2005. doi: 10.1140/epje/i2004-10152-7.

[23] M Shigematsu, Y. Meno, H. Misumi, and K. Amako. The measurement of swimming velocity of *Vibrio cholerae* and *Pseudomonas aeruginosa* using the video tracking methods. *Microbiol Immunol.*, 39:741–744, 1995.

[24] Kwangmin Son, Jeffrey S. Guasto, and Roman Stocker. Bacteria can exploit a flagellar buckling instability to change direction. *Nature Phys.*, 9:494–498, 2013. doi: 10.1038/nphys2676.

[25] Linda Turner, William S. Ryu, and Howard C. Berg. Real-time imaging of fluorescent flagellar filaments. *J. Bacteriol.*, 182:2793–2801, 2000. doi: 10.1128/JB.182.10.2793-2801.2000.

[26] Shuang Zhou, Andrey Sokolov, Oleg D. Lavrentovich, and Igor S. Aranson. Living liquid crystals. *Proc. Natl. Acad. Sci. U.S.A.*, 111:1265–1270, 2014. doi: 10.1073/pnas.1321926111.

[27] A. J. Reynolds. The swimming of minute organisms. *J. Fluid Mech.*, 23:241–260, 1965. doi: 10.1017/S0022112065001337.

[28] David F. Katz. On the propulsion of micro-organisms near solid boundaries. *J. Fluid Mech.*, 64:33–49, 1974. doi: 10.1017/S0022112074001984.

[29] David F. Katz, J. R. Blake, and S. L. Paveri-Fontana. On the movement of slender bodies near plane boundaries at low reynolds number. *J. Fluid Mech.*, 72:529–540, 1975. doi: 10.1017/S0022112075003126.

[30] M. Ramia, D. L. Tullock, and N. Phan-Thien. The role of hydrodynamic interaction in the locomotion of microorganisms. *Biophys. J.*, 65:755–778, 1993. doi: 10.1016/S0006-3495(93)81129-9.

[31] Howard C. Berg and Linda Turner. Chemotaxis of bacteria in glass capillary arrays—*Escherichia coli*, motility, microchannel plate, and light scattering. *Biophys. J.*, 58:919–930, 1990. doi: 10.1016/S0006-3495(90)82436-X.

[32] Paul D. Frymier, Roseanne M. Ford, Howard C. Berg, and Peter T. Cummings. Three-dimensional tracking of motile bacteria near a solid planar surface. *Proc. Natl. Acad. Sci. U.S.A.*, 92:6195–6199, 1995.

[33] Yukio Magariyama, Makoto Ichiba, Kousou Nakata, Kensaku Baba, Toshio Ohtani, Seishi Kudo, and Tomonobu Goto. Difference in bacterial motion between forward and backward swimming caused by the wall effect. *Biophys. J.*, 88:3648–3658, 2005. doi: 10.1529/biophysj.104.054049.

[34] Tomonobu Goto, Kousou Nakata, Kensaku Baba, Masaharu Nishimura, and Yukio Magariyama. A fluid-dynamic interpretation of the asymmetric motion of singly flagellated bacteria swimming close to a boundary. *Biophys. J.*, 89: 3771–3779, 2005. doi: 10.1529/biophysj.105.067553.

[35] E. Lauga, W. R. DiLuzio, G. M. Whitesides, and H. A. Stone. Swimming in circles: motion of bacteria near solid boundaries. *Biophys. J.*, 90:400–412, 2006. doi: 10.1529/biophysj.105.069401.

[36] James Gray and G. J. Hancock. The propulsion of sea-urchin spermatozoa. *J. Exp. Biol.*, 32:802–814, 1955.

[37] James Lighthill. Flagellar hydrodynamics. *SIAM Rev.*, 18:161–230, 1976. doi: 10.1137/1018040.

[38] Robert E. Johnson. An improved slender-body theory for stokes flow. *J. Fluid Mech.*, 99:411–431, 1980. doi: 10.1017/S0022112080000687.

[39] Ricardo Cortez, Lisa Fauci, and Alexei Medovikov. The method of regularized stokeslets in three dimensions: Analysis, validation, and application to helical swimming. *Phys. Fluids*, 17:031504, 2005. doi: 10.1063/1.1830486.

[40] Andrew S. Utada, Rachel R. Bennett, Jiunn C. N. Fong, Maxsim L. Gibiansky, Fitnat H. Yildiz, Ramin Golestanian, and Gerard C. L. Wong. *Vibrio cholerae* use pili and flagella synergistically to effect motility switching and conditional surface attachment. *Nat. Commun.*, 5:4913, 2014. doi: 10.1038/ncomms5913.

[41] Paula I. Watnick and Roberto Kolter. Steps in the development of a *Vibrio cholerae* El Tor biofilm. *Mol. Microbiol.*, 34:586–595, 1999.

[42] Lisa Craig, Michael E. Pique, and John A. Tainer. Type IV pilus structure and bacterial pathogenicity. *Nature Rev. Microbiol.*, 4:363–378, 2004. doi: 10.1038/nrmicro885.

[43] K. Helene Thelin and Ronald K. Taylor. Toxin-coregulated pilus, but not mannose-sensitive hemagglutinin, is required for colonization by *Vibrio cholerae* o1 el tor biotype and o139 strains. *Infect. Immun.*, 64:2853–2856, 1996.

[44] Stephen R. Attridge, Paul A. Manning, Jan Holmgren, and Gunhild Jonson. Relative significance of mannose-sensitive hemagglutinin and toxin-coregulated pili in colonization of infant mice by *Vibrio cholerae* el tor. *Infect. Immun.*, 64: 3369–3373, 1996.

[45] C. O. Tacket, R. K. Taylor, G. Losonsky, Y. Lim, J. P. Nataro, J. B. Kaper, and M. M. Levine. Investigation of the roles of toxin-coregulated pili and mannose-sensitive hemagglutinin pili in the pathogenesis of *Vibrio cholerae* o139 infection. *Infect. Immun.*, 66:692–695, 1998.

[46] Deborah A. Chiavelli, Jane W. Marsh, and Ronald K. Taylor. The mannose-sensitive hemagglutinin of *Vibrio cholerae* promotes adherence to zooplankton. *Appl. Environ. Microbiol.*, 67:3220–3225, 2001. doi: 10.1128/AEM.67.7.3220-3225.2001.

[47] Paul R. Epstein. Algal blooms in the spread and persistence of cholera. *Biosystems*, 31:209–221, 1993. doi: 10.1016/0303-2647(93)90050-M.

[48] M. N. Guentzel and L. J. Berry. Motility as a virulence factor for *Vibrio cholerae*. *Infect. Immun.*, 11:890–897, 1975.

[49] M. N. Guentzel, L. H. Field, E. R. Eubanks, and L. J. Berry. Use of fluorescent antibody in studies of immunity to cholera in infant mice. *Infect. Immun.*, 15: 539–548, 1977.

[50] Kathleen Richardson. Roles of motility and flagellar structure in pathogenicity of *Vibrio cholerae*: Analysis of motility mutants in three animal models. *Infect. Immun.*, 59:2727–2736, 1991.

[51] Claudette L. Gardel and John J. Mekalanos. Alterations in *Vibrio cholerae* motility phenotypes correlate with changes in virulence factor expression. *Infect. Immun.*, 64:2246–2255, 1996.

[52] Susan M. Butler and Andrew Camilli. Both chemotaxis and net motility greatly influence the infectivity of *Vibrio cholerae*. *Proc. Natl. Acad. Sci. U.S.A.*, 101: 5018–5023, 2004. doi: 10.1073/pnas.0308052101.

[53] Jennifer K. Teschler, David Zamorano-Sánchez, Andrew S. Utada, Christopher J. A. Warner, Gerard C. L. Wong, Roger G. Linington, and Fitnat H. Yildiz. Living in the matrix: assembly and control of *Vibrio cholerae* biofilms. *Nature Rev. Microbiol.*, 13:255–268, 2015. doi: 10.1038/nrmicro3433.

[54] Maxsim L. Gibiansky, Jacinta C. Conrad, Fan Jin, Vernita D. Gordon, Dominick A. Motto, Margie A. Mathewson, Wiktor G. Stopka, Daria C. Zelasko, Joshua D. Shrout, and Gerard C. L. Wong. Bacteria use type IV pili to walk upright and detach from surfaces. *Science*, 330:197, 2010. doi: 10.1126/science.1194238.

[55] Jacinta C. Conrad, Maxsim L. Gibiansky, Fan Jin, Vernita D. Gordon, Dominick A. Motto, Margie A. Mathewson, Wiktor G. Stopka, Daria C. Zelasko, Joshua D. Shrout, and Gerard C. L. Wong. Flagella and pili-mediated near-surface single-cell motility mechanisms in *P. aeruginosa*. *Biophys. J.*, 100:1608–1616, 2011. doi: 10.1016/j.bpj.2011.02.020.

[56] Kun Zhao, Boo Shan Tseng, Bernard Beckerman, Fan Jin, Maxsim L. Gibiansky, Joe J. Harrison, Erik Luijten, Matthew R. Parsek, and Gerard C. L. Wong. Psl trails guide exploration and microcolony formation in *Pseudomonas aeruginosa* biofilms. *Nature*, 497:388–391, 2013. doi: 10.1038/nature12155.

[57] George O'Toole, Heidi B. Kaplan, and Roberto Kolter. Biofilm formation as microbial development. *Annu. Rev. Microbiol.*, 54:49–79, 2000. doi: 10.1146/annurev.micro.54.1.49.

[58] Calvin Lee and Gerard C. L. Wong. Private communication, 2015.

[59] Heidi H. Hau and Jeffrey A. Gralnick. Ecology and biotechnology of the genus *Shewanella*. *Annu. Rev. Microbiol.*, 61:237–258, 2007. doi: 10.1146/annurev.micro.61.080706.093257.

[60] Kai M. Thormann, Renée M. Saville, Soni Shukla, Dale A. Pelletier, and Alfred M. Spormann. Initial phases of biofilm formation in *Shewanella oneidensis* MR-1. *J. Bacteriol.*, 186:8096–8104, 2004. doi: 10.1128/JB.186.23.8096-8104.2004.

[61] Leslie A. Pratt and Roberto Kolter. Genetic analysis of *Escherichia coli* biofilm formation: roles of flagella, motility, chemotaxis and type I pili. *Mol. Microbiol.*, 30:285–293, 1998. doi: 10.1046/j.1365-2958.1998.01061.x.

[62] Ronn S. Friedlander, Hera Vlamakis, Philseok Kim, Mughees Khan, Roberto Kolter, and Joanna Aizenberg. Bacterial flagella explore microscale hummocks and hollows to increase adhesion. *Proc. Natl. Acad. Sci. U.S.A.*, 110:5624–5629, 2013. doi: 10.1073/pnas.1219662110.

[63] Ramin Golestanian, Julia M. Yeomans, and Nariya Uchida. Hydrodynamic synchronization at low reynolds number. *Soft Matter*, 7, 2011. doi: 10.1039/c0sm01121e.

[64] James Gray. *Ciliary movement*. Cambridge University Press, 1928.

[65] Yingzi Yang, Jens Elgeti, and Gerhard Gompper. Cooperation of sperm in two dimensions: Synchronization, attraction, and aggregation through hydrodynamic interactions. *Phys. Rev. E*, 78:061903, 2008. doi: 10.1103/PhysRevE.78.061903.

[66] U. Rüffer and W. Nultsch. High-speed cinematographic analysis of the movement of *chlamydomonas*. *Cell Motil. Cytoskel.*, 5:251–263, 1985. doi: 10.1002/cm.970050307.

[67] Marco Polin, Idan Tuval, Knut Drescher, J.P. Gollub, and Raymond E. Goldstein. *Chlamydomonas* swims with two "gears" in a eukaryotic version of run-and-tumble locomotion. *Science*, 325:487, 2009.

[68] Sidney L. Tamm and H. A. Horridge. The relation between the orientation of the central fibrils and the direction of beat in cilia of opalina. *Proc. Roy. Soc. Lond. B*, 175:219–233, 1970. doi: 10.1098/rspb.1970.0020.

[69] Sidney L. Tamm. Ciliary motion in *Paramecium*: a scanning electron microscope study. *J. Cell Biol.*, 55:250–255, 1972. doi: 10.1083/jcb.55.1.250.

[70] Sidney L. Tamm, T. M. Sonneborn, and R. V. Dippell. The role of cortical orientation in the control of the direction of ciliary beat in *Paramecium*. *J. Cell Biol.*, 64:98–112, 1975. doi: 10.1083/jcb.64.1.98.

[71] Douglas R. Brumley, Marco Polin, Timothy J. Pedley, and Raymond E. Goldstein. Metachronal waves in the flagellar beating of *Volvox* and their hydrodynamic origin. *J. R. Soc. Interface*, 12:20141358, 2015. doi: 10.1098/rsif.2014.1358.

[72] Shay Gueron and Konstantin Levit-Gurevich. Energetic considerations of ciliary beating and the advantage of metachronal coordination. *Proc. Natl. Acad. Sci. U.S.A.*, 96:12240–12245, 1999. doi: 10.1073/pnas.96.22.12240.

[73] Martin B. Short, Cristian A. Solari, Sujoy Ganguly, Thomas R. Powers, John O. Kessler, and Raymond E. Goldstein. Flows driven by flagella of multicellular organisms enhance long-range molecular transport. *Proc. Natl. Acad. Sci. U.S.A.*, 103:8315–8319, 2006. doi: 10.1073/pnas.0600566103.

[74] Sébastien Michelin and Eric Lauga. Efficiency optimization and symmetry-breaking in a model of ciliary locomotion. *Phys. Fluids*, 22:111901, 2010. doi: 10.1063/1.3507951.

[75] Henry Shum, Anurag Tripathi, Julia M. Yeomans, and Anna C. Balazs. Active ciliated surfaces expel model swimmers. *Langmuir*, 29:12770–12776, 2013. doi: 10.1021/la402783x.

[76] Jens Elgeti and Gerhard Gompper. Emergence of metachronal waves in cilia arrays. *Proc. Natl. Acad. Sci. U.S.A.*, 110:4470–4475, 2013. doi: 10.1073/pnas.1218869110.

[77] Yong Woon Kim and Roland R. Netz. Pumping fluids with periodically beating grafted elastic filaments. *Phys. Rev. Lett.*, 96:158101, 2006. doi: 10.1103/PhysRevLett.96.158101.

[78] Boris Guirao and Jean-François Joanny. Spontaneous creation of macroscopic flow and metachronal waves in an array of cilia. *Biophys. J.*, 92:1900–1917, 2007. doi: 10.1529/biophysj.106.084897.

[79] D.R. Brumley, M. Polin, T.J. Pedley, and R.E. Goldstein. Hydrodynamic synchronization and metachronal waves on the surface of the colonial alga *Volvox carteri*. *Phys. Rev. Lett.*, 109:268102, 2012. doi: 10.1103/PhysRevLett.109.268102.

[80] Bruce Alberts, Alexander Johnson, Julian Lewis, Martin Raff, Keith Roberts, and Peter Walter. *Molecular Biology of the Cell*. Garland Science, New York, 2008.

[81] John R. Blake and Michael A. Sleigh. Mechanics of ciliary locomotion. *Biol. Rev.*, 49:85–125, 1974. doi: 10.1111/j.1469-185X.1974.tb01299.x.

[82] I. R. Gibbons. The relationship between the fine structure and direction of beat in gill cilia of a lamellibranch mollusc. *J. Biophys. Biochem. Cytol.*, 11:179–205, 1961.

[83] S. P. Sorokin. Reconstructions of centriole formation and ciliogenesis in mammalian lungs. *J. Cell Sci.*, 3:207–234, 1968.

[84] Andrej Vilfan and Frank Jülicher. Hydrodynamic flow patterns and synchronization of beating cilia. *Phys. Rev. Lett.*, 96:058102, 2006. doi: 10.1103/PhysRevLett.96.058102.

[85] Nariya Uchida and Ramin Golestanian. Synchronization and collective dynamics in a carpet of microfluidic rotors. *Phys. Rev. Lett.*, 104:178103, 2010. doi: 10.1103/PhysRevLett.104.178103.

[86] Nariya Uchida and Ramin Golestanian. Synchronization in a carpet of hydrodynamically coupled rotors with random intrinsic frequency. *Europhys. Lett.*, 89:50011, 2010. doi: 10.1209/0295-5075/89/50011.

[87] Jurij Kotar, Marco Leoni, Bruno Bassetti, Marco Cosentino Lagomarsino, and Pietro Cicuta. Hydrodynamic synchronization of colloidal oscillators. *Proc. Natl. Acad. Sci. U.S.A.*, 107:7669–7673, 2010. doi: 10.1073/pnas.0912455107.

[88] Nariya Uchida and Ramin Golestanian. Generic conditions for hydrodynamic synchronization. *Phys. Rev. Lett.*, 106:058104, 2011.

[89] Nariya Uchida and Ramin Golestanian. Hydrodynamic synchronization between objects with cyclic rigid trajectories. *Eur. Phys. J. E*, 35:135, 2012.

[90] Benjamin M. Friedrich and Frank Jülicher. Flagellar synchronization independent of hydrodynamic interactions. *Phys. Rev. Lett.*, 109:138102, 2012. doi: 10.1103/PhysRevLett.109.138102.

[91] M Cosentino Lagomarsino, P. Jona, and B. Bassetti. Metachronal waves for deterministic switching two-state oscillators with hydrodynamic interaction. *Phys. Rev. E*, 68:021908, 2003. doi: 10.1103/PhysRevE.68.021908.

[92] Peter Lenz and Andrey Ryskin. Collective effects in ciliar arrays. *Phys. Biol.*, 3:285–294, 2006. doi: 10.1088/1478-3975/3/4/006.

[93] Thomas Niedermayer, Bruno Eckhardt, and Peter Lenz. Synchronization, phase locking, and metachronal wave formation in ciliary chains. *Chaos*, 18:037128, 2008. doi: 10.1063/1.2956984.

[94] C. Wollin and H. Stark. Metachronal waves in a chain of rowers with hydrodynamic interactions. *Eur. Phys. J. E*, 34:42, 2011. doi: 10.1140/epje/i2011-11042-7.

[95] C. W. Oseen. *Neuere Methoden und Ergebnisse in der Hydrodynamik*. Leipzig, 1927.

[96] J. R. Blake. A note on the image system for a stokeslet in a no-slip boundary. *Proc. Camb. Phil. Soc.*, 70:303–310, 1971. doi: 10.1017/S0305004100049902.

[97] J. R. Blake and A. T. Chwang. Fundamental singularities of viscous flow. Part I: The image systems in the vicinity of a stationary no-slip boundary. *J. Engrg. Math.*, 8:23–29, 1974. doi: 10.1007/BF02353701.

[98] Jurij Kotar, Luke Debono, Nicolas Bruot, Stuart Box, David Phillips, Stephen Simpson, Simon Hanna, and Pietro Cicuta. Optimal hydrodynamic synchronization of colloidal rotors. *Phys. Rev. Lett.*, 111:228103, 2013. doi: 10.1103/PhysRevLett.111.228103.

[99] Rachel R. Bennett and Ramin Golestanian. Emergent run-and-tumble behavior in a simple model of *Chlamydomonas*. *Phys. Rev. Lett.*, 110:148102, 2013.

[100] Rachel R. Bennett and Ramin Golestanian. Phase dependent forcing and synchronization in a three-sphere model of *Chlamydomonas*. *New J. Phys.*, 15: 075028, 2013.

[101] Rachel R. Bennett and Ramin Golestanian. A steering mechanism for phototaxis in *Chlamydomonas*. *J. R. Soc. Interface*, 12:20141164, 2015. doi: 10.1098/rsif.2014.1164.

[102] Katja Polotzek and Benjamin M. Friedrich. A three-sphere swimmer for flagellar synchronization. *New J. Phys.*, 15:045005, 2013.

[103] Douglas R. Brumley, Kirsty Y. Wan, Marco Polin, and Raymond E. Goldstein. Flagellar synchronization through direct hydrodynamic interactions. *eLife*, 3: e02750, 2014. doi: 10.7554/eLife.02750.

[104] Veikko F. Geyer, Frank Jülicher, Jonathon Howard, and Benjamin M. Friedrich. Cell-body rocking is a dominant mechanism for flagellar synchronization in a swimming alga. *Proc. Natl. Acad. Sci. U.S.A.*, 110:18058–18063, 2013. doi: 10.1073/pnas.1300895110.

[105] O. Bénichou, M. Coppey, M. Moreau, P-H Suet, and R. Voituriez. Optimal search strategies for hidden targets. *Phys. Rev. Lett.*, 94:198101, 2005. doi: 10.1103/PhysRevLett.94.198101.

[106] Frederic Bartumeus and Simon A. Levin. Fractal reorientation clocks: Linking animal behavior to statistical patterns of search. *Proc. Natl. Acad. Sci. U.S.A.*, 105:19072–19077, 2008. doi: 10.1073/pnas.0801926105.

[107] Dan V. Jr. Nicolau, Judith P. Armitage, and K. Maini, Philip. Directional persistence and the optimality of run-and-tumble chemotaxis. *Comput. Biol. Chem.*, 33:269–274, 2009. doi: 10.1016/j.compbiolchem.2009.06.003.

[108] Howard C. Berg. *E. coli in Motion*. Springer-Verlag, 2004.

[109] Martin Welch, Kenji Oosawa, Shin-Ichi Aizawa, and Michael Eisenbach. Phosphorylation-dependent binding of a signal molecule to the flagellar switch of bacteria. *Proc. Natl. Acad. Sci. U.S.A.*, 90:8787–8791, 1993.

[110] Howard C. Berg. *Random Walks in Biology*. Princeton University Press, West Sussex, 1993.

[111] Roman Stocker and William M. Durham. Tumbling for stealth? *Science*, 325: 400–402, 2009. doi: 10.1126/science.1177269.

[112] Howard C. Berg and Edward M. Purcell. Physics of chemoreception. *Biophys. J.*, 20:193–219, 1977. doi: 10.1016/S0006-3495(77)85544-6.

[113] Steven M. Block, Jeffrey E. Segall, and Howard C. Berg. Impulse responses in bacterial chemotaxis. *Cell*, 31:215–226, 1982. doi: 10.1016/0092-8674(82)90421-4.

[114] Jeffrey E. Segall, Steven M. Block, and Howard C. Berg. Temporal comparisons in bacterial chemotaxis. *Proc. Natl. Acad. Sci. U.S.A.*, 83:8987–8991, 1986.

[115] Antonio Celani and Massimo Vergassola. Bacterial strategies for chemotaxis response. *Proc. Natl. Acad. Sci. U.S.A.*, 107:1391–1396, 2010. doi: 10.1073/pnas.0909673107.

[116] H. Harz and P. Hegemann. Rhodopsin-regulated calcium currents in *Chlamydomonas*. *Nature*, 351:489–491, 1991. doi: 10.1038/351489a0.

[117] G. B. Witman. *Chlamydomonas* phototaxis. *Trends Cell Biol.*, 3:403–408, 1993. doi: 10.1016/0962-8924(93)90091- E.

[118] S. Tamm. Ca^{2+} channels and signalling in cilia and flagella. *Trends Cell Biol.*, 4:305–310, 1994. doi: 10.1016/0962-8924(94)90226-7.

[119] E.M. Holland, F. J. Braun, C. Nonnengässer, H. Harz, and P. Hegemann. The nature of rhodopsin-triggered photocurrents in *Chlamydomonas*. I. kinetics and influence of divalent ions. *Biophys*, 70:924–931, 1996. doi: 10.1016/S0006-3495(96)79635-2.

[120] P. Hegemann. Algal sensory photoreceptors. *Annu. Rev. Plant Biol.*, 59:167–189, 2008. doi: 10.1146/annurev.arplant.59.032607.092847.

[121] R. Kamiya and G.B. Witman. Submicromolar levels of calcium control the balance of beating between the two flagella in demembranated models of *Chlamydomonas*. *J. Cell Biol.*, 98:97–107, 1984. doi: 10.1083/jcb.98.1.97.

[122] U. Rüffer and W. Nultsch. Flagellar photoresponses of *Chlamydomonas* cells held on micropipettes: I. change in flagellar beat. *Cell Motil. Cytoskel.*, 15: 162–167, 1990. doi: 10.1002/cm.970150305.

[123] U. Rüffer and W. Nultsch. Flagellar photoresponses of chlamydomonas cells held on micropipettes: II. change in flagellar beat pattern. *Cell Motil. Cytoskel.*, 18:269–278, 1991. doi: 10.1002/cm.970180404.

[124] E. M. Holland, H. Harz, R. Uhl, and P. Hegemann. Control of phobic behavioral responses by rhodopsin-induced photocurrents in *Chlamydomonas*. *Biophys*, 73: 1395–1401, 1997. doi: 10.1016/S0006-3495(97)78171-2.

[125] Kenjiro Josef, J. Saranak, and K. W. Foster. An electro-optic monitor of the behavior of *Chlamydomonas reinhardtii* cilia. *Cell Motil. Cytoskel.*, 61:83–96, 2005. doi: 10.1002/cm.20064.

[126] K. Josef, J. Saranak, and K. W. Foster. Ciliary behavior of a negatively phototactic *Chlamydomonas reinhardtii*. *Cell Motil. Cytoskel.*, 61:97–111, 2005. doi: 10.1002/cm.20069.

[127] C.J. Horst and G. B. Witman. A nonphototactic mutant of *Chlamydomonas* lacks control of flagellar dominance. *J. Cell Biol.*, 120:733–741, 1993. doi: 10.1083/jcb.120.3.733.

[128] U. Rüffer and W. Nultsch. Flagellar photoresponses of *ptx1*, a nonphototactic mutant of *Chlamydomonas*. *Cell Motil. Cytoskel.*, 37:111–119, 1997. doi: 10.1002/(SICI)1097-0169(1997)37:2<111::AID-CM3>3.0.CO;2-B.

[129] K. Yoshimura and Ritsu Kamiya. The sensitivity of chlamydomonas photoreceptor is optimized for the frequency of cell body rotation. *Plant Cell Physiol.*, 42:665–672, 2001. doi: 10.1093/pcp/pce084.

[130] K. Schaller, R. David, and R. Uhl. How *chlamydomonas* keeps track of the light once it has reached the right phototactic orientation. *Biophys. J.*, 73:1562–1572, 1997. doi: 10.1016/S0006-3495(97)78188-8.

[131] N. Morel-Laurens. Calcium control of phototactic orientation in *Chlamydomonas reinhardtii*: Sign and strength of response. *Photochem. Photobiol.*, 45:119, 1987. doi: 10.1111/j.1751-1097.1987.tb08412.x.

[132] M. E. H. Feinlab and G. M. Curry. The relationship between stimulus intensity and oriented phototactic response (topotaxis) in *Chlamydomonas*. *Physiol. Plant.*, 25:346–352, 1971. doi: 10.1111/j.1399-3054.1971.tb01453.x.

[133] T. Takahashi and M. Watanabi. Photosynthesis modulates the sign of phototaxis of wild-type *Chlamydomonas reinhardtii*. effects of red background illumination and 3-(3',4'-dichlorophenyl)-1,1-dimethylurea. *FEBS Lett.*, 336:516–520, 1993. doi: 10.1016/0014-5793(93)80867-T.

[134] Klaus Schaller and Rainer Uhl. A microspectrophotometric study of the shielding properties of eyespot and cell body in *Chlamydomonas*. *Biophys. J.*, 73: 1573–1578, 1997. doi: 10.1016/S0006-3495(97)78189-X.

[135] Kai M. Thormann, Renée M. Saville, Soni Shukla, and Alfred M. Spormann. Induction of rapid detachment in *Shewanella oneidensis* MR-1 biofilms. *J. Bacteriol.*, 187:1014–1021, 2005. doi: 10.1128/JB.187.3.1014-1021.2005.

[136] Karin Sauer, M. C. Cullen, A. H. Rickard, L. A. H. Zeef, David G. Davies, and P. Gilbert. Characterization of nutrient-induced dispersion in *Pseudomonas aeruginosa* PAO1 biofilm. *J. Bacteriol.*, 186:7312–7326, 2004. doi: 10.1128/JB.186.21.7312-7326.2004.

[137] Kai M. Thormann, Stefanie Duttler, Renée M. Saville, Mamoru Hyodo, Soni Shukla, Yoshihiro Hayakawa, and Alfred M. Spormann. Control of formation and cellular detachment from *Shewanella oneidensis* MR-1 biofilms by cyclic di-GMP. *J. Bacteriol.*, 188:2681–2691, 2006. doi: 10.1128/JB.188.7.2681-2691.2006.

[138] L. D. Landau and E. M. Lifshitz. *Theory of Elasticity.* Elsevier, Oxford, 1986.

[139] Shoichi Wakiya. Application of bipolar coordinates to the two-dimensional creeping motion of a liquid. II. some problems for two circular cylinders in viscous fluid. *J. Phys. Soc. Japan*, 39:1603–1607, 1975. doi: 10.1143/JPSJ.39.1603.

[140] Raymond E. Goldstein, Marco Polin, and Idan Tuval. Noise and synchronization in pairs of beating eukaryotic flagella. *Phys. Rev. Lett.*, 103:168103, 2009. doi: 10.1103/PhysRevLett.103.168103.

[141] Knut Drescher, Raymond E. Goldstein, Nicolas Michel, Marco Polin, and Idan Tuval. Direct measurement of the flow field around swimming microorganisms. *Phys. Rev. Lett.*, 105:168101, 2010. doi: 10.1103/PhysRevLett.105.168101.

[142] Jeffrey S. Guasto, A. Johnson, Karl, and J. P. Gollub. Oscillatory flows induced by microorganisms swimming in two dimensions. *Phys. Rev. Lett.*, 105:168102, 2010. doi: 10.1103/PhysRevLett.105.168102.

[143] T. J. Racey, R Hallet, and B. Nickel. A quasi-elastic light scattering and cinematographic investigation of motile chlamydomonas reinhardtii. *Biophys. J.*, 35:557–571, 1981. doi: 10.1016/S0006-3495(81)84812-6.

[144] Kyriacos C. Leptos, Kirsty Y. Wan, Marco Polin, Idan Tuval, Adriana I. Pesci, and Raymond E. Goldstein. Antiphase synchronization in a flagellar-dominance mutant of *Chlamydomonas*. *Phys. Rev. Lett.*, 111:158101, 2013.

[145] G. Maruyama. Continuous markov processes and stochastic equations. *Rend. Circ. Math. Palermo*, 4:48–90, 1955. doi: 10.1007/BF02846028.

[146] Timothy Sauer. *Numerical Analysis*. Pearson, Essex, 2nd edition, 2012.

[147] E. G. Govorunova and O. A. Sineshchekov. Chemotaxis in the green flagellate alga *Chlamydomonas*. *Biochem. (Mosc.)*, 70:717–725, 2005.

[148] Mehdi Molaei, Michael Barry, Roman Stocker, and Jian Sheng. Failed escape: Solid surfaces prevent tumbling of *Escherichia coli*. *Phys. Rev. Lett.*, 113: 068103, 2014. doi: 10.1103/PhysRevLett.113.068103.

[149] Anna Bagorda and Carole A. Parent. Eukaryotic chemotaxis at a glance. *J. Cell Sci.*, 121:2621–2624, 2008. doi: 10.1242/jcs.018077.

[150] Kristen F. Swaney, Chuan-Hsiang Huang, and Peter N. Devreotes. Eukaryotic chemotaxis: A network of signaling pathways controls motility, directional sensing, and polarity. *Annu. Rev. Biophys.*, 39:265–289, 2010. doi: 10.1146/annurev.biophys.093008.131228.